OPTICAL MICROSPECTROMETERS USING IMAGING DIFFRACTION GRATINGS

S. GRABARNIK

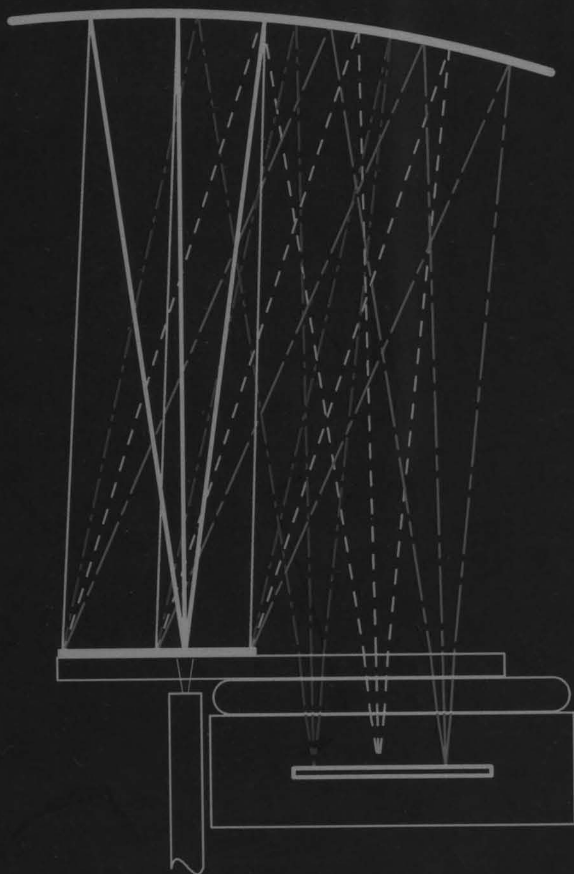

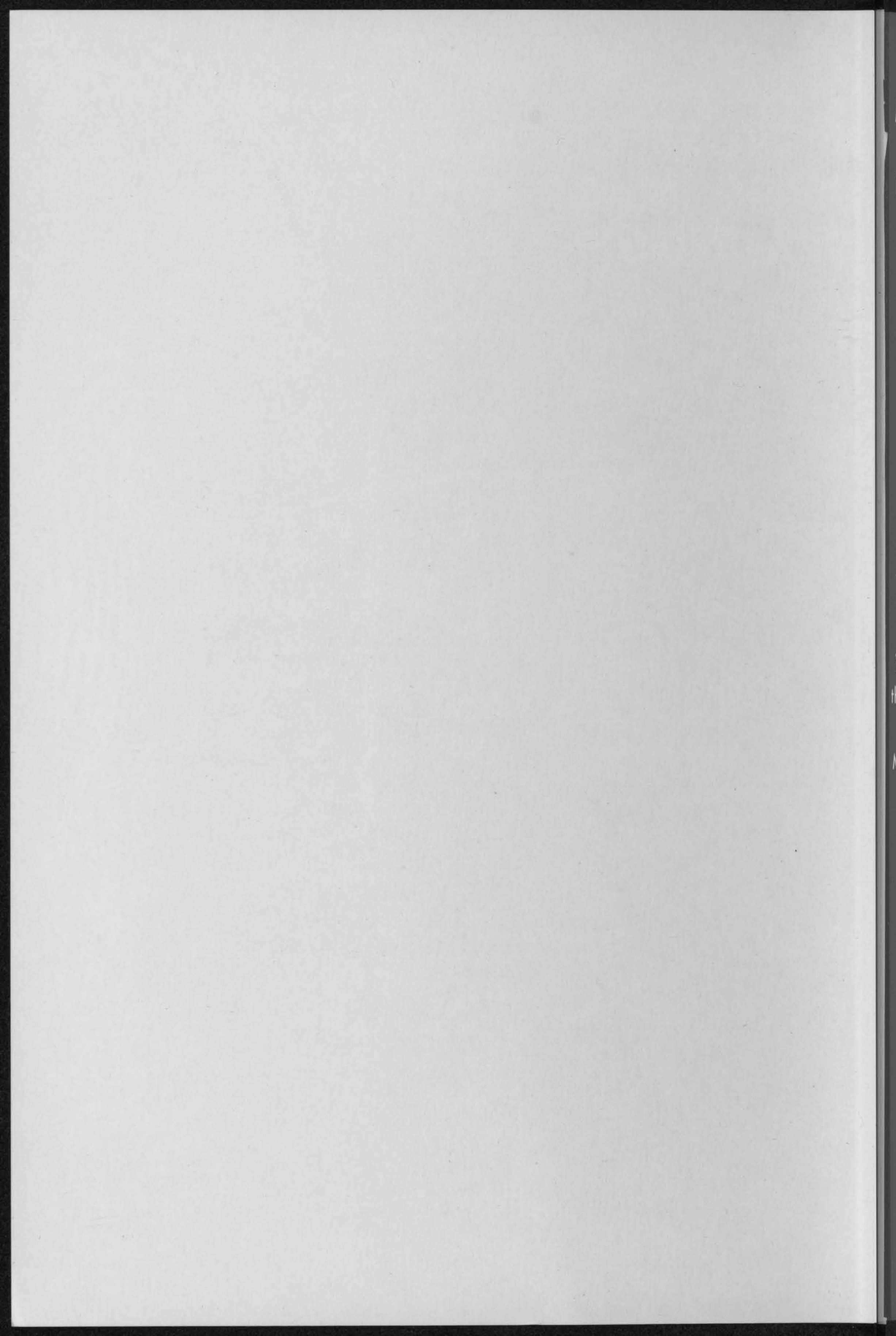

Optical Microspectrometers Using Imaging Diffraction Gratings

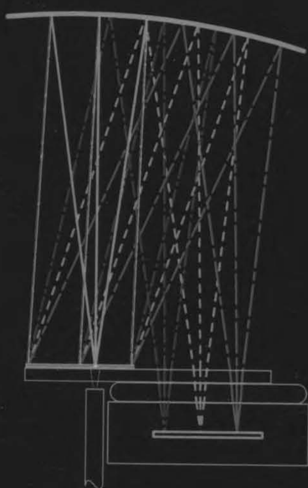

You are cordially invited for the open defence of my thesis that takes place on Monday, January 11th, 2010 at 10:00 in the Senaatzaal of the Aula of Delft University of Technology, Mekelweg 5, Delft

A short introductory presentation starts at 09:30

Semen Grabarnik
sgrabarnik@yahoo.com

Propositions accompanying the thesis

Optical microspectrometers using imaging diffraction gratings

Semen Grabarnik

Delft, January 11, 2010

1. The history of spectrometer design and fabrication dates back more than two centuries and the main principles of operation introduced at that early time are still the basis of modern devices (this thesis).

2. Compact (with dimensions comparable to that of an integrated circuit) and inexpensive spectrometers could bring about applications that would not be feasible with large conventional spectrometers.

3. Although high spectral resolving power can be achieved in a macroscopic optical system that includes aspherical elements, the planar surfaces that result from a MEMS-like process are to be preferred in a microsystem that should be fabricated at low unit costs (this thesis).

4. The limitations of MEMS technology in an optical microsystem can be circumvented by adding an additional postprocessing step in the fabrication process, or by introducing a single external non-MEMS optical component.

5. The principal design challenge in a microspectrometer is to find a compromise that settles the contradictory requirements of high optical throughput versus small size of the microdevice. High throughput requires a large entrance hole, but the resulting entrance hole largely determines the system dimensions.

6. Perhaps we don't pay attention to it, but the most frequently observed spectrum in daily life is a rainbow (this thesis).

7. To an engineer aiming for the best solution, designing is like an iterative process without end. The necessary number of iterations at any moment in time is always one more than the number you have already done.

8. Sometimes, the fastest way to get to the solution of a problem is to throw everything out and start over again.

9. There is never a single right solution. There are always multiple wrong ones, though.

10. Underestimating the requirements of an application sometimes results in products that are amazing from the technology point of view, but useless for the people these products are intended for.

11. All numerical models are limiting. The task of an engineer is to figure out what the limitations are of the model considered and to decide how it can nevertheless be used to solve a particular problem.

12. Nowadays virtual social networks are so popular that your friends may twitter you if you do not yet have a profile on Facebook.

These propositions are considered defendable and as such have been approved by the supervisor, Prof. dr. ir. G. C. M. Meijer.

Stellingen behorende bij het proefschrift

Optical microspectrometers using imaging diffraction gratings

Semen Grabarnik

Delft, 11 januari 2010

1. De geschiedenis van spectrometerontwerp en fabricage gaat meer dan twee eeuwen terug en de belangrijkste werkprincipes, zoals indertijd ingevoerd, vormen nog steeds de basis van moderne apparaten (dit proefschrift).

2. Compacte (met afmetingen vergelijkbaar met die van een geïntegreerd circuit) en goedkope spectrometers kunnen toepassingen mogelijk maken, welke niet haalbaar zouden zijn met grote conventionele spectrometers.

3. Hoewel een hoog spectraal oplossend vermogen kan worden gerealiseerd in een macroscopisch optisch systeem met a-sferische elementen, zijn in een microsysteem, welke gefabriceerd moet kunnen worden tegen lage stukskosten, de planaire structuren van een MEMS-achtig proces te prefereren (dit proefschrift).

4. De beperkingen van de MEMS-technologie in een optisch microsystem kunnen worden vermeden door toevoeging van een extra stap aan het einde van de procesgang, of door toevoeging van een externe, niet-MEMS optische component.

5. De belangrijkste uitdaging bij het ontwerpen van een microspectrometer is het vinden van een compromis tussen de tegengestelde eisen van hoge optische throughput versus de afmetingen van het apparaat met dimensies in de orde van micrometers. Voor een hoge throughput is een groot ingangsgat nodig, welke echter ook in hoge mate de totale systeemafmetingen bepaalt.

6. Misschien besteden we er geen aandacht aan, maar het spectrum dat we in het dagelijks leven het vaakst waarnemen is een regenboog (dit proefschrift).

7. Ontwerpen is voor een perfectionistisch ingestelde ingenieur als een iteratief proces zonder eind. Het noodzakelijke aantal iteraties is op elk willekeurig moment altijd één meer dan het aantal reeds uitgevoerd.

8. Soms is alles omgooien en opnieuw beginnen de snelste manier om tot de oplossing van een probleem te komen.

9. Er is nooit een enkele goede oplossing. Er zijn wel altijd meerdere verkeerden.

10. Onderschatting van de toepassingseisen resulteert soms in producten die verbazingwekkend zijn vanuit het oogpunt van de technologie, maar nutteloos voor de mensen voor wie deze producten zijn bedoeld.

11. Alle numerieke modellen zijn beperkend. De taak van een ingenieur is om er achter te komen wat de beperkingen zijn van het model dat wordt overwogen en om te beslissen hoe het desondanks gebruikt kan worden om een gegeven probleem op te lossen.

12. Virtuele sociale netwerken zijn tegenwoordig zodanig populair, dat je vrienden je waarschijnlijk zullen 'twitteren' indien je nog geen profiel hebt op 'Facebook'.

Deze stellingen worden verdedigbaar geacht en zijn als zodanig goedgekeurd door de promotor,
Prof. dr. ir. G. C. M. Meijer.

875598

Optical microspectrometers using imaging diffraction gratings

Proefschrift

ter verkrijging van de graad van doctor
aan de Technische Universiteit Delft,
op gezag van de Rector Magnificus prof. ir. K.C.A.M. Luyben,
voorzitter van het College voor Promoties,

in het openbaar te verdedigen

op maandag 11 januari 2010 om 10.00 uur

TU Delft Library
Prometheusplein 1
2628 ZC Delft

door

Semen GRABARNIK
M.Sc. of Moscow Institute of Physics and Technology
geboren te Penza, Rusland

Dit proefschrift is goedgekeurd door de promotor:

Prof. dr. ir. G.C.M. Meijer

Copromotor: Dr. ir. R.F. Wolffenbuttel

Samenstelling promotiecommissie:

Rector Magnificus,	voorzitter
Prof. dr. ir. G.C.M. Meijer,	Technische Universiteit Delft, promotor
Dr. ir. R.F. Wolffenbuttel	Technische Universiteit Delft, copromotor
Prof. dr. J.H.G. Correia,	University of Minho, Portugal
Prof. dr. W. Mokwa,	RWTH Aachen, Duitsland
Prof. dr. ir. A.J.P. Theuwissen	Technische Universiteit Delft
Prof. dr. ir. P.P.L. Regtien	Universiteit Twente
Dr. G.V. Vdovin	Technische Universiteit Delft
Prof. dr. P.J. French	Technische Universiteit Delft, reservelid

TU Delft Library
Prometheusplein 1
2628 ZC Delft

ISBN: 978-90-9025048-9

Copyright © 2009 by S. Grabarnik
All rights reserved. No part of this publication may be reproduced or distributed in any form or by any means, or stored in a database or retrieval system, without the prior written permission of the author.

Printed in The Netherlands

to Irina

Contents

1. Introduction

1.1 Optical spectrum and Optical Spectroscopy 1
1.2 Spectrometers: has everything been done? 3
1.3 Motivation and objectives 5
1.4 Organization of the thesis 6

2. Essential concepts in the design and analysis of a spectroscopic instrument

2.1 Light, what does a spectrometer measure.................9
2.1.1 Evolution of light theories 9
2.1.2 Classical light theory 11
2.2 Main spectrometer components 24
2.2.1 Imaging optics 24
2.2.2 Dispersive elements...36
2.2.3 Photodetector 48
2.3 General spectroscopic instrument............................50
2.3.1 General configuration of a spectrometer 50
2.3.2 Realization of the spectrometer in microtechnologies 52
2.3.3 Resolution and resolving power 53
2.3.4 Instrumental profile 54
2.3.5 Factors limiting spectrometer resolution 54
2.3.6 Etendue or throughput and etendue-resolving power product...56
2.3.7 Operating bandwidth 57

2.3.8 Stray light 57
2.4 Conclusions 58

3. Various approaches to spectral measurements

3.1 Prism spectrometers 61
3.2 Grating spectrometers 63
3.3 Waveguide spectrometers 67
3.4 Spectrometers using photonic crystal structures ... 70
3.5 Interference spectrometers 71
3.5.1 Fabry-Perot spectrometers. 71
3.5.2 Fourier Transform spectrometers. 75
3.6 Why using a diffraction grating? 79

4. Planar microspectrometers based on imaging gratings

4.1 Planar imaging grating 86
4.2 Single grating spectrometer design 88
4.2.1 Spectrometer model 88
4.2.2 Principal configuration of the spectrometer 95
4.2.3 Rigorous ray tracing model 96
4.2.4 Grating efficiency 102
4.3 Double grating spectrometer design 103
4.3.1 Double grating imaging system 103
4.3.2 Principal configuration of the spectrometer 105
4.3.3 Ray tracing model 106
4.3.4 Efficiency of the gratings 110
4.4 Fabrication of the spectrometers 110
4.5 Characterization of the fabricated devices 116
4.6 Conclusions 120

5. Lithographically fabricated concave diffraction gratings

5.1 Concave grating imaging. 124
5.2 Concave grating based spectrometer design 129
5.3 Lithographic technology for the fabrication of concave gratings 132
5.4 Results of the experiments 136
5.4.1 Fabrication of the gratings 136
5.4.2 Characterization of the produced gratings. 137
5.4.3 Roughness induced scattering 142
5.4.4 Imaging performance of the gratings 144
5.5 Conclusions 147

6. Spectrometer with an external spherical mirror

6.1 Concept of the microspectrometer with an external spherical mirror 152
6.2 Microspectrometer design 154
6.2.1 Principal configuration and selection of the design parameters 154
6.2.2 Ray tracing design and optimization 157
6.2.3 Estimation of spectral resolution 162
6.2.4 Tolerances 164
6.2.5 Stray light 164
6.2.6 Grating diffraction efficiency. 165
6.3 Fabrication and characterization of the microspectrometer 166
6.3.1 Fabrication of the glass chips 166
6.3.2 Assembling of the microspectrometer. 167
6.3.3 Experimental characterization of the microspectrometer 168
6.4 Modifications of the microspectrometer 171

6.4.1 Design for maximising etendue-resolving power product 172
6.4.2 Design of a miniaturized imaging spectrometer 176
6.5 Conclusions 181

7. **Conclusions**

7.1 Three approaches to make a microspectrometer . 185
7.2 Performance of the developed microspectrometers in comparison with the commercial devices 189
7.3 Suggestions for future work 190

Summary 193

Samenvatting 195

Acknowledgements 197

List of publications 199

About the author 203

1. Introduction

1.1 Optical spectrum and Optical Spectroscopy

We usually associate the word "spectrum" with the number of colours we can see with our eyes. Perhaps we don't pay attention to it, but the most frequently observed spectrum in daily life (and probably the first one observed by a human) is a rainbow - the spectrum of a sun light. Usually, the air is saturated with tiny water droplets after rain. Due to material dispersion and their spherical shape, such droplets reflect a portion of the sun light back at an angle which slightly differs depending on the color (or wavelength), and approximately equal to 42°. Another example of spectral observation is an oil film on the water which becomes colored when illuminated in front of a dark background. This effect is due do light interference and such an oil film is an example of a Fabry-Perot filter, a spectral filter employed in many types of optical devices.

Actually, a concept of spectrum is very broad and has its general definition is in the Fourier Transform theory [1.1], according to which the spectrum is a representation of a time function in the frequency domain. Applied to the wave theory of light, in which light is considered as a sum of electromagnetic waves characterized by the oscillating frequency and direction of propagation, this definition implies that spectrum is a representation of the intensity of waves

constituting light depending on their frequencies (or wavelengths). According to the quantum theory, light is a collection of photons, particles having certain energy. The energy of a photon is also associated with the frequency via Plank equation as $E = h\nu$. Thus the spectrum of light can also be interpreted as the energy distribution of the concentration of photons in the light beam.

It was Isaac Newton who first introduced the concept of spectrum, which is nowadays universally used in modern optical science, in his classic "Optiks" [1.2] published in 1704, where he described his experiments with the sunlight dispersed by prisms. He showed that white light could be decomposed into continuous series of colours which he called "spectrum". This word is of Latin origin and means literally "appearance".

More than two centuries of scientific research has discovered that light contains a wealth of information on the matter that emits or interacts with it, and this information is encoded in spectrum. Indeed, according to quantum theory, each atom is characterized by it's electron transitions, which are responsible for the absorption or emission of energy in form of photons. Thus, the spectrum of the emitted light, for example, contains information on the atoms of the emitting matter, such as the type and the concentration of the atoms. To decode the information one has to separate and measure intensities of different spectral components. That is the task of Optical Spectroscopy - a branch of science that extract the information about the matter analysing the spectrum of emitted or absorbed light.

Spectral analysis was critical in many advances in physics, both in theory and in experimental techniques. For example, Gustav Kirchhoff and Robert Bunsen obtained spectra of many elements and developed the first practical spectroscope in 1860 [1.3]. They were the first to apply spectral analysis for the identification of chemical substances and discovered two chemical elements cesium and rubidium. Since then spectroscopy helped to discover 18 previously unknown elements. The Bohr's model of the atom [1.4] was defined by relating measured spectrum of light emitted by hydrogen atoms to the motion of electrons. Niels Bohr explained the origin of atomic spectra in a way that each spectral line could be interpreted as a difference between energy levels of an electron in atom. This concept together with the developments in quantum mechanics by Erwin Schrodinger, Werner Heisenberg and others gave the impact to the investigation of more complicated atomic and molecular structures. Nowadays spectral analysis has a tremendous number of applications [1.5], [1.6] which is due to the

many advantages of the spectroscopy compared to other analytical methods:

- Analysis times of a few seconds.
- Simultaneous multicomponent analysis.
- No sample preparation is usually required for liquids, solids or gases.
- Non-invasive and nondestructive analysis is possible.
- Cost per analysis is very low and usually no reagents are used.
- Physical properties and biological effects can be calculated from the spectra of samples.
- Automated correction of background and interferences is performed in instruments by means of computer algorithms.
- Detection limits can be very low.
- Sample sizes ranges from picograms to the mass of complete planets.
- Molecular structural information can be derived from spectra.

Spectroscopy is a standard technique for the identification of different chemicals. Another example is the environmental monitoring which includes analysis of spectral lines of various gases to determine the composition of the atmosphere. Spectroscopy is also a necessary tool in biophysics and medicine allowing non intruding analysis of cells and tissues. A simple color analysis is widely used in cosmetic and paper industry. Each of the applications demands specially suited equipment for the spectral measurements and analysis. The important part of such an equipment is a spectrometer (or spectrograph) - the primary device that performs spectral decomposition of light and measures the intensity of its spectral components.

1.2 Spectrometers: has everything been done?

The history of spectrometer design and fabrication goes back more than two centuries and the main principles of operation introduced at that early time are still the basis of modern devices. The milestones in the history of the development are as follows. Isaac Newton used a pinhole in his experiments to form a bundle of rays passing through a prism. The first improvement is the introduction of slit by William Wollaston in 1802 and independently by Joseph Fraunhofer in 1814 [1.7]. The slit was much easier to work with and allowed

observation of finer details in a spectrum.

The diffraction grating, invented by David Rittenhouse in 1785, was used by Joseph Fraunhofer for his spectral measurements in 1820s [1.8]. A further improvement to the diffraction gratings was made by Henry Rowland, who also introduced spherical grating [1.9] combining both the dispersion and imaging functionality. Interferometers developed in 1892 by Albert Michelson [1.10] and in 1899 by Charles Fabry and Alfred Perot [1.11] are now bearing their names and are the basis for the Fourier - Transform and Fabry - Perot spectrometers.

The 20th century has brought further improvements to the design and fabrication technologies of the spectroscopic devices. With the invention of lasers and holography spectrometers received holographic gratings with better performance in terms of efficiency and imaging properties, as compared to ruled gratings known since Rowland experiments.

Advances in IC technology made very sensitive detectors like CCD or CMOS cameras available. Such detectors allow the recording of a spectrum produced by the spectrometer optics with much higher dynamic range and better signal sensitivity than photographic plates used before.

Very sensitive and high-resolution spectrometers are available on the market nowadays as a result of all mentioned achievements, and the performance of the spectrometers has almost reached the theoretical limits. However, the research and development activity in the field of spectrometer design doesn't stop. There are several reasons for that. First, each application requires a spectrometer with the specific characteristics (for example weight or dimensional constraints), and it is a challenge for a spectrometer designer to satisfy those requirements. There is a huge opportunity for research in inventing new spectrometer designs and implementing new technologies and materials for production. Second, in the last decades a great progress was achieved in optical waveguides and MEMS. These technologies, although not directly suited for the spectrometer fabrication, bring nevertheless new possibilities for designers [1.12]. MEMS technologies allow miniaturization of the design eliminating the complex alignment of different spectrometer parts during the fabrication and integration of optics with photosensors and electronics. Since MEMS are intended for mass production at low cost per unit, a spectrometer fabricated with MEMS compatible technologies would be rather cheap compared to conventional devices. Low-cost is likely to increase the number of applications that the device can have.

1.3 Motivation and objectives

One of the trends in modern industry is the integration and miniaturisation of components and devices. The interesting example is the sensors market, where sensors are integrated with the electronics using batch processing resulting both in smaller and cheaper systems at the same time. Such a progress was possible due to the availability of MEMS technologies. Although MEMS technologies are highly suitable for the fabrication of a compact low cost device, on the other hand, these technologies impose their own specific requirements and limitations on a spectrometer design. MEMS technologies include deposition of different materials on a silicon or glass wafer, litography and etching. Such a processing is best suited for the fabrication of planar devices and components. However, an optical system such as a spectrometer usually includes non-planar (spherical or aspherical) elements which are used for collimation and focusing of light. Taking these limitations into account, a designer of a miniature MEMS based spectrometer could face one or more of the following challenges:

- Design a spectrometer based on plane optical surfaces only.
- Adapt MEMS technologies for the fabrication of non-planar elements.
- Integrate non-planar external parts with MEMS parts.

The objective of the work presented in this thesis is the development of a compact and inexpensive spectrometer providing high (better than 1 nm) spectral resolution in a wide spectral bandwidth (about 300 nm) in the visible region. The fabrication technology of the spectrometer should allow its integration with the supporting electronic circuits. The size of the whole device must be comparable with that of an electronic component, so the spectrometer could be mounted directly on a printed circuit board.

The potential applications of such a spectrometer range from space and aviation to chemical analysis and medicine. Small size and weight would be extremely important in space systems, while low price is essential in portable medical devices. The choice of the MEMS technologies for the spectrometer fabrication was natural, because of the advantages mentioned above. Thus the spectrometer design should satisfy not only dimensional constraints and performance requirements, but also allow fabrication in a simple MEMS batch process. As a consequence, the work described in this thesis includes research in optical design and the adaptation of the available technological processes for the fabrication of the spectrometer in a MEMS foundry.

1.4 Organization of the thesis

This thesis presents research on the design and fabrication of an extremely compact, high performance and potentially low cost spectrometer conducted at the Delft University of Technology.

The thesis outline is as follows:

This introductory chapter, which explains motivation and objectives of the thesis and illustrates applications of the spectral measurements and spectrometers in science and industry.

Chapter 2 reviews the basics of light and spectrum theory and discusses general concepts in the design of a spectroscopic instrument. The specific spectrometer components including optical imaging system, dispersive elements (grating, FP etalons, etc.) and detectors, as well as theoretical concepts used in the optical design, are briefly described.

Chapter 3 reviews the previous work on spectrometers and discusses different approaches to build a spectral instrument, including Fabry-Perot, Fourier-Transform, grating and waveguide spectrometers. The choice of the grating as a basis for the development of the microspectrometer in this thesis is proved.

Chapter 4 describes spectrometers composed of planar elements only and an operation principle based on the use of planar imaging gratings. Due to a planar configuration, such spectrometers are fully MEMS compatible. The chapter starts with the theoretical basics of an imaging diffraction grating. Subsequently, the design, fabrication and results of experimental characterization of single- and double-grating planar spectrometers are described.

Chapter 5 demonstrates theoretically the advantages of the concave gratings as compared to planar imaging gratings. A simple MEMS-compatible technology for the fabrication of concave diffraction gratings is presented and the experimental results obtained with the fabrication of test gratings and their use in a miniature spectrometer are described.

Chapter 6 presents the design, fabrication and testing of a two-component spectrometer. Most of the essential spectrometer components, including the

entrance slit, aberration-correcting diffraction grating and image sensor, are integrated on a single planar chip (the first component), while a spherical mirror is a single external component. The adaptations of this design for applications requiring high sensitivity and for its use in an imaging spectroscopic system are also discussed.

The last chapter draws the conclusion to this research and discusses possible future work.

The original contributions of the work described in this thesis are mainly on the design and experimental validation of three microspectrometer concepts and the MEMS post-processes used for their fabrication. These are: two types of planar microspectrometers, a spectrometer with a concave grating fabricated in a MEMS-compatible process and a MEMS-integrated microspectrometer with an external mirror. These concepts are described in Chapter 4, Chapter 5 and Chapter 6 respectively.

References

[1.1] R. N. Bracewell, *The Fourier transform and its applications*, McGraw-Hill, Boston, 2000

[1.2] Sir Isaac Newton. *Opticks: Or, a Treatise of the Reflexions, Refractions, Infexions and Colours of Light*. Sam Smith and Benjamin Walford, London, 1704.

[1.3] M. E. Weeks, "The discovery of the elements: XIII. Some spectroscopic studies", *Journal of Chemical Education*, 9(8): 1413-1434, 1932.

[1.4] Niels Bohr. On the constitution of atoms and molecules. *Phil. Magazine*, 26(6): 1-25, 1913

[1.5] R. J. Dempsey, D. G. Davis, R. G. Buice, Jr., and R. A. Lodder, "Biological and medical applications of near-infrared spectroscopy," *Appl. Spectrosc.* 50: 18A–34A (1996).

[1.6] C. P. Bacon, Y. Mattley, and R. DeFrece, "Miniature spectroscopic instrumentation: application to biology and chemistry," *Rev. Sci. Instrum.* 75: 1-16 (2004).

[1.7] J. A. Rust, J. A. Nóbrega, C. P. Calloway Jr. and B. T. Jones, " Fraunhofer Effect Atomic Absorption Spectrometry", *Analytical Chemistry*, 77(4): 1060-1067, 2005

[1.8] J. Fraunhofer. Kurzer bericht von den resultaten neuerer versuch ber die gesetze des lichtes, und die theorie derselben. *Gilbert's Annalen der Physik*, 74: 337-378, 1823.

[1.9] H. A. Rowland. On concave gratings for optical purposes. *Phil. Magazine*, 16(99): 197-210, 1883.

[1.10] P. Giacomo, "The Michelson interferometer", *Microchimica Acta*, 93(1): 19-31, 1987

[1.11] J. M. Vaughan, *The Fabry-Perot Interferometer; history, theory, practice and applications*, Taylor & Francis, 1989

[1.12] R. F. Wolffenbuttel. MEMS-based optical mini- and microspectrometers for the visible and infrared spectral range. *J. Micromech. Microeng.*, 15: S145 - S152, 2005

2. Essential concepts in the design and analysis of a spectroscopic instrument

This chapter starts with a short review of theories of light and light propagation. Subsequently, the main attention is devoted to wave theory, since this is the basis for a modern optical design. The concept of spectrum, geometrical optics and diffraction are reviewed. This is followed by the discussion of the main components which can be used to build a spectrometer. Finally, the general configuration of a spectroscopic instrument is presented and important concepts applicable to a spectrometer design are discussed.

2.1 Light, what does a spectrometer measure

2.1.1 Evolution of light theories

The nature of light has been a topic of scientific discussions since ancient times. Pythagoras [2.1] (580 - 500 BC) believed that the material objects become visible due to tiny particles which are emitted by these objects and strike a human eye. Starting from the 17th century there were two main concepts of light in science: corpuscular (assuming that light is a flux of particles) and wave

(considering light as a wave) theories. In 19th century the wave theory, supported by many experiments including diffraction and interference, became dominating. However it remained unclear what is the nature of the light waves. The most popular hypotheses assumed that the space is filled with a special substance, "aether", and light is actually a wave which can be excited and propagate in this medium. This idea had not been confirmed experimentally, and, moreover, the results of some experiments contradicted this hypotheses (Michelson–Morley experiment). Finally, the theory of relativity formulated by Einstein in 1905 resulted in the final rejection of the aether concept [2.1].

James Maxwell proposed his theory of an electromagnetic field in 1860's. He concluded that light is actually an electromagnetic wave. This conclusion was confirmed by experimental results available at that time. For example, the velocity of an electromagnetic wave in vacuum which followed from his equations was equal to experimentally measured speed of light. Nevertheless, the wave theory was not able to explain such phenomena as black body radiation or photoelectric effect. This problem was resolved with the development of quantum theory in the beginning of 20th century. The idea had been proposed by Plank in 1900 [2.1]. This theory has something common with a corpuscular concept since it considers light as a flux of particles called photons. Photons move with a speed of light and can be characterized by a certain energy. The quantum approach also explains phenomena on a level of molecules and atoms. For example, the nature of a photoelectric effect becomes clear when considering interaction of a photon and an electron.

The wave electromagnetic theory of light is not rejected by a quantum approach. These two concepts are used in modern science forming a so-called corpuscular-wave dualism. Indeed, the task of any theory is to explain physical phenomena and provide a basis for theoretical calculations which would be in agreement with the experimental results. In this sense the wave and quantum theories can work together to explain the same phenomena from the different point of views and to contribute to a complete picture. For example, a light beam can be considered as an electromagnetic wave with frequency ν and velocity c or as a flux of photons with energy defined by Plank equation $E = h\nu$ moving with speed c. In practice, either wave or quantum theory can be more efficient for solving a particular problem.

Wave theory and geometrical optics (which is actually a simplification of the wave theory in the case when the diffraction and interference effects are

negligible) are used in the design of optical systems. While quantum concept is applied in problems related to light - matter interaction. For example, the optical spectral measurements performed with a spectrometer which was designed using the laws of wave and geometrical optics, can be analysed scientifically on the basis of quantum concept.

2.1.2 Classical light theory

Maxwell Equations

The state of electro-magnetic excitation in space induced by moving electric charges can be described by a set of two vectors, $\boldsymbol{E}$ (electric field) and $\boldsymbol{B}$ (magnetic induction). In presence of material objects a scalar ρ representing the electrical charge density and additional vectors are required: $\boldsymbol{H}$ (magnetic vector), $\boldsymbol{D}$ (electric displacement) and $\boldsymbol{j}$ (electric current density). The fundamental relationships between these quantities was established by James Clerk Maxwell and are known as Maxwell equations [2.2], [2.3]. Maxwell equations are not unchanged in different systems of units. Although the fundamental dependencies remain the same, the equations can differ by constant coefficients. In a Gaussian system of units (which main difference from the SI system is the definition of the unit of charge) these equations are as follows:

$$\mathrm{curl}\boldsymbol{H} = \frac{1}{c}\frac{\partial \boldsymbol{D}}{\partial t} + \frac{4\pi}{c}\boldsymbol{j} \tag{2.1}$$

$$\mathrm{curl}\boldsymbol{E} = -\frac{1}{c}\frac{\partial \boldsymbol{B}}{\partial t} \tag{2.2}$$

$$\mathrm{div}\boldsymbol{D} = 4\pi\rho \tag{2.3}$$

$$\mathrm{div}\boldsymbol{B} = 0 \tag{2.4}$$

The coefficient of proportionality c in Eq. (2.1) and Eq. (2.2) is the speed of electromagnetic waves in vacuum, as it is shown below. The system of four equations (2.1) - (2.4) is not complete since it involves 16 independent variables (components of vectors $\boldsymbol{E}$, $\boldsymbol{B}$, $\boldsymbol{D}$, $\boldsymbol{H}$, $\boldsymbol{j}$ and a scalar ρ). Thus the system must be supplied with additional equations. These are equations which describe the properties of the medium. In principle, these equations can be obtained on the basis of a molecular theory of polarization, magnetic and electrical conductivity

of the medium. Using equations of classical or quantum mechanics and statistical physics the relations between the vectors ***E***, ***B*** and ***D***, ***H***, ***j*** can be established. However, in the case of a relatively weak field the material equations take the form of a simple proportionality:

$$\boldsymbol{D} = \varepsilon \boldsymbol{E} \quad \textbf{(2.5)}$$

$$\boldsymbol{B} = \mu \boldsymbol{H} \quad \textbf{(2.6)}$$

$$\boldsymbol{j} = \sigma \boldsymbol{E} \quad \textbf{(2.7)}$$

The coefficients ε, μ and σ are called electrical and magnetic permittivity and conductivity of the medium respectively. In practice these coefficients are measured experimentally for a given material and for the most of the materials the required values can be found in a reference book (see for example [2.4]).

Electromagnetic waves

It follows from the Maxwell equations that the electromagnetic field can exist in form of a wave. Indeed, according to Eq. (2.1), the time-varying electric field can generate a magnetic field. In turn, a non-constant in time magnetic field produces electric field as it follows from Eq. (2.2). One can obtain from the equations (2.1)- (2.7), assuming a homogeneous medium without electrical charges and currents, the following equations:

$$\nabla^2 \boldsymbol{E} - \frac{\varepsilon\mu}{c^2}\frac{\partial^2 \boldsymbol{E}}{\partial t^2} = 0$$

$$\nabla^2 \boldsymbol{H} - \frac{\varepsilon\mu}{c^2}\frac{\partial^2 \boldsymbol{H}}{\partial t^2} = 0 \quad \textbf{(2.8)}$$

These are wave equations which suggests the existence a wave moving with a velocity $v = c/(\sqrt{\varepsilon\mu})$. In vacuum $\varepsilon = 1$ and $\mu = 1$, thus $v = c$. The vector ***E*** in a wave is directed normally to the vector ***H***, and the direction of the wave propagation is perpendicular to both of vectors. The direction of vector ***S*** called "Poynting vector" coincides with the direction of wave and the vector magnitude equals to the energy flux. The vector is defined via electric and magnetic vectors as follows:

$$S = \frac{c}{4\pi} E \times H \tag{2.9}$$

A solution of wave equations (2.8) in a homogeneous medium is a function which is periodic in time and space and can be described as:

$$\begin{aligned} E &= E_0(r)\exp(-i\omega t + ikr) \\ H &= H_0(r)\exp(-i\omega t + ikr) \end{aligned} \tag{2.10}$$

The field amplitudes E_0 and H_0 are functions slowly varying in space and depending on the space vector r. The vector k in equations (2.10) is a wave vector, which defines a period of space oscillations of a wave, or wavelength $k = \frac{2\pi}{\lambda}$. The scalar ω defines the reciprocal of the wave oscillation period in time and is called the wave frequency. From this definition the relationship for a wave in a vacuum follows: $c = \omega / k$. The direction of amplitude vector E_0 defines the polarization of an electromagnetic wave.

In the presence of material objects the solution of the wave equations conserves its time-periodic exponential form. However, field amplitude and wave vector can vary in a complex manner. In a homogeneous medium speed of an electromagnetic wave and its wavelength are reduced proportionally to a quantity called refractive index n:

$$\begin{aligned} v_{medium} &= \frac{c}{n} \\ \lambda_{medium} &= \frac{\lambda_{vacuum}}{n} \\ n &= \sqrt{\varepsilon\mu} \end{aligned} \tag{2.11}$$

In an electromagnetic wave, the amplitudes of electric and magnetic fields are not independent. As already mentioned, a time-variable electric (magnetic) field is a source for a magnetic (electric) field. The amplitudes of these fields are connected as follows:

$$E = \sqrt{\frac{\mu}{\varepsilon}} H \tag{2.12}$$

Thus, an electromagnetic wave propagating in a free space or in a homogeneous medium can be characterized by the tree quantities: electric field magnitude and polarization defined by $\boldsymbol{E_0}$ and wave frequency ω. A wave with a constant direction of $\boldsymbol{E_0}$ is called a polarized wave.

Light in a classical theory

Light, according to classical theory, is an electromagnetic wave with a wave frequency in the range of about 10^{12} - 10^{15} Hz, and with a wavelength in vacuum in the bandwidth from 10 nm to 1 mm. The wavelength of visible light which can be registered by a human eye ranges approximately from 390 nm to 760 nm. Different colours of visible objects are due to different wavelengths of the reflected or emitted light. For example, a light with the 560 nm wavelength is sensed by a human eye as green, while the wavelength of 700 nm is recognized as red.

Spectrum

Light that can be described by a wave with a single frequency ω and wavelength λ is called "monochromatic" which means literally "single colour". However, in reality, light rarely can be described by a single monochromatic wave. More adequate description is a sum of waves:

$$\boldsymbol{E}(\boldsymbol{r}, t) = \sum_j \boldsymbol{E}_j(\boldsymbol{r}) \exp(-i\omega_j t + i\boldsymbol{k}_j \boldsymbol{r}) \tag{2.13}$$

Thus, electromagnetic field of a light wave is not characterized by a single oscillating frequency. The values of $\boldsymbol{E_j}$ in Eq. (2.13) describe contributions from waves at different frequencies to the resulting wave. Equation (2.13) can be transformed introducing a new unit vector $\boldsymbol{n}$ which is collinear to $\boldsymbol{k}$: $\boldsymbol{k} = k\boldsymbol{n}$.

$$\boldsymbol{E}(\boldsymbol{r}, t) = \sum_j \boldsymbol{E}_j(\boldsymbol{r}) \exp\left(-i\omega_j\left(t - \frac{\boldsymbol{nr}}{c}\right)\right) \tag{2.14}$$

In the limit, the frequencies of different waves contributing to the sum in Eq. (2.14) become close to each other and the sum can be substituted by an integral:

$$E(r, t) = \int E(\omega, r) \exp\left(-i\omega\left(t - \frac{nr}{c}\right)\right) d\omega \qquad \textbf{(2.15)}$$

Consider a fixed point A in space. The field of a light wave in point A is given by Eq. (2.15) in the form:

$$E_A(t) = \varphi \int E_A(\omega) \exp(-i\omega t) d\omega \ , \qquad \textbf{(2.16)}$$

In Eq. (2.16) $\varphi = \exp\left(i\frac{r_A}{c}\right)$ is a constant phase. According to the definition of Fourier Transform, the function $E_A(\omega)$ in equation (2.16) is the spectrum of $E_A(t)$.

The field in equations (2.10) - (2.16) is a complex valued vector. In practice, the intensity of light is the physical quantity which is measured because it is hardly possible to measure an electric field oscillating with such a high frequency (10^{12} - 10^{15} Hz). From equations (2.9) and (2.12) it follows that light intensity is proportional to the square of the electric field amplitude:

$$I \sim |E|^2 = E \times E^* \qquad \textbf{(2.17)}$$

where E^* is a complex conjugate of E. Taking into account Eq. (2.17) one can rewrite equations (2.13) - (2.16) for intensity:

$$I = \sum_j I_j(\omega_j) \qquad \textbf{(2.18)}$$

$$I = \int S(\omega) \exp(-i\omega) d\omega \qquad \textbf{(2.19)}$$

$$S(\omega) \sim \int E(\nu) E^*(\omega - \nu) d\nu \qquad \textbf{(2.20)}$$

The function $S(\omega)$ in equations (2.19) and (2.20) is the intensity spectrum of the electromagnetic field described by the Eq. (2.16).

To conclude, a practical representation of light is a collection of monochromatic waves. Moreover, the spectrum describes the distribution of light energy over frequencies of the contributing waves.

Light propagation - Geometrical optics

Although solution of Maxwell equations with boundary conditions can provide a precise description of the electromagnetic field, it is often very difficult to find this solution. That is why there are approaches which are valid under certain assumptions and lead to essentially the same results as a solution of Maxwell equations, while allowing for much easier calculations. One of the such approaches is geometrical optics.

The equations (2.10) can be rewritten in a different form:

$$\begin{aligned} \boldsymbol{E}(\boldsymbol{r}, t) &= \boldsymbol{e}(\boldsymbol{r})\exp(i\omega t)\exp(ik_0 S(\boldsymbol{r})) \\ \boldsymbol{H}(\boldsymbol{r}, t) &= \boldsymbol{h}(\boldsymbol{r})\exp(i\omega t)\exp(ik_0 S(\boldsymbol{r})) \end{aligned} \quad \textbf{(2.21)}$$

In Eq. (2.21) k_0 is a wave vector in vacuum and function $S(\boldsymbol{r})$ is called eikonal. Substituting Eq. (2.21) into equations (2.1) - (2.4) one can obtain in the limit of a small wavelength (when members with k_0^{-1} are neglected) that eikonal obeys the following equation [2.3]:

$$(\nabla S)^2 = n^2 \quad \textbf{(2.22)}$$

Equation (2.22) is called eikonal equation and it is a basis for geometrical optics. The limits of validity of Eq. (2.22) (small wavelength limit) require that the fields magnitudes $\boldsymbol{e}$ and $\boldsymbol{h}$ vary slow over the dimensions comparable to wavelength.

The surfaces defined by $S(\boldsymbol{r}) = const$ are referred to as geometrical wave surfaces or geometrical wavefronts. It can be demonstrated [2.3] that the time-average of the Poynting vector is in the direction normal to the geometrical wavefront. This suggests to define the geometrical light rays as orthogonal trajectories to the geometrical wavefronts. The ray's direction coincide with the direction of Poynting vector (although, this is valid for an isotropic medium and not always true for an anisotropic one). If $\boldsymbol{r}(s)$ is the position vector of a ray point and s is the length of arc of the ray, the equation of the ray follows as:

$$n\frac{\mathrm{d}\boldsymbol{r}}{\mathrm{d}s} = \nabla S \quad \textbf{(2.23)}$$

From Eq. (2.22) and Eq. (2.23) the ray equation which does not include eikonal can also be derived:

$$\frac{\mathrm{d}}{\mathrm{d}s}\left(n\frac{\mathrm{d}\boldsymbol{r}}{\mathrm{d}s}\right) = \nabla n \qquad \textbf{(2.24)}$$

The direction of the ray can be described by a unit vector $\boldsymbol{s} = \frac{\nabla S}{n}$.

The laws of geometrical optics follow from Eq. (2.22) - Eq. (2.24). Indeed, if $n = const$, according to Eq. (2.24) $\frac{\mathrm{d}^2\boldsymbol{r}}{\mathrm{d}s^2} = 0$, which implies that in a homogeneous medium rays are straight lines. When light crosses a surface separating two homogeneous media of different refractive indices (see Eq. (2-1)), the rays change the direction according to the following equation which can be derived using Eq. (2.23) combined with Stokes' theorem (relating the integrals over the area and over its boundary) :

$$\boldsymbol{n}_{12} \times (n_1\boldsymbol{s}_1 - n_2\boldsymbol{s}_2) = 0 \qquad \textbf{(2.25)}$$

In Eq. (2.25) $\boldsymbol{n}_{12}$ is a normal to the interface at a point where a ray crosses the boundary. Equation (2.25) implies that the tangential component of the ray vector $\boldsymbol{s}$ is continuous across the interface. Mathematically, this is formulated as:

$$n_1 \sin(\theta_1) = n_2 \sin(\theta_2) \qquad \textbf{(2.26)}$$

Equation (2.26) is a formulation of Snell's law of refraction.

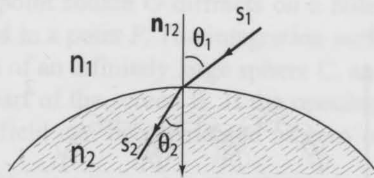

***Fig. 2-1.** Illustration of Snell's law of refraction.*

The law of reflection follows from Eq. (2.25) if one assumes $n_1 = n_2$. The reflected wave propagates back into the first medium at an angle $\theta_2 = \pi - \theta_1$.

One of the useful concepts in geometrical optics is optical path. The optical path between two points P_1 and P_2, a ray goes through, is defined by the integral along the ray trajectory:

$$L = \int_{P_2}^{P_1} n ds \qquad \textbf{(2.27)}$$

Since the phase increment of a light wave equals to $\frac{2\pi L}{\lambda}$, the optical path can be used to account for the effects caused by the wave nature of light (such as interference and diffraction) in calculations based on geometrical optics.

Diffraction

Geometrical optics can not provide an adequate description of an electromagnetic field if the assumption of a slowly varying field amplitude is not valid. This condition is violated, for example, at boundaries of shadows or at points where intensity has a sharp maximum. The behaviour of the optical field in these regions can be described by the diffraction theory based on the Huygens-Fresnel principle [2.3].

The Huygens-Fresnel principle assumes that every point on a wavefront is a source of the secondary spherical waves which mutually interfere. The results of the secondary waves interference is a new wavefront. This is illustrated in Fig. 2-2, where the plane wavefront 2 is a result of the interference of spherical waves generated at points of the plane wavefront 1.

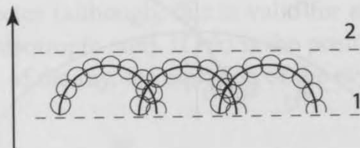

Fig. 2-2. Illustration of the Huygens-Fresnel principle.

The mathematical formulation of the Huygens-Fresnel principle had been proposed by Kirchhoff. The field at a point P can be described by an integral over a surface S surrounding P. If $\boldsymbol{n}$ is the normal to S and s is the distance from the point P to the point (x,y,z) on S, then the field amplitude $U(P)$ is:

$$U(P) = \frac{1}{4\pi}\iint\limits_S \left[U\frac{\partial}{\partial n}\left(\frac{\exp(iks)}{s}\right) - \frac{\exp(iks)}{s}\frac{\partial U}{\partial n}\right] dS \qquad \textbf{(2.28)}$$

In Eq. (2.28) $k = \frac{2\pi}{\lambda}$ is the wave vector. The integral Eq. (2.28) can be applied for various diffraction problems (by an appropriate selection of the surface for integration). For example, the problem of a wave propagating through a hole in an opaque screen is illustrated in Fig. 2-3.

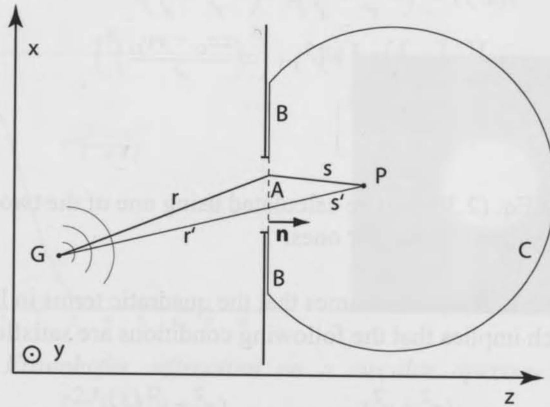

Fig. 2-3. *Diffraction of a wave on a hole in an opaque screen.*

A wave from a point source G diffracts on a hole and the intensity of the field is to be calculated in a point P. The integration surface can be selected to be consisting of a portion of an infinitely large sphere C, an opening A and a portion of a non-transparent part of the screen B. If the opening A much larger than the wavelength, then the field can be considered as zero on C and B and equal to $\frac{U_0 \exp(ikr)}{r}$ on A. In this case integral in Eq. (2.28) should be taken only over the opening A which results in:

$$U(P) = -\frac{iU_0}{2\lambda}\iint_S \frac{\exp(ik(r+s))}{rs}(\cos(n,r)-\cos(n,s))dS \quad \textbf{(2.29)}$$

If the distances from the points P and G to the screen are large compared to the size of the hole and δ is the angle between line GP and screen normal $\boldsymbol{n}$, Eq. (2.29) can be simplified to:

$$U(P) = -\frac{i\cos(\delta)}{\lambda}\frac{U_0\exp(ik(r'+s'))}{r's'}\iint_A \exp(ikf(x,y))dS \quad \textbf{(2.30)}$$

In Eq. (2.30) f(x,y) is a power series expansion of $(r+s)$ in x/r', x/s', y/r' and y/s':

$$\begin{aligned} f(x,y) = {} & \left(-\frac{x_G}{r'}-\frac{x_P}{s'}\right)x + \left(-\frac{y_G}{r'}-\frac{y_P}{s'}\right)y \\ & +\frac{1}{2}\left[\left(\frac{1}{r'}+\frac{1}{s'}\right)(x^2+y^2) + \left(-\left(\frac{xx_G+yy_G}{r'}\right)^2\right)\right. \\ & \left. -\left(\frac{xx_P+yy_P}{s'}\right)^2\right]\ldots \end{aligned} \quad \textbf{(2.31)}$$

Integral in Eq. (2.30) can be calculated using one of the two approximations known as Fresnel and Fraunhofer ones.

Fraunhofer diffraction assumes that the quadratic terms in Eq. (2.31) can be neglected, which implies that the following conditions are satisfied:

$$r' \gg \frac{(x^2+y^2)_{max}}{\lambda} \qquad s' \gg \frac{(x^2+y^2)_{max}}{\lambda}$$

$$or \quad \textbf{(2.32)}$$

$$\frac{1}{r'}+\frac{1}{s'} = 0 \qquad \left(\frac{x_G}{r'}\right)^2, \left(\frac{y_G}{r'}\right)^2, \left(\frac{x_P}{s'}\right)^2, \left(\frac{x_P}{s'}\right)^2 \ll \frac{r'\lambda}{(x^2+y^2)_{max}}$$

If Fresnel diffraction takes place, the linear as well as quadratic terms have to be taken into account in the integral of Eq. (2.30).

Calculation of the diffracted field in the case of a Fraunhofer diffraction is much simpler than in the case of a Fresnel one. As an example, a diffraction on a

circular transparent aperture in an opaque screen can be considered. This case is important in optics, since diffraction occurs at all circular-aperture optical elements such as lenses or mirrors. Introducing polar coordinates, it can be demonstrated by the direct integration of Eq. (2.30) in the Fraunhofer approximation (Eq. (2.32)), that the intensity of the diffracted light is described by Bessel function $J_1(x)$ [2.3], [2.5]:

$$I(r) = I_0\left(\frac{2J_1(kar/z)}{kar/z}\right)^2 \tag{2.33}$$

In Eq. (2.33) a is the aperture radius, z is the distance from the screen to the plane of observation, r is the radial coordinate in the observation plane and I_0 is the intensity in the center of the diffraction pattern. The Fraunhofer diffraction on a circular aperture is illustrated in Fig. 2-4.

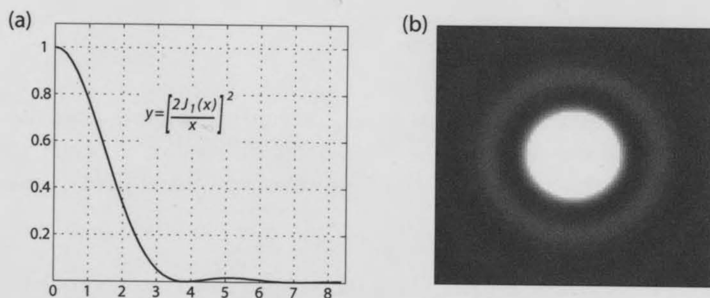

Fig. 2-4. *Fraunhofer diffraction on a circular aperture. The function* $y = \left[\frac{2J_1(x)}{x}\right]^2$ *(a) and intensity distribution (b).*

The central diffraction maximum is called the Airy disk and the radius r_A of the Airy disk is defined by the first zero of the Bessel function $J_1(x = 3.8) = 0$. From Eq. (2.33):

$$r_A = 1.22\frac{\lambda z}{2a} \tag{2.34}$$

Fraunhofer diffraction can be observed at a very large distance from the aperture as follows from the Eq. (2.32). For example, at a 600 nm wavelength, the

observation distance should be larger than 166 m for a 1 cm diameter aperture. However, Fraunhofer diffraction is also observed in the focal plane of a lens and optical imaging devices work in the Fraunhofer regime. Indeed, since the optical paths of the rays coming to a point in the image plane is the same for all rays, the interference effects will be essentially the same as if the diffracted pattern is observed in a distant plane.

It follows from the Eq. (2.34) that there is a minimum size of the image of a point source that can produced by an ideal lens, and the radius of this image is defined by the diffraction broadening induced by the finite lens aperture: $r_{im} = 1.22\frac{\lambda f}{D}$, where f is the focal length and D is the diameter of the lens. It can be also shown that the diffraction pattern of the light transmitted through a long slit of width D is described by the function $\mathrm{sinc}(x)^2$ and the angular diffraction broadening (angular semi-width of the first minimum) is defined as

$$\Delta\alpha = \frac{\lambda}{D}, \tag{2.35}$$

Another interesting conclusion which can be derived from Eq. (2.29) - Eq. (2.31) is that the result of the Fraunhofer diffraction is actually a Fourier Transform of the function describing the diffracting optical field over the spatial frequencies $\sigma_x = k\frac{x}{s'}$ and $\sigma_y = k\frac{y}{s'}$. This also implies that the intensity distribution observed in a focal plane of the lens is a Fourier Transform of the intensity in the object plane [2.5].

Finally, consider the Fresnel approximation of Eq. (2.29). Integral in Eq. (2.29) can be calculated analytically only for the point P lying on the axis which is normal to the aperture and crosses the aperture in its center. The intensity distribution in the off-axis points can be calculated numerically. The evolution of the intensity of the diffracted field for different values of the parameter $\frac{ka^2}{z}$ is shown in Fig. 2-5 (from [2.5]). As the observation plane becomes more distant from the aperture (increasing z) or the size of the aperture becomes smaller (decreasing a) or the wavelength becomes larger (decreasing k), the intensity distribution approaches the case of a Fraunhofer diffraction.

The constraints imposed by lens aperture are particularly relevant in micro-optical devices, where the aperture can be as small as 0.1 mm - 1 mm. Nevertheless, the corresponding distance necessary to obtain Fraunhofer diffraction pattern is still large: from ~1 cm to ~1 m. That is why such microdevices have to include imaging elements, such as micro-lenses or imaging Diffraction Optical Elements (DOE) or, in application to spectrometers, imaging diffraction gratings.

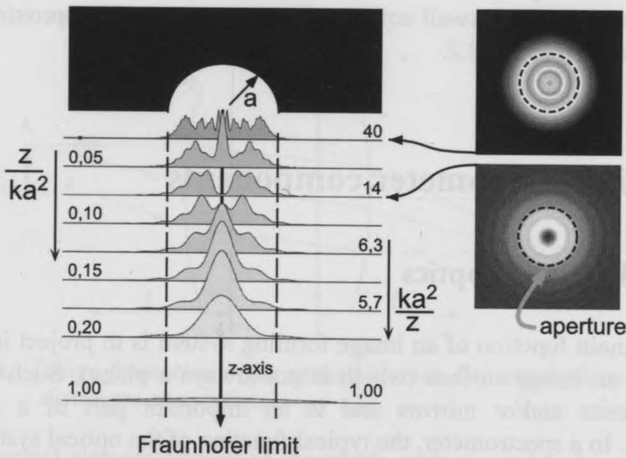

Fig. 2-5. Diffraction on a circular aperture from the Fresnel up to the Fraunhofer limit case (from [2.5]). Figures on the right show the light intensity distribution.

Implications of the theory on optical system design

The next chapters will discuss spectrometers, the instruments combining various optical elements. Normally, the design and analysis of an instrument (before it has been fabricated) is performed numerically using a special computer software. Such computer programs implement numerical algorithms to calculate the behaviour of light in an optical system. These algorithms are based on certain approximation of optical theory (for example, geometrical optics) or provide a precise numerical solution of Maxwell equations for specified boundary conditions. The theoretical aspects of light theory discussed in the preceding sections allows to define the applicability of different optical software for a given problem.

The optical design can be done using geometrical optics only, while the analysis of the designed optical system requires taking diffraction effects into account. The Kirchhoff's diffraction theory is often sufficient for this application.

However, the Kirchhoff's theory is not able to describe behaviour of the optical field correctly if the size of an aperture (for example, opening A in Fig. 2-3) becomes smaller and approaches the dimensions of a wavelength. This is the case, for example, when the efficiency of a diffraction grating has to be computed. Such a problem can be addressed using algorithms which provide an accurate solution of Maxwell equations without additional approximations, as is discussed in section 2.2.2.2.

2.2 Main spectrometer components

2.2.1 Imaging optics

The main function of an image forming system is to project images of real objects on an image surface (which is not always a plane). Such a system can include lenses and/or mirrors and is an important part of a spectroscopic instrument. In a spectrometer, the typical function of the optical system is to form a collimated light beam before the dispersive element and to focus the dispersed light onto the photodetector. In other words, the spectrometer optics builds a dispersed image of the entrance aperture. As it is discussed in section 2.3.5, the performance of the spectrometer optics is critical in achieving high spectral resolution and throughput. While this section reviews only main concepts necessary to describe the design of spectrometers, the detailed discussion of the optical system design can be found in literature (see for example [2.6] or [2.7]).

2.2.1.1 Gaussian optical system

The elementary theory of imaging developed by Carl Friedrich Gauss (1777-1855) is based on geometrical optics and assumes that the angles between the optical axis and the rays are small. This assumption is also known as the paraxial approximation.

An image-forming system operation is illustrated in Fig. 2-6. The system is

rotationally symmetric and includes optical elements between the surfaces S_1 and S_2. The axis of symmetry O_2O_1 is called the optical axis. An imaginary plane which includes an object point A and optical axis is called tangential plane, while the plane including optical axis and perpendicular to the tangential one is called the saggital plane. The optical axis is not always a straight line because it can change its direction, for example if there is a mirror in the system which reflects light at a certain angle.

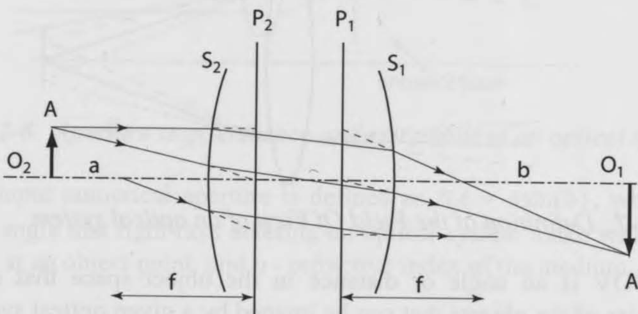

Fig. 2-6. *Image formation in an optical system. Principal planes and focal distances are shown.*

Each optical element as well as the whole system can be characterized by its focal distance. In Fig. 2-6 *f* is the focal distance of the system which can be defined using principal planes (P_1 and P_2). The principal planes are imaginary planes which allow to consider the complete system as a single element, which is illustrated by the trajectories of real rays designated by the solid lines in Fig. 2-6 and dashed lines representing imaginary trajectories. All rays emitted from a point located on an optical axis at a focal distance from the principal plane of the system are made parallel (collimated) by the optical system.

The system in Fig. 2-6 images point A into an image point A'. This implies that all the rays emitted from the point A at an angle with the optical axis not larger than a certain value (this angle defines the aperture of the system, see also section 2.3.6 and Fig. 2-28) come to the point A'. The relation between the distances from the object and image to the principal planes is expressed by the well-known lens equation:

$$\frac{1}{a} + \frac{1}{b} = \frac{1}{f} \tag{2.36}$$

The concept of the Field Of View (FOV) of an optical system is illustrated in Fig. 2-7.

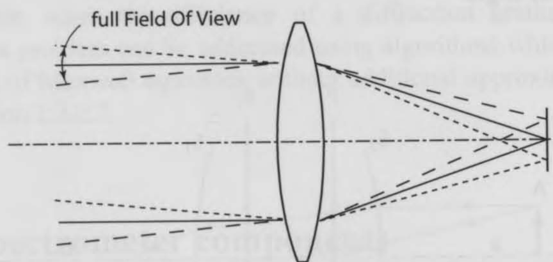

Fig. 2-7. *Definition of the Field Of View of an optical system.*

The FOV is an angle or distance in the object space that defines the maximum size of the objects that can be imaged by a given optical system. If the optical system is designed to be used with an image sensor, the maximum FOV is defined by the size of the sensor (see Fig. 2-7).

There is always an element in an optical system that limits the diameter of the bundle of rays that pass through the system. This element is called iris or aperture stop. The ray that goes through the center of an iris is called a chief ray. Aperture stop also defines the pupils of the system. The entrance pupil is an image of the stop observed in front of the system and the exit pupil is a stop image observed from the back. Figure 2-8 shows a telecentric system consisting of a positive and a negative lens with the aperture stop between the lenses.

If a chief ray can propagate along a straight line, it would cross a pupil in its center as illustrated in Fig. 2-8. The images of the aperture stop can be either virtual (as in Fig. 2-8) or real. The trajectory of a ray emitted from the object point is completely defined by the coordinates of the object point and the coordinates of ray intersection with one of the pupils.

The important characteristic of an imaging system is the F-number which is defined as a ratio of the focal distance to the entrance pupil diameter.

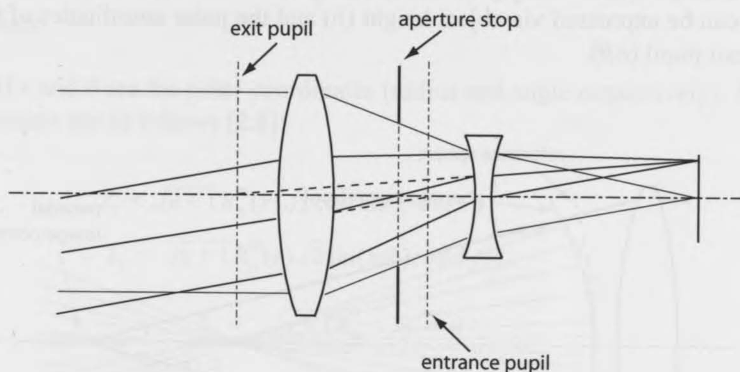

Fig. 2-8. *Aperture stop, entrance and exit pupils of an optical system.*

The input numerical aperture is defined as $NA = n\sin(\theta)$, where θ is the maximum angle that light rays entering an optical system make with the axis of the system at an object point, and n - refractive index of the medium.

2.2.1.2 Optical aberrations

When the paraxial approximation is not valid, the rays from an image point that enter an optical system do not come to the gaussian image point, but arrive in the vicinity of this point. This fact is due to imperfection of optics. For example, widely used due to its simplicity in fabrication, spherical lens in principle is not able to produce a perfect image. The deviations of the rays from the gaussian image point are the ray aberrations of the system. The larger the angle that make rays with the optical axis, the larger the aberrations. The result of aberrations is a blurring of a point image which implies the degradation of the performance of an imaging system. That is why the important problem in optical design is how to reduce aberrations of an optical system by an appropriate design of system elements.

Figure 2-9 shows ray trajectories in an aberrated system. The ideal (gaussian) image point is formed by the rays originated on a spherical converging wavefront (reference sphere). The aberrated wavefront does not coincide with the reference sphere because the optical path is not constant for all the rays due to imperfections of the optical system the rays come through. The deviation of the wavefront from the reference sphere is called the wavefront aberration.

The function describing the wavefront deviation or optical path difference (OPD) can be expressed via object height (h) and the polar coordinates of the ray in the exit pupil (r, θ).

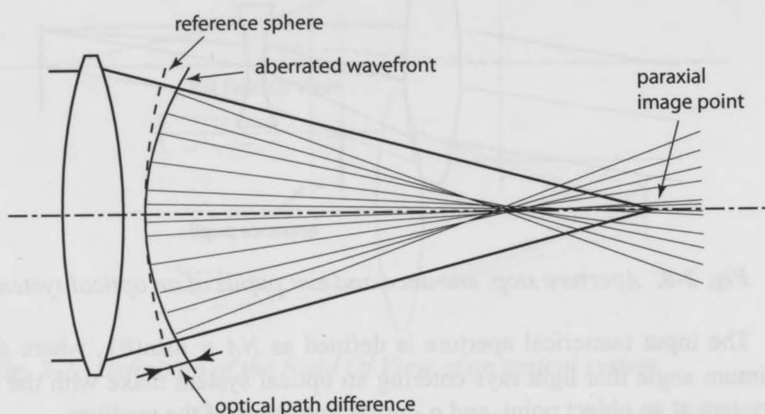

Fig. 2-9. *Illustration of the aberrations resulted from the optical path difference.*

In the case of a rotationally symmetrical system, the OPD function takes the form [2.6], [2.7]:

$$W = W_{020}r^2 + W_{111}hr\cos(\theta) + W_{040}r^4 + W_{131}hr^3\cos(\theta) \quad \textbf{(2.37)}$$

$$+W_{222}h^2r^2\cos(\theta)^2 + W_{220}h^2r^2 + W_{311}h^3r\cos(\theta) + \ldots$$

$$= \sum W_{ijk}h^i r^j \cos(\theta)^k$$

A different approach to describe the aberrated wavefront is to use Zernike polynomials. This is a complete set of polynomials defined on a circular aperture of a unit radius. The wavefront OPD function for an arbitrary optical system is expressed via Zernike polynomials Z_j and corresponding weight coefficients A_j as:

$$W = \sum_j A_j Z_j \quad \textbf{(2.38)}$$

The aberration coefficients A_{ij} in Eq. (2.38) in general depend on the field coordinate.

If r and θ are the polar coordinates (radius and angle respectively), Zernike polynomials are as follows [2.8]:

$$\left.\begin{array}{l} Z_j = \sqrt{n+1}R_n^m(r)\sqrt{2}\cos(m\theta),\ even\ j \\ Z_j = \sqrt{n+1}R_n^m(r)\sqrt{2}\sin(m\theta),\ odd\ j \end{array}\right\},\ m \neq 0$$

$$Z_j = \sqrt{n+1}R_n^0 \quad ,m = 0 \tag{2.39}$$

$$R_n^m(r) = \sum_{s=0}^{(n-m)/2} \frac{(-1)^s(n-s)!}{s![(n+m)/2-s]![(n-m)/2-s]!}r^{n-2s}$$

The values of m and n are integral and satisfy $m \le n$ and $n-|m| = even$.

The angular deviation of the rays equals to the partial derivative of the wave aberration polynomial:

$$\partial\alpha_x = \frac{\partial W}{\partial x} \qquad \partial\alpha_y = \frac{\partial W}{\partial y} \tag{2.40}$$

In order to characterize the degree of the wavefront aberration by a single number an RMS wavefront aberration can be used which is defined as follows:

$$W_{RMS} = \sqrt{\langle W^2\rangle - \langle W\rangle^2}$$

$$\langle W^n\rangle = \frac{\int (W(x,y))^n dxdy}{\int dxdy} \tag{2.41}$$

In the aberration analysis it is common to consider members of the sum in Eq. (2.37) which have the same order defined as $n = i+j$. Due to the rotational symmetry the order n can be only an even number (0, 2, 4, 6, ...). The zero-order aberration is simply a constant added to the wavefront. Aberrations of the second order are defocus and wavefront tilt. The first one can be compensated by an adjustment of the image plane while the second one implies an error in magnification. Fourth-order wave or third-order ray (see Eq. (2.40)) aberrations

have special names: spherical aberration, coma, astigmatism, field curvature and distortion.

Third-order spherical aberration is rotationally symmetric and its amplitude is defined by the coefficient W_{040}. This aberration corresponds to the Zernike polynomial Z_{11}. The ray trajectories in a system with a large spherical aberration are shown in Fig. 2-10(a).

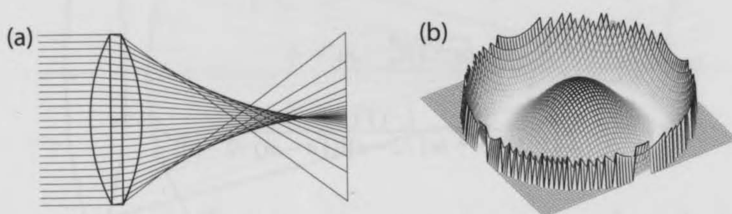

Fig. 2-10. *Spherical aberration: ray diagram (a) and optical path difference (b).*

Unlike a gaussian system which has a single focal point, the rays cross the optical axis at different points. The system in Fig. 2-10(a) does not have a single focus and an image of an axial point source is blurred for every position of an image plane. However, it is possible to find an image plane position in which spherical aberration is partly compensated by defocus resulting in a minimal possible image blurring. Such a position is called an optimal focus. Figure 2-10(b) shows a wavefront aberration (or optical path difference) over the exit pupil for an optimal focus position. Spherical aberration is an intrinsic property of optical elements with spherical surfaces (such as spherical lenses or mirrors), and aspherical components should be used (for example, paraboloidal mirrors) to reduce this aberration significantly.

Third-order aberration defined by the coefficient W_{131} is called coma due to characteristic pattern formed by the ray intersections with an image plane. Coma can be also expressed as a combination of Zernike polynomials Z_7 and Z_8. This aberration is proportional to the field angle and is zero for rays parallel to the optical axis. Figure 2-11(a) illustrates ray trajectories in the presence of coma. The rays going through a circular zone of the exit pupil generate a circular region in the image plane. The larger radius of the circular zone in the exit pupil, the larger corresponding circle is formed in the image plane and the larger distance

from the center of this circle to the paraxial image point. The presence of coma in an optical system can be recognized by a characteristic pattern of ray intersections with an image plane shown in Fig. 2-11(b). The optical path difference in the presence of coma is shown in Fig. 2-11(c).

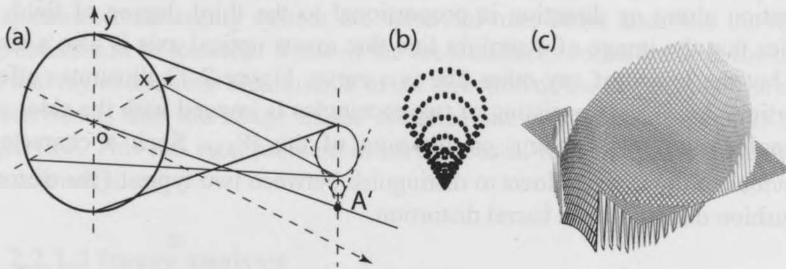

Fig. 2-11. Coma aberration: circular parts of the pupil produce circles in the image plane (a) resulting in a characteristic coma pattern (b). Optical path difference in the presence of coma (c).

Astigmatism and field curvature are usually considered together since these deal with quadratic dependence of a focal position on the field angle. These aberrations are defined by the coefficients W_{220} and W_{222} (Zernike polynomials Z_5 and Z_6). The result of astigmatism and field curvature is that the tangential and saggital focal points are located on two different surfaces, as shown in Fig. 2-12(a).

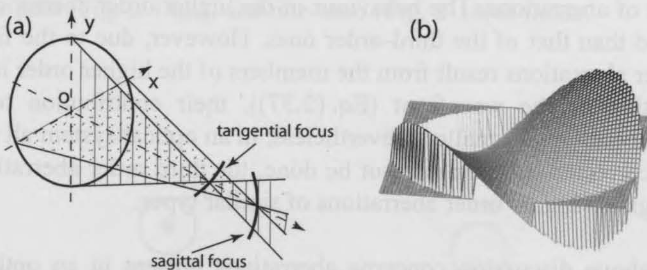

Fig. 2-12. Astigmatism and field curvature: ray diagram (a) and optical path difference (b).

If ε_x and ε_y are the ray aberrations in the ox and *oy* direction respectively,

then $\varepsilon_y = 0$ at the tangential focal surface and $\varepsilon_x = 0$ at the saggital focal surface. In the absence of astigmatism these two surfaces coincide.

The aberration called distortion is due to the coefficient W_{311}. The result of the distortion is that the ray aberration along ox direction $\varepsilon_x = 0$ and the ray aberration along *oy* direction is proportional to the third degree of field. This implies that the image of a straight line that meets optical axis is also a straight line, but the image of any other line is a curve. Figure 2-13 illustrates effect of distortion. An object consisting of two rectangles is imaged with the sides of the rectangles curved depending on the sign of the W_{311}. Such a characteristic behaviour of the image allows to distinguish between two types of the distortion: pincushion distortion and barrel distortion.

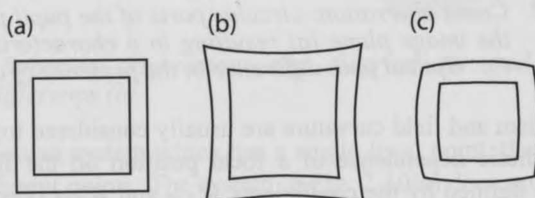

Fig. 2-13. *Distortion: Object (a), pincushion distortion (b) and barrel distortion (c).*

There are also aberrations of higher orders. These include higher order spherical aberration, coma, field curvature, astigmatism and distortion and also other types of aberrations. The behaviour of the higher order aberrations is more complicated than that of the third-order ones. However, due to the fact that the higher order aberrations result from the members of the higher order in the series decomposition of the wavefront (Eq. (2.37)), their contribution to the total wavefront aberration is smaller. Nevertheless, in an optical system all aberrations should be corrected. If these can not be done, the third order aberrations can be balanced against higher order aberrations of similar types.

The above discussion concerns aberrations present in an optical system working with a monochromatic light. For non-monochromatic light one has to deal with additional aberration called the chromatic one. This is due to the dependency of the refractive index of a lens (and consequently, refraction angle) on a wavelength. It is obvious, that an optical system using only reflective

components (mirrors) is free from chromatic aberrations.

In general, it is important for an optical system of a spectrometer to produce an image which is free from ray aberrations in a single direction - in the direction of the dispersion (see section 2.3.5). The exception is an imaging spectrometer discussed in chapter 6. That is why the most important aberrations to compensate in a spectrometer imaging system are spherical one, coma and field curvature. Astigmatism can be tolerated if one of the focal surfaces coincides with the image plane and ray aberrations are minimal in the direction of the dispersion. The result of distortion is that the image of the entrance slit in the spectrometer is not a straight line. This can be a problem in certain cases, for example if the entrance slit is relatively long.

2.2.1.3 Image analysis

The common way to estimate the performance of a designed imaging system for a given field and focal positions is to calculate the trajectories of rays emitted from a point source and forming a uniform grid at the entrance pupil. This method is called the ray tracing and the points of intersections of these rays with image plane form a pattern called the spot diagram. In an optical system with the perfectly corrected aberrations the spot diagram will be a point.

However, a point image is impossible in reality. The image size of a point source can not be smaller than a certain value defined by the diffraction on the exit pupil. That is why the image size can not be smaller than the diameter of the Airy disk (see pages 18 - 23). Figure 2-14 shows an example of a lens spot diagram for zero (Fig. 2-14(a)) and non-zero (Fig. 2-14(b) fields.

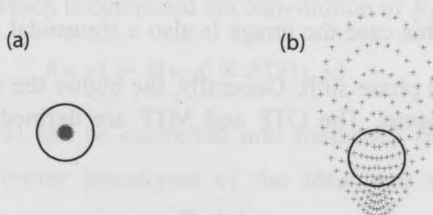

Fig. 2-14. *Spot diagram of a spherical lens for zero (a) and non-zero (b) fields in comparison with the Airy disk.*

It is visible on the Fig. 2-14 that for a zero field position aberrations are small and the image size is completely defined by the Airy disk. However, for the non-zero field aberrations make substantial contribution to the broadening of the image.

The imaging systems in which the effect of aberrations on the image quality is small as compared to the contribution of the diffraction on the exit pupil (for a specified range of fields and focal positions) are called diffraction-limited.

A more adequate characterisation of a point source image can be obtained by calculating a Point Spread Function (PSF). The PSF is the intensity distribution in the image plane resulted from a point source object. It can be computed as a square of the diffraction integral (Eq. (2.29)) over the exit pupil of the optical system. As it was mentioned before, the calculation of the diffraction integral for the points in the image plane of an optical system is equivalent to the Fourier Transform of the optical field at the exit pupil. The Fourier Transform method of the PSF calculation is widely used in optical design software (for example, ZEMAX [2.9]). First, the rays are traced from the point source to the exit pupil. For each of the rays the amplitude and phase are used to compute the complex wavefront amplitude on a grid at the exit pupil. Finally, the squared Fourier Transform of the obtained grid function completes the task. Figure 2-15 shows surface and gray-scale representations of PSF computed using ZEMAX for the same spherical lens which plot diagrams are demonstrated in Fig. 2-14 and for the same field angles.

Another commonly used measure of the performance of an optical system is Optical Transfer Function (OTF) and Modulation Transfer Function (MTF). Suppose that the object is a sinusoidal intensity distribution $I(x) = 1 + m\cos(2\pi\nu x + \phi(\nu))$. The contrast of this function is defined as follows: $m = \frac{I_{max} - I_{min}}{I_{max} + I_{min}}$. In this case the image is also a sinusoidal distribution but with different contrast and phase shift. Generally, the higher the object frequency, the lower the image contrast. The OTF and MTF are defined as functions of the object frequencies:

$$MTF(\nu_x, \nu_y) = \frac{m_{\text{image}}}{m_{object}}$$
$$OTF(\nu_x, \nu_y) = MTF \times \exp(iPTF) \quad \textbf{(2.42)}$$

In Eq. (2.42) *PTF* is a Phase Transfer Function which represents a phase shift. The OTF can be computed as a Fourier Transform of the PSF and the MTF is an absolute value of the OTF: $MTF = |OTF|$.

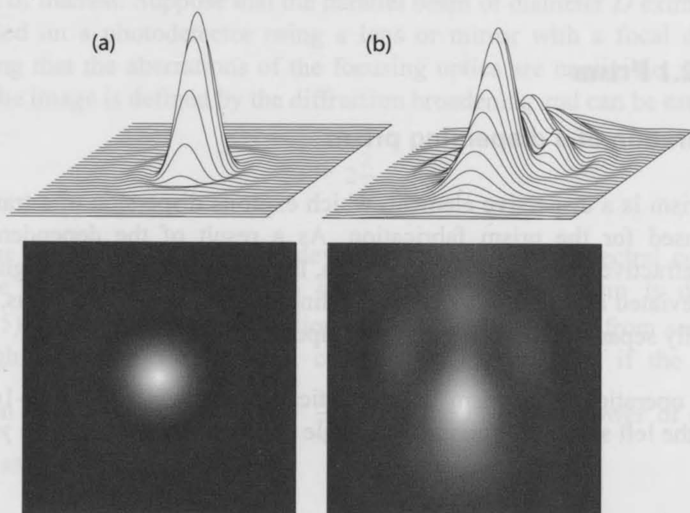

Fig. 2-15. *Surface and gray-scale representations of PSF for zero (a) and non-zero (b) fields of a spherical lens (ZEMAX).*

The PSF and OTF can be used to compute the image of an extended object. If the function *S(x,y)* describes the ideal (without influence of aberrations and diffraction) image obtained by ray tracing, the real image can be computed as a convolution of *S(x,y)* with the PSF. Since the PSF depends on the field position, it also depends on the coordinates *x* and *y* in the image plane. The real image is described by *I(x,y)* which is computed via convolution of *S* and *PSF*:

$$I(x, y) = S(x, y) \otimes PSF(x, y) \tag{2.43}$$

Equation (2.43) can be converted into frequency space. If $s(\nu_x, \nu_y)$ and $i(\nu_x, \nu_y)$ are the Fourier transforms of the ideal and real image functions respectively, the following relation is valid:

$$i(\nu_x, \nu_y) = s(\nu_x, \nu_y) \times OTF(\nu_x, \nu_y) \tag{2.44}$$

2.2.2 Dispersive elements

A dispersive element is a device that alters the intensity of light passing through the system or direction of light propagation depending on the light wavelength.

2.2.2.1 Prism

Operation of a dispersing prism

A prism is a dispersive element, which exploits dispersion of a transparent material used for the prism fabrication. As a result of the dependency of a material refractive index on the wavelength, light beams passing through a prism become deviated at different angles depending on the wavelength. Thus, a prism can spatially separate different spectral components of light.

The operation of a prism is schematically illustrated in Fig. 2-16. Light falling at the left side of the prism at an angle φ_1 is deviated at an angle γ.

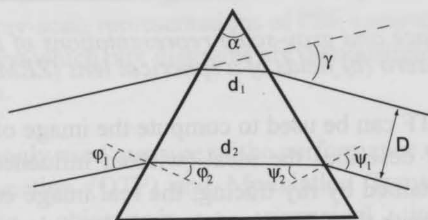

Fig. 2-16. Prism dispersing a collimated light beam.

Resolving power of a prism

From geometrical considerations using Snell's law one can obtain (assuming that the prism material refractive index is *n*, and the refractive index of the medium is 1):

$$\frac{\partial\gamma}{\partial\lambda} = \frac{\sin(\alpha)}{\cos(\psi_1)\times\cos(\varphi_2)}\frac{dn}{d\lambda} \tag{2.45}$$

Equation (2.45) connects the angular dispersion of a prism $\frac{\partial\gamma}{\partial\lambda}$ with the material dispersion $\frac{dn}{d\lambda}$. For spectroscopy applications the resolving power of a prism is of interest. Suppose that the parallel beam of diameter D exiting a prism is focused on a photodetector using a lens or mirror with a focal distance F. Assuming that the aberrations of the focusing optics are negligible, the angular size of the image is defined by the diffraction broadening and can be estimated as:

$$\delta\theta = 2\frac{\lambda}{D} \quad \textbf{(2.46)}$$

The difference between the deviation angles of two spectral components with the wavelengths λ_1 and λ_2 passing through the prism is defined by Eq. (2.45). According to the definition of the resolving power from section 2.3.3 (Rayleigh criterion), two spectral components are resolved if the following condition is satisfied: $\frac{\partial\gamma}{\partial\lambda}(\lambda_1 - \lambda_2) = \frac{\lambda}{D}$. Thus the resolving power of a prism is defined as:

$$R = \frac{\lambda}{\Delta\lambda} = D \times \frac{\partial\gamma}{\partial\lambda} = \frac{D \times \sin(\alpha)}{\cos(\psi_1) \times \cos(\varphi_2)}\frac{dn}{d\lambda} \quad \textbf{(2.47)}$$

Resolving power depends both on the prism material (via $\frac{dn}{d\lambda}$) and on the geometrical configuration of the system (prism vertex angle α and the angle at which light falls on the prism).

At a certain incident angle the refraction angles φ_2 and ψ_2 are equal. It can be demonstrated that the deviation angle γ takes the smallest possible value at this incident angle which is called the angle of minimum deviation [2.3]. The angle of minimum deviation depends on the prism material and apex angle:

$$\varphi_{mindev} = arc\sin\left(n \times \sin\left(\frac{\alpha}{2}\right)\right) \quad \textbf{(2.48)}$$

The important benefit of using a prism at a condition of minimum deviation is the symmetry of the system. Due to this symmetry, it is possible (by the proper

selection of the prism apex angle) to make incident and exit angles Brewster's angle. This eliminates Fresnel reflection losses for a p-polarized light beam. For the case of minimum deviation the resolving power of a prism can be expressed as:

$$R = (d_2 - d_1)\frac{dn}{d\lambda} \quad \textbf{(2.49)}$$

According to Eq. (2.47) and Eq. (2.49), a high dispersion glass should be used for the fabrication of a prism for spectroscopic applications.

Dispersion of optical glasses

Normally, glass dispersion is characterised in catalogues by the Abbe Number:

$$V = \frac{n_d}{n_f - n_c} \quad \textbf{(2.50)}$$

In Eq. (2.50) n_d, n_f and n_c are the glass refractive indices at the wavelengths of the Fraunhofer D-, F- and C- spectral lines (589.2 nm, 486.1 nm and 656.3 nm respectively). The higher the Abbe number, the lower material dispersion. For the fabrication of the dispersion prisms a SF glass is frequently used. It has Abbe number in the range 20 -30 and refraction index n_d=1.78, while the Abbe numbers of low dispersion (crown) glasses are in the range 55 - 70 [2.10]. In practice it is often required to know the refractive index of material at an arbitrary wavelength. For this purpose a glass dispersion formula can be used [2.9], [2.11]. It uses known refractive indices at different wavelengths to make interpolation within the specified wavelength range. One of the most common forms of the dispersion formula is the Sellmeier one:

$$n^2(\lambda) = 1 + \frac{B_1\lambda^2}{\lambda^2 - C_1} + \frac{B_2\lambda^2}{\lambda^2 - C_2} + \frac{B_3\lambda^2}{\lambda^2 - C_3} \quad \textbf{(2.51)}$$

Coefficients of the Eq. (2.51) for various optical glasses can be found in glass catalogues [2.10].

As an example, consider a prism made of SF11 glass. One can calculate the

size of the prism (used at the condition of minimum deviation) required to achieve a spectral resolving power of 1000 at a wavelength of 600 nm. Using Eq. (2.51) with the coefficients from [2.10] to calculate $\frac{dn}{d\lambda}$, one can obtain from Eq. (2.49) that the size of the prism base should be at least 7 mm to achieve this resolving power.

2.2.2.2 Diffraction grating

A diffraction grating is a collection of reflecting or transmitting elements arranged periodically and separated by a distance comparable with the wavelength of light [2.12]. The main property of the grating is that it introduces a periodic modulation (phase or/and intensity) in the wavefront of the incident light.

Grating equation.

There are different approaches to consider the effect of the grating on the incident light. The simplest one is to refer to each of the grooves as to a very small slit-shaped source of the diffracted light. The result of the interference of light from such sources is that there is a limited set of directions along which a diffracted wavefront can propagate. These directions are defined by the grating period and wavelength of light. This situation is demonstrated in Fig. 2-17.

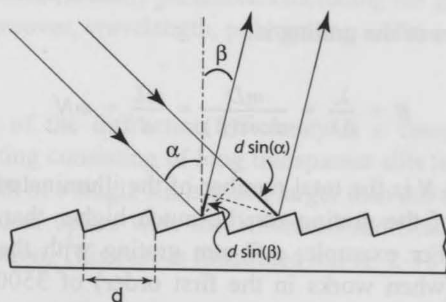

Fig. 2-17. Path difference between incident and diffracted light

Consider a reflective grating with period d and light with the wavelength λ falling on the grating at an angle α with the grating normal. Let the diffracted

light propagate in the direction at an angle β with the grating normal. The path difference between the light diffracted from the two adjacent grooves is (see Fig. 2-17): $d\sin(\alpha) - d\sin(\beta)$. Constructive interference is possible if the path difference is equal to the integer number of the wavelengths. This condition results in what is called grating equation:

$$d(\sin(\alpha) - \sin(\beta)) = m\lambda \tag{2.52}$$

In Eq. (2.52) m is an integer number defining the diffraction order. It follows from Eq. (2.52) that if m is not zero, the diffraction angle β depends on the wavelength. This implies the ability of the grating to spatially separate different spectral components of light.

Resolving power of the diffraction grating

The dispersion of a grating as follows from Eq. (2.52) is:

$$\frac{d\beta}{d\lambda} = \frac{m}{d\cos(\beta)} \tag{2.53}$$

The resolving power of the grating can be found using the same approach as in the section 2.2.2.1. The width of the diffracted beam $D = L\cos(\beta)$, where L is the illuminated length of the grating. According to the Rayleigh criterion (section 2.3.3), the diffraction broadening of the image should be equal to the spatial separation of the components λ_1 and λ_2: $\frac{m}{d\cos(\beta)} \times (\lambda_1 - \lambda_2) = \frac{\lambda}{D}$. Finally, the resolving power of the grating is:

$$R = \frac{\lambda}{\Delta\lambda} = \frac{mD}{d\cos(\beta)} = \frac{mL}{d} = mN \tag{2.54}$$

In Eq. (2.54) N is the total number of the illuminated grating grooves. The resolving power of the grating can be much higher than that of the prism of comparable size. For example, a 7 mm grating with the period of 2 μm has resolving power (when works in the first order) of 3500, while the resolving power of a prism with a 7 mm long base is only 1000 (see section 2.2.2.1).

Free spectral range.

Equation (2.52) can be solved for different values of λ and m, while keeping α and β constant. This means that the diffracted light at different wavelengths can propagate in the same direction being diffracted in different diffraction orders.

The range of the wavelengths diffracted in a given order for which overlapping from adjacent orders does not occur is called the Free Spectral Range (FSR). FSR can be calculated from its definition $m(\lambda_1 + \Delta\lambda) = (m+1)\lambda_1$ as:

$$FSR = \Delta\lambda = \frac{\lambda}{m} \tag{2.55}$$

The concept of FSR is especially important for gratings working in a high diffraction order (echelles), since free spectral range is inversely proportional to m. If the desired operating wavelength range is larger than the FSR, the additional wavelength selective elements such as wavelength filters (see 2.2.2.3) can be used to block the light from adjacent orders.

Grating efficiency

In practical applications, only a single diffraction order is typically used. That is why it is desired to direct as much energy as possible in to the order in use. The ratio of the light power in the given diffraction order to the power of the incident beam is called the diffraction efficiency of the grating in this order. The grating efficiency depends on many parameters including the grating material, the shape of the grating grooves, wavelength, polarization and the angle of incidence of light [2.12], [2.13].

The calculation of the diffraction efficiency is a complicated task. The simplest case of a grating consisting of long transparent slits in an opaque screen (provided that the width of a single slit is much larger than the wavelength) can be addressed using classical optics with the Kirchhoff's diffraction theory in the Fraunhofer approximation. This case is illustrated in Fig. 2-18

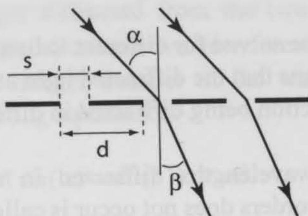

Fig. 2-18. Diffraction on a grating consisting of transparent slits in an opaque screen.

The calculation of the Kirchoff's diffraction integral results in:

$$J(p) \sim \left(\frac{\sin\left(\frac{kps}{2}\right)}{\frac{kps}{2}} \right)^2 \times \left(\frac{\sin\left(N \times \frac{kdp}{2}\right)}{\sin\left(\frac{kdp}{2}\right)} \right)^2 \qquad \textbf{(2.56)}$$

In Eq. (2.56) *J(p)* is the light intensity depending on the angle of incidence and diffraction via parameter $p = \sin(\alpha) - \sin(\beta)$, $k = 2\pi/\lambda$ is the wave vector of light, *d* and *s* are the grating period and slit width respectively. The left multiplier in Eq. (2.56) describes the result of the diffraction on a single slit, while the right multiplier is the result of interference from *N* slits in the grating.

The grating equation (2.52) follows directly from Eq. (2.56). Indeed, the left multiplier in Eq. (2.56) is a low oscillating function as compared to the right part. The function *J(p)* has a maximum if $\frac{kdp}{2} = n\pi$, n is an integer, and $dp = \frac{2\pi}{k}n$, which is identical to Eq. (2.52).

As an example, the result of a diffraction on a grating consisting of 20 slits in an opaque screen is shown in Fig. 2-19 and Fig. 2-20 for an incident angle of 5°, 25 μm grating period, 10 μm slit width and wavelength of 600 nm.

Figure 2-19 shows the effect of two multipliers in Eq. (2.56) separately and Fig. 2-20 - the result of multiple slits interference.

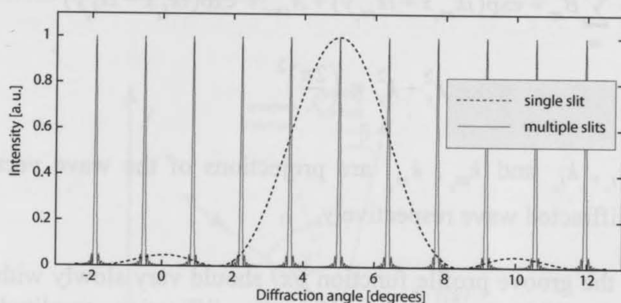

Fig. 2-19. Result of a diffraction on slits in an opaque screen.

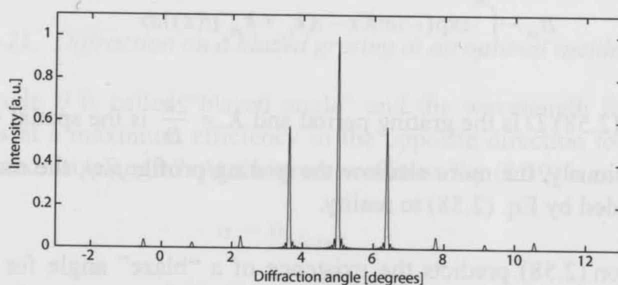

Fig. 2-20. Result of a diffraction on a grating consisting of slits in an opaque screen.

The sharp peaks in Fig. 2-20 correspond to different diffraction orders. The modulation due to a single slit diffraction function results in unequal intensities of diffraction orders.

The classical approach involving calculation of the Kirchoff's integral can also be extended on more complicated gratings using additional approximation called Rayleigh hypothesis. This approach is known as scalar theory. Considering a reflective or transmission grating with grooves profile described by a function $y = f(x)$, it assumes that the electromagnetic field can be described everywhere (outside the grating corrugated region as well as inside this region) by the sum of the incident wave and plane waves representing the diffraction orders [2.12] (plane wave expansion):

$$F = \sum_m B_m \times \exp(ik_{m_x}x + ik_{m_y}y) + A_{inc} \times \exp(ik_{i_x}x + ik_{i_y}y) \quad , \qquad k_x^2 + k_y^2 = \left(\frac{2\pi}{\lambda}\right)^2 \tag{2.57}$$

where k_{i_x}, k_{i_y} and k_{m_x}, k_{m_y} are projections of the wave vectors of the incident and diffracted wave respectively.

Further, the groove profile function *f(x)* should vary slowly with respect to the wavelength. With these assumptions the diffraction amplitudes can be evaluated in the form [2.12]:

$$B_m \sim \int_0^D \exp(-imKx - i(k_{i_y} + k_{m_y})f(x))dx \tag{2.58}$$

In Eq. (2.58) D is the grating period and $K = \frac{2\pi}{D}$ is the spatial vector of the grating. Obviously, the more shallow the grating profile *f(x)*, the more close the results provided by Eq. (2.58) to reality.

Equation (2.58) predicts the existence of a "blaze" angle for the gratings with a saw-tooth groove profile. Such a grating with a triangular-shaped grooves is shown in Fig. 2-21. The integral in Eq. (2.58) has maximum if the exponent factor is null. This condition is satisfied when the direction of diffraction of the m-th order (angle β in Fig. 2-21) coincides with the direction of light reflected from a single facet tilted at an angle θ (see Fig. 2-21): $(\alpha + \beta = 2\gamma)$.

Using grating equation (Eq. (2.52)) and simple geometrical considerations, the condition of maximum diffraction efficiency can be obtained as:

$$\cos(\alpha - \theta)\sin(\theta) = \frac{m\lambda}{2d} \tag{2.59}$$

Normally, commercially available gratings are specified in catalogues by a blazed angle and blazed wavelength at a Littrow condition (diffraction is in the opposite direction to the incident light, $\beta = -\alpha$) [2.14]. This implies that for a grating with a groove facet tilt angle θ, maximum efficiency is achieved for light at a specified wavelength falling at an angle θ with the grating normal and

diffracted in the opposite direction.

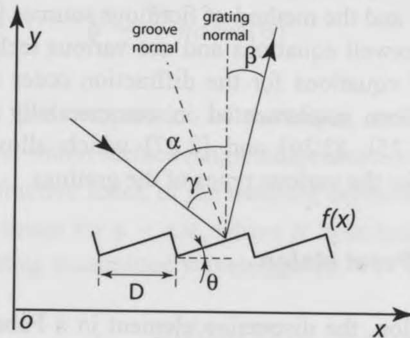

Fig. 2-21. Diffraction on a blazed grating at an optimal incident angle.

The angle θ is called "blazed angle" and the wavelength for which the diffraction is at a maximum efficiency in the opposite direction to the incident one is a "blazed wavelength". At a Littrow condition Eq. (2.59) is modified as:

$$\alpha = \theta_{blazed}$$

$$\sin(\theta_{blazed}) = \frac{m\lambda_{blazed}}{2d} \quad \textbf{(2.60)}$$

Although scalar theory had been applied to calculate efficiency of the gratings with a small wavelength/period ratio, such as transmission surface relief gratings [2.15] and perfectly conductive reflective gratings [2.16], [2.17], it is no longer valid when the grating period reduced to values close to wavelength. Moreover, the theory does not account for light polarization, while in the many cases the grating efficiency strongly depends on the state of polarization. Nevertheless, Kirchoff's diffraction theory provides qualitative description of the grating behaviour, which is a fundamental property of all gratings. For example, sharp peaks in the diffracted light corresponding to different diffraction orders and blazed angle defining the conditions for maximum diffraction efficiency.

There are several grating theories which are used for accurate calculation of the grating efficiency nowadays [2.13]. These are considered as "rigorous" methods in the sense that they are based on a numerical solution of Maxwell equations with boundary conditions without any theoretical approximations.

These theories have been developed since 1960's, when numerical computers had become available. The rigorous theories include the integral method [2.18], [2.19], the modal method [2.20], [2.21], the differential method [2.22], the finite - element method [2.23] and the method of fictitious sources [2.24]. In general, the methods start with Maxwell equations and use various techniques to arrive at a linear algebraic set of equations for the diffraction order amplitudes. Some of these methods have been implemented in commercially available simulation software packages [2.25], [2.26] and [2.27] which allow calculation of the diffraction efficiency for the various types of the gratings.

2.2.2.3 Fabry-Perot etalon

Fabry-Perot etalon, the dispersive element in a Fabry-Perot spectrometer consists of the two partially reflective and partially transmissive parallel plates (see Fig. 2-22).

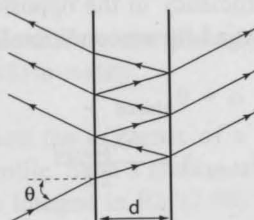

Fig. 2-22. *Reflections of a plane wave in a Fabry-Perot etalon.*

The light falling on a Fabry-Perot etalon experiences divisions of the wavefront into reflected and transmitted parts on each of the plates. These multiple wavefronts interfere with each other. Depending on the wavelength, the angle of light incidence and the distance between the etalon plates, the interference can be a constructive (wavefronts amplify each other) or destructive (wavefronts cancel each other) one. As a result of this interference, the optical transmittance of the etalon is given by the Airy formula [2.3]:

$$I(\phi) = \frac{I(0)}{1 + \frac{4r}{(1-r)^2}\sin(\phi)^2} \quad \textbf{(2.61)}$$

In Eq. (2.61) r is the reflection coefficient of the plate surfaces and ϕ is the phase:

$$\phi = \frac{2\pi}{\lambda} nd\cos(\theta) \tag{2.62}$$

In Eq. (2.62) d is the separation of the etalon surfaces, θ is the angle at which light falls on the etalon surface (angle of incidence), λ is the wavelength of light and n is the refractive index of the medium between plates. Transmittance of the etalon has maximum for $\phi = \pi N$, where N is an integer called interference order. The corresponding transmitted wavelength is:

$$\lambda = \frac{2nd\cos(\theta)}{N} \tag{2.63}$$

Since the transmittance of the etalon depends on the wavelength, it can be used as a spectral filter and the resolving power of the etalon follows from the Eq. (2.61) as:

$$R = \frac{2nd\cos(\theta)}{\lambda} \times \frac{\pi\sqrt{r}}{1-r} = N \times \frac{\pi\sqrt{r}}{1-r} \tag{2.64}$$

From Eq. (2.64) it is clear that the resolution is better for higher orders of interference and for more reflective (larger r) surfaces.

The transmittance function (Eq. (2.61)) is periodic in ϕ which implies that there are more then one wavelengths that a given etalon transmits provided that all parameters such as distance between plates and incident angle are fixed. The maximum spectral range $\Delta\lambda$ that contains only one wavelength λ_0 transmitted by etalon is called free spectral range (FSR). In other words FSR is the wavelength period of $I(\phi)$ and from Eq. (2.61) and Eq. (2.62) one can obtain:

$$\Delta\lambda = \frac{\lambda^2}{2nd\cos(\theta)} \tag{2.65}$$

2.2.3 Photodetector

The main function of an optical detector is to convert an optical signal into an electrical signal (voltage or current). Many different types of detectors are available. These are clamped in two groups: thermal detectors such as bolometers and thermoelectric detectors and photon detectors, such as photomultipliers and various semiconductor-based detectors [2.28]. The most suitable for application in a visible microspectrometer are silicon-based photon detectors arrays. There are following reasons for that:

- The pitch of the photon detectors array (the distance between the centers of the two adjacent photon detectors, or pixels) can be as small as 3 - 5 μm, which is extremely important in achieving a high resolution in a small-sized spectrometer, as will be discussed in the next chapters.
- Silicon photon detectors can be fabricated in a standard IC process. This implies that the integration of a photodetector array with additional read-out or processing circuits and MEMS structures is possible on the same silicon chip.
- Silicon detectors are very sensitive in the domain of visible light (the only more sensitive detector is a photomultiplier).
- Silicon detectors can be fabricated in a high volume process at a low price per single device.

The main building block of the silicon photosensors is a photodiode [2.29]. The operation principle of a simple p-n photodiode is illustrated in Fig. 2-23.

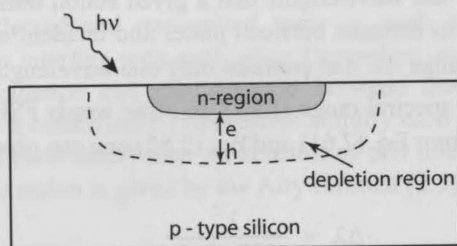

Fig. 2-23. *Separation of the photo-generated charge-carriers in a photodiode.*

The p-n junction is created in a silicon p-type substrate by implanting donor

atoms (typically phosphorus). Such a p-n junction results in a depletion layer and, as a consequence, in an internal electric field. When an absorbed photon generates an electron-hole pair in the depletion region, the internal electric field separates these photogenerated charge carriers accumulating a photo-generated charge. The amount of this charge is proportional to the intensity of the incident light.

The photodiodes can be arranged in a two- or one-dimensional array which can be fabricated on a planar silicon substrate together with the additional structures for read-out of the accumulated electric charge. This photo-generated charge can be read in various ways. There are currently two industry standards which implement different approaches to the read-out of a photodiode signal and also differ by the fabrication process steps. These are CMOS and CCD image sensors shown in Fig. 2-24.

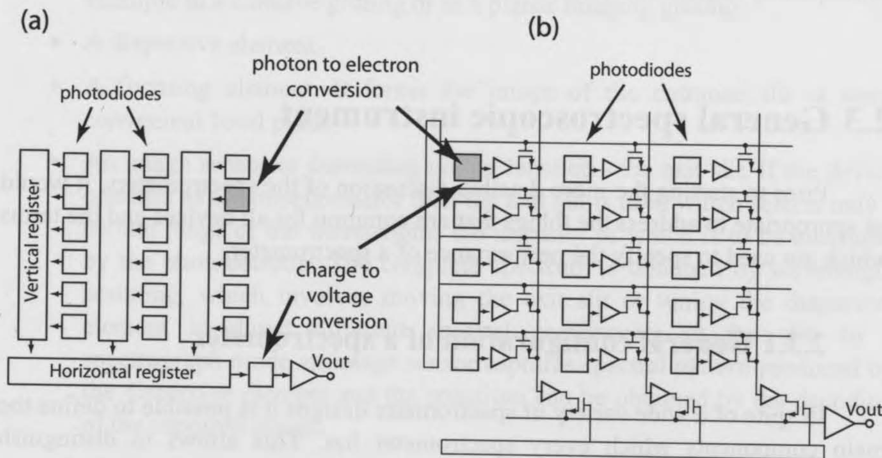

Fig. 2-24. Architecture of CCD (a) and CMOS (b) image sensors.

In a two dimensional CCD array metal electrodes in horizontal and vertical registers are used to create potential wells of variable depth for electrons by applying a certain voltage. During the acquisition of the image (exposure) the charge is accumulated in photodiodes. After that it is shifted from the photodiodes area to the potential well under metal electrodes in vertical registers. In the same way the charge is moved from the vertical registers to the horizontal one and then it is converted to voltage at the output. The pixels are read out one by one.

In a CMOS array, every photodiode is supplied with a circuit consisting of several transistors, which is used to convert charge to voltage and allow direct access to the pixels via column and row addressing. Thus, the fill factor (the ratio of the total chip area to the area of photodiodes) of the CMOS sensors is smaller than that of the CCD.

The advantage of CMOS sensors is that these can be fabricated in a standard process which is used for the fabrication of electronic chips. That is why CMOS photodetectors can be supplied with additional signal processing curcuits on the same chip.

An one-dimensional array of photodiodes is in principal sufficient in spectrometer applications. As it will be shown in the next chapters, an array of long and narrow pixels is desirable in most devices. The exception is imaging spectrometers which acquire a two-dimensional spectral distribution and consequently require two-dimensional arrays of photodetectors.

2.3 General spectroscopic instrument

Prior to starting the more detailed discussion of the spectrometers, it would be appropriate to address the things that are common for all devices and the terms which are used to specify the performance of a spectrometer.

2.3.1 General configuration of a spectrometer

In spite of a wide variety of spectrometer designs it is possible to define the main components which every spectrometer has. This allows to distinguish between different spectrometer types on the basis of the realization of those components.

The configuration of a generic spectroscopic device is presented in Fig. 2-25.

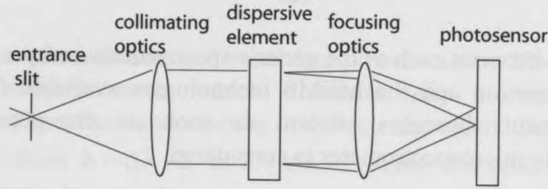

Fig. 2-25. Generic spectrometer.

The generic spectrometer includes [2.30]:

- An entrance aperture. Generally it is a narrow slit but, in principle, it could be of any shape.
- A collimating element. This element makes parallel all the rays passing through one point of the entrance slit. This element may be a lens or a mirror. It may also be an integrated part of the dispersive element as for example in a concave grating or in a planar imaging grating.
- A dispersive element.
- A focusing element. It forms the image of the entrance slit at some convenient focal plane.
- An image sensor or depending on the function - the exit slit. If the device operates as a monochromator then the exit slit is used which selects only a certain range of the wavelengths the intensity of which is to be measured by the photodetector. The complete spectrum is obtained by wavelength scanning, which involves moving the exit slit or tuning the dispersive element to direct different spectral components to the slit. In a spectrograph mode an image sensor captures spectral pattern produced by the dispersive element and the spectrum can be obtained by the decoding of the captured image.

The various types of spectrometers may differ by the dispersive element (prism, grating or Fabry-Perot etalon), by using image sensor (spectrograph) or exit slit (monochromator), by using lenses or mirrors for collimation and focusing or combining those functions with the dispersion in a single element (imaging grating). Since the goal of the research presented in this thesis is a very small, cheap and robust device, the moving parts can not be used in the design. This implies that this thesis is focused on a spectrograph-like devices using an array of photodetectors (or image sensor).

2.3.2 Realization of the spectrometer in microtechnologies

The link between each of the generic spectrometer components discussed in the previous section and the MEMS technologies available for fabrication of these components becomes evident as soon as the actual design of a manufacturable microspectrometer is considered.

Some of the optical components can be fabricated in an unaltered microtechnology. This applies especially to planar components, such as flat mirrors and detectors. For example, the spectrometer entrance slit can be easily implemented lithographically based on a highly reflective strip mirror surrounded by an anti-reflective surface, or as a window etched in an opaque material. The first approach was employed in the planar microspectrometers described in chapter 4, while the second approach was used in the microspectrometer presented in chapter 6. Imaging sensors are not investigated in this thesis, since the science of the design and fabrication of CCD or CMOS photon detectors is well developed nowadays.

Available microtechnologies are more restrictive when trying to implement a dispersion element. The microspectrometers described in this thesis employ diffraction gratings with a rectangular profile of the grooves. Such gratings were fabricated lithographically using two etching steps. This approach results in usable grating, however a superior optical performance would be possible using blazed gratings. The fabrication of such a blazed grating with a triangular groove profile is much more challenging and is not possible with a simple planar lithography. Since the grating was not the limiting factor, no attempts have been made to design a modified MEMS process for fabrication of a blazed gating.

Since MEMS processing does not easily allow fabrication of non-planar structures, the most challenging component from the fabrication point of view is collimating and focusing optics. The possible solutions include: 1. using the capability of a planar diffraction grating for imaging using curved and unequally spaced grooves (chapter 4), 2. adding a post-processing step to allow for the fabrication of a spherical element (chapter 5) or 3. using an external non-MEMS component - simple spherical mirror combined with a grating fabricated with microtechnologies and integrating these components in a microspectrometer at the packaging level (described in chapter 6).

2.3.3 Resolution and resolving power

The concept of resolution and resolving power can be illustrated on the example of a monochromator which transmits only a certain range of wavelengths in the spectrum and absorbs or reflects the others. Suppose that the selected range is from $\lambda - \Delta\lambda/2$ to $\lambda + \Delta\lambda/2$. Then the resolving power is defined as a dimensionless number:

$$R = \frac{\lambda}{\Delta\lambda} \tag{2.66}$$

Resolution can be defined simply as $\Delta\lambda$ and it is measured in nm. In a spectrometer that uses an image sensor to capture the spectrum in form of the intensity distribution, the resolution can be understood as follows. In such devices the spectral dependency of the optical intensity is mapped on an array of image sensor pixels and a particular wavelength is identified by a pixel number. Thus, image sensor output is converted into the dependency of the light intensity on the wavelength $S(\lambda)$. If the entrance aperture of the spectrometer is illuminated by the monochromatic radiation, then the common way to define resolution is to measure the width of the $S(\lambda)$ curve at the half of the maximum height as shown on the Fig. 2-26.

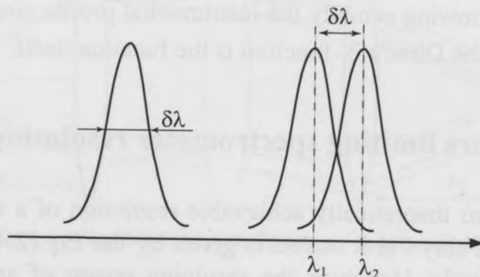

Fig. 2-26. Definition of the spectral resolution concept.

The resolution $\delta\lambda$ defined in this way is referred to as the "resolution Full Width Half Maximum" (FWHM). Two spectral lines of the wavelengths λ_1 and λ_2 can be resolved if the maximum of the curve corresponding to wavelength λ_1

coincides with the minimum of the curve corresponding to wavelength λ_2. Then the resolution of the spectrometer is defined as $\delta\lambda = \lambda_2 - \lambda_1$ (see Fig. 2-26). This condition is called the Rayleigh criterion.

2.3.4 Instrumental profile

The concept of the instrumental profile is closely connected with the resolution of a spectrometer. Consider a spectrum consisting of a single line at a wavelength λ_0. If such a spectrum is measured with a spectrometer the output of a perfect instrument would be $S(\lambda) = \delta(\lambda_0)$. However the output of a real spectrometer will be $S(\lambda) = \alpha \times F(\lambda_0, \lambda - \lambda_0)$, where α is a constant depending on the transmission of the spectrometer and the function F is called the instrumental profile. If the spectrum of a light source is described by the function $L(\lambda)$ then the output of the spectrometer is the convolution of this function with the instrumental profile:

$$I(\lambda) = a\int_0^{\infty} S(\lambda')F(\lambda', \lambda - \lambda')d\lambda' \tag{2.67}$$

It is now clear that the curves representing monochromatic spectral lines in the Fig. 2-26 are showing actually the instrumental profile since the convolution of a function with the Dirac's δ-function is the function itself.

2.3.5 Factors limiting spectrometer resolution

The maximum theoretically achievable resolution of a spectrometer using prism, grating or Fabry-Perot etalon is given by the Eq. (2.47), Eq. (2.54) and Eq. (2.64) respectively. However, the resolving power of an actually realized instrument is always smaller due to the optical aberrations and a finite non-zero width of the entrance aperture.

Figure 2-27 illustrates a spectrometer with an entrance slit of width d. The optical system images entrance slit with a certain magnification m onto the focal plane of the focusing lens. In the absence of aberrations the width of the slit

image D is proportional to the slit width d: $D = md$. Consider two wavelength of light: λ_1 and λ_2. If the angular dispersion of the dispersing element is φ, each point of the entrance slit creates two points in the image plane separated by distance $L = \varphi \times (\lambda_2 - \lambda_1) \times F_2$. Obviously, if $D > L$, λ_1 and λ_2 can not be resolved. To resolve these wavelengths, one has to make the entrance slit smaller. However, it is useless to make the width of the slit smaller than the diffraction limited value $d_0 = \frac{\lambda}{NA}$, where NA is the input numerical aperture of the entrance optics (see Eq. (2.35)). In the absence of aberrations, the image size can not be smaller than the diffraction limited value $D_0 = md_0$, and making the entrance slit width smaller than d_0 will only reduce the amount of light entering the system.

Another factor limiting spectral resolution is the aberrations of the spectrometer optical system. The width of the entrance slit image can be increased due to the optical aberrations (see section 2.2.1.2). In this case, the resolution is defined by the total width of the slit image which is $D = md + D_{aberr}$, where D_{aberr} is the aberration-induced image blurring.

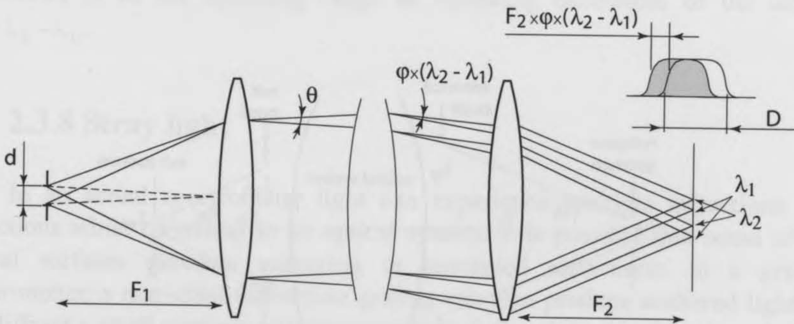

Fig. 2-27. Factors limiting the resolution of a spectrometer.

If D is the size of the entrance slit image which is defined by the factors discussed above, and φ is the angular dispersion of the dispersing element, the resolution of the spectrometer is:

$$R = \frac{\lambda}{\Delta\lambda} = \lambda\frac{\varphi \times F_2}{D} \quad \textbf{(2.68)}$$

If D in Eq. (2.68) is measured as FWHM, than the resolving power defined by this equation is also resolving power FWHM.

2.3.6 Etendue or throughput and etendue-resolving power product

Luminosity or throughput of the optical device defines the "light-gathering-power" of an instrument [2.30], the amount of light passing from the source through the instrument on to the detector. This amount depends on the area of the entrance pupil S_{ip} and the solid angle Ω subtended by the entrance aperture at the entrance pupil (entrance pupil can coincide with the collimator or illuminated area of dispersing element), see Fig. 2-28:

$$G = S_{ip} \times \Omega \tag{2.69}$$

It can be shown that etendue can also be expressed in terms of the numerical aperture and the entrance aperture area of the optical system (Fig. 2-28):

$$G = \pi \times S_{ia} \times NA_i^2 \tag{2.70}$$

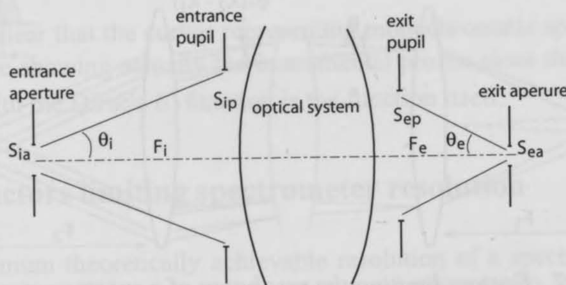

Fig. 2-28. Quantities defining the etendue of an optical system

Etendue is a fundamental property of the optical system that does not change as light propagates through the system. According to Fig. 2-28:

$$G = \pi \times S_{ia} \times NA_i^2 = \frac{S_{ia} \times S_{ip}}{F_i^2} = \frac{S_{ea} \times S_{ep}}{F_e^2} = \pi \times S_{ea} \times NA_e^2 \quad \textbf{(2.71)}$$

In Eq. (2.71) S_{ip}, S_{ep} and S_{ia}, S_{ea} are the areas of the entrance and exit pupils and entrance and exit apertures respectively and F_i and F_e are the corresponding distances between the pupils and apertures.

As was discussed in the previous section, the resolving power of a spectrometer is inversely proportional to the width of the entrance aperture (provided that the aberrations are small). That is why it is convenient to consider an etendue-resolving power product, *GR*. This value can be used as a measure of the spectrometer performance allowing to compare devices with different throughput and resolution.

2.3.7 Operating bandwidth

Suppose that the spectrometer is able to measure spectrum with the resolving power R in the region of wavelengths form λ_1 to λ_2. Then this region is referred to as the operating range or operating bandwidth of the device $\Delta\lambda = \lambda_2 - \lambda_1$.

2.3.8 Stray light

In an actual spectrometer light can experience multiple refractions and reflections while travelling in an optical system. It is possible that some of the optical surfaces generate scattering or unwanted reflections. In a grating spectrometer, a non-ideal diffraction grating can also produce scattered light or/ and diffract a small portions of light in additional directions (grating ghosts). As a result, there is an undesired light which strikes a photodetector. Such a light is called the “stray light” and results in the additional measurement noise or the fictitious spectral components.

2.4 Conclusions

In conclusion, the basic concepts which are necessary to understand the spectrometer operating principles are reviewed in this chapter. It is discussed that geometrical optics and ray tracing can be used to make an optical design of a spectrometer, while the performance of the spectrometer is simulated accounting for diffraction and using concepts of PSF and MTF. Prism, diffraction grating or Fabry-Perot etalon can function as a dispersive element in a spectrometer and the resulted spectral pattern is captured using CMOS or CCD photosensors.

These essential theoretical concepts reveal constraints when trying to reduce spectrograph dimensions: smaller does not necessary imply best optics. Finally, the best of both is one of the major challenges in micro-optics and in microspectrometers in particular.

References

[2.1] B. Bunch, A. Hellemans, *The history of science and technology*, Houghton Mifflin, Boston, 2004

[2.2] L. D. Landau, E. M. Lifshitz, *The classical theory of fields: Vol. 2 (Course of theoretical physics)*, Fourth Edition, Butterworth-Heinemann, Oxford UK, 1980

[2.3] J. M. Born, E. Wolf, *Principles of Optics*, Cambridge University Press, Cambridge, 1999.

[2.4] M. De Podesta, *Understanding the properties of matter*, Taylor and Francis, London, 2002.

[2.5] D. Meschede, *Optics, Light and lasers*, Wiley-VCH, Berlin, 2007.

[2.6] R. E. Fischer, B. Tadic-Galeb, P. R. Yoder, *Optical System Design*, McGraw-Hill, New York, 2008

[2.7] R. R. Shannon, *The art and science of optical design*, Cambridge University Press, Cambridge, 19971

[2.8] R. J. Noll, Zernike polynomials and atmospheric turbulence, *J. Opt. Soc. Am.* 66: 207-211, 1976

[2.9] ZEMAX Optical Design Program, User's Guide, Version 9.0 (Focus Software, Inc., Tucson, Ariz., 2000)

[2.10] Shott Optical Glass Data Sheets, Schott North America, Inc., www.us.schott.com

[2.11] H. Bach, N. Neuroth, *The properties of optical glass*, Springer Verlag, Berlin, 1998.

[2.12] E. G. Loewen, E. Popov, *Diffraction gratings and applications*, Marcel Dekker, New York, 1997

[2.13] M. Neviere, E. Popov, *Light propagation in periodic media*, Marcel Dekker, New York, 2003

[2.14] *http://www.edmundsoptics.com*

[2.15] E.K. Popov, L.V. Tsonev and E.G. Loewen, Scalar theory of transmission relief gratings , *Opt. Comm.* 80: 307-311, 1991

[2.16] E. G. Loewen, M. Nevière, and D. Maystre, On an asymptotic theory of diffraction gratings used in the scalar domain, *J. Opt. Soc. Am.* 68: 496-502, 1978

[2.17] R. D. Hatcher and J. H. Rohrbaugh, Theory of the Echelette Grating. I, *J. Opt. Soc. Am.* 46: 104-110, 1956

[2.18] H. A. Kahlor and A. R. Neureuther, Numerical Method for the Analysis of Diffraction Gratings, *J. Opt. Soc. Am.* 61, 43-48 (1971)

[2.19] D. Maystre, A new general integral theory for dielectric coated gratings, *J. Opt. Soc. Am.* 68: 490-495, 1978

[2.20] M. G. Moharam and T. K. Gaylord, Rigorous coupled-wave analysis of metallic surface-relief gratings, *J. Opt. Soc. Am. A* 3: 1780-1787, 1986

[2.21] D. M. Pai and K. A. Awada, Analysis of dielectric gratings of arbitrary profiles and thicknesses, *J. Opt. Soc. Am. A* 8: 755-762, 1991

[2.22] P. Vincent, Differential methods, in *Electromagnetic Theory of Gratings*, R. Petit, ed., Springer-Verlag, Berlin, 1980

[2.23] T. Delort and D. Maystre, Finite-element method for gratings, *J. Opt. Soc. Am. A* 10: 2592-2601, 1993

[2.24] G. Tayeb, R. Petit and M. Cadilhac, Synthesis method applied to the problem of diffraction by gratings: the method of fictitious sources, SPIE vol. 1545 International Conference on the Application and Theory of Periodic Structures, 95-105, 1991

[2.25] *http://www.rsoftdesign.com*

[2.26] *http://www.pcgrate.com/about/pcgrates*

[2.27] *http://www.holograte.com/eng/pcgrate.htm*

[2.28] J. Wilson, J. Hawkes, *Optoelectronics: an introduction.*, Prentice Hall Europe, Harlow, 1998

[2.29] H. Zimmerman, *Silicon optoelectronic integrated ciruits*, Springer-Verlag, Berlin, 2004

[2.30] John James, *Spectrograph design fundamentals*, Cambridge University Press, Cambridge, 2007.

3. Various approaches to spectral measurements

The state-of-the-art in microspectrometers is reviewed in this chapter and different approaches are discussed, including Fabry-Perot, Fourier-Transform, prism, grating, waveguide spectrometers and devices using photonic crystals. The choice of the grating as a basis for the development of the microspectrometer in this thesis is proved.

3.1 Prism spectrometers

Typical configurations of a prism spectrometer using refractive and reflective optics are shown in Fig. 3-1(a) and Fig. 3-1(b) respectively [3.1], [3.2].

According to section 2.3.6, the etendue of a prism spectrometer is:

$$G = \pi \times NA^2 \times w \times l = \frac{1}{4} \times \pi \times H \times D \times \Delta\gamma \times \Delta\beta \qquad (3.1)$$

In Eq. (3.1) NA is the input numerical aperture of the spectrometer, w and l are the width and height of the entrance slit respectively, H is the height of the prism, D is the width of the output beam and $\Delta\gamma$ and $\Delta\beta$ are the angular height and

width of the output slit respectively. This equation is illustrated in Fig. 3-2.

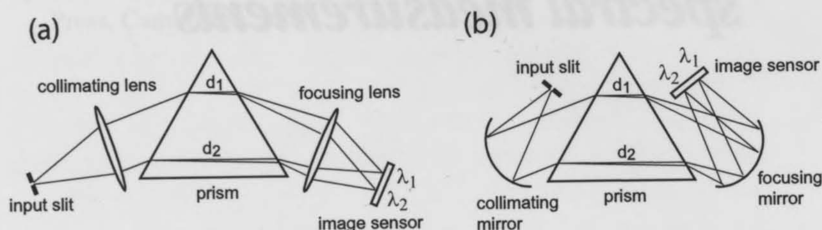

Fig. 3-1. *Prism spectrometers using refractive (a) and reflective (b) imaging optics.*

From Eq. (2.49): $\Delta\beta = \frac{L}{D} \times \frac{dn}{d\lambda} \times \Delta\lambda$. Substituting this in Eq. (3.1) and multiplying by $R = \frac{\lambda}{\Delta\lambda}$ one can obtain:

$$GR = \frac{\pi}{4} \times A \times \frac{dn}{d\lambda} \times \lambda \times \Delta\gamma \quad \textbf{(3.2)}$$

Thus, for a prism spectrometer, the etendue-resolving power product is proportional to the prism base area $A = L \times H$ and to the dispersion of the prism material.

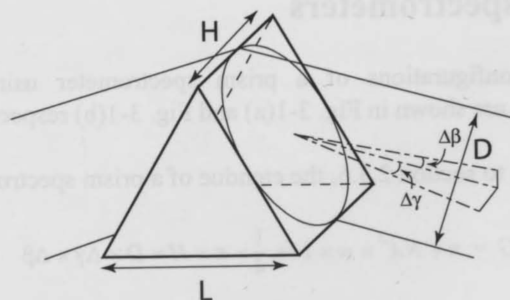

Fig. 3-2. *Parameters for the calculation of a prism-based spectrometer etendue.*

The etendue-resolving power product of the prism spectrometers is smaller than that of grating-based or fabry-perot spectrometers of comparable size, as will be discussed later. That is why the applications of prism spectrometers are limited. However, the prism spectrometers were used in the past because at that time due to imperfections of the grating fabrication technologies a prism was able to provide a superior performance within certain wavelength regions in terms of the stray light and efficiency. Prism spectrometers had been designed for vacuum UV regions where the dispersion of some of the transmission materials become higher [3.3]. In a wide infrared region from about 2 μm to 25 μm the usage of gratings becomes complicated due to overlapping of different diffraction orders, which determined the use of a prism as a dispersive element [3.4] or as an order-sorter attached to a grating-based spectrometer [3.5]. Nowadays, prisms are used mainly in simple low-resolution spectroscopy applications [3.6].

3.2 Grating spectrometers

The properties of a plane grating consisting of a number of straight parallel grooves are discussed in section 2.2.2.2. Such a grating can be used in a spectrometer with auxiliary collimating and focusing optics. The goal of the optical design is to reduce optical aberrations to exploit the inherent resolving power of the grating as much as possible, and there is always a trade-off between the performance and complexity (and consequently, cost) of the device. Spherical mirrors can usually provide a reasonable compromise. The examples of a Czerny-Turner [3.7] and Littrow [3.8] spectrometer configurations using spherical mirrors are shown in Fig. 3-3(a) and Fig. 3-3(b) respectively.

A grating fabricated on a non-planar substrate (typically spherical, but toroidal or other shapes are also possible) has imaging properties [3.9]. The advantage of such a grating is that the number of spectrometer components is reduced, since no auxiliary optics is required. The configuration of a concave-grating based spectrometer is illustrated in Fig. 3-3(c). Concave gratings will be considered in more details in chapter 5, and it will be shown, that although there are no collimating and focusing optics, a concave grating is not free from inherent aberrations, and special attention has to be devoted to the grating design.

As it will be discussed in details in chapter 4, a plane grating with curved and not-equally spaced grooves also has imaging power and can be used in a

spectrometer system without additional optics. However, the aberrations of such a grating are low in a relatively narrow wavelength bandwidth provided that the numerical aperture of the spectrometer is not high. That is why planar imaging gratings are suitable for applications which do not require high throughput and wide operating wavelength range.

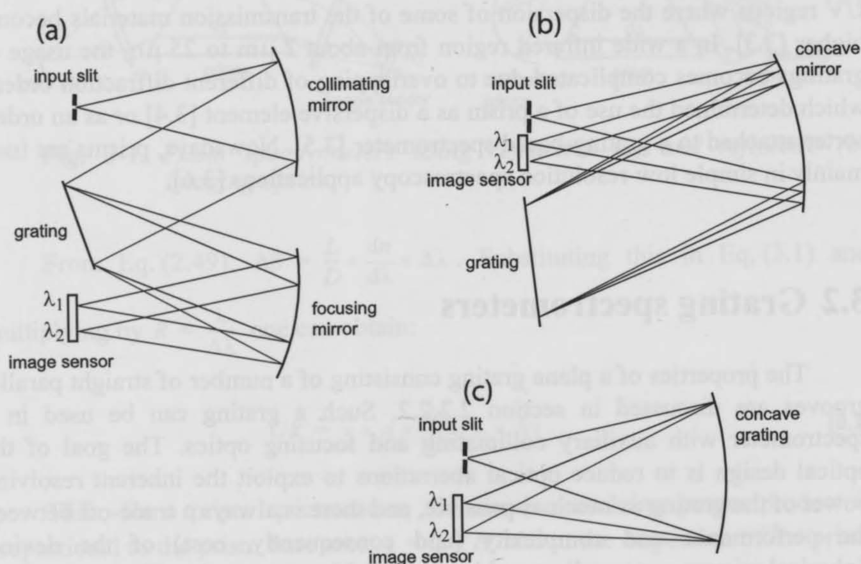

Fig. 3-3. *Grating spectrometers: Czerny-Turner (a) and Littrow (b) mountings of a plane grating and a concave-grating spectrograph (c).*

The etendue - resolving power of a grating spectrometer can be derived in the same way as it was done for a prism one:

$$GR = \frac{\pi}{4} \times S \times \frac{m}{d} \times \lambda \times \Delta\gamma \tag{3.3}$$

In Eq. (3.3) S is the area of the grating, m is the diffraction order and d is the grating period.

The comparison of Eq. (3.2) and Eq. (3.3) gives (assuming $S = A$):

$$\frac{(GR)_{prism}}{(GR)_{grating}} = \frac{d}{m}\frac{\mathrm{d}n}{\mathrm{d}\lambda} \tag{3.4}$$

Equation (3.4) shows that the grating in most cases is superior to the prism. For example, the dispersion of a SF11 glass prism which is discussed in section 2.2.2.1 is about 0.14 μm^{-1}, and typical values of period of a grating for the visible region are in a 1 - 2 μm range. Which implies, that the etendue-resolving power product is 3.5 - 7 times larger for grating spectrometers than for prism ones.

Diffraction gratings have been implemented in a huge number of different spectroscopy systems [3.10]. Planar gratings with a rectangular profile can be fabricated in a simple MEMS process, which suggests the applications of the gratings in microdevices. For example, plane imaging gratings have been considered to perform optical interconnection between different components integrated on a planar substrate [3.11], [3.12].

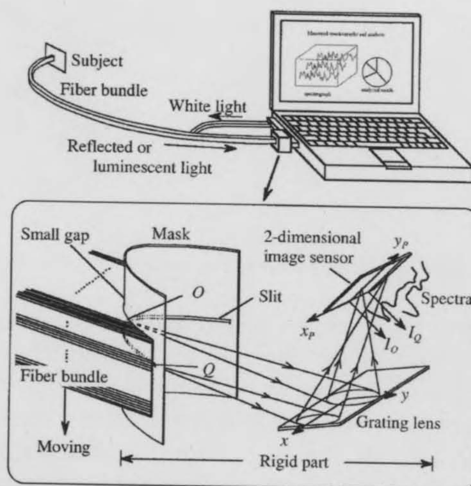

Fig. 3-4. Planar imaging grating used in a multi-channel compact spectrometer [3.13].

Imaging gratings which allow to avoid the use of auxiliary optics are very suitable for application in miniaturized spectrometer systems. Such a system using a grating fabricated with e-beam lithography had been demonstrated in

[3.13]. The fiber bundle illuminated the long slit in a concave mask as shown in Fig. 3-4. The concave mask was used to reduce aberration resulting from a large field of view. The size of the spectrometer module was about 1cm^3 and spectral resolution of the system was 5 nm in a 100 nm wavelength range.

A three-color imaging miniature system based on planar gratings had been described in [3.14] (see Fig. 3-5). The first grating (CSGL - color separation grating lens) was used for spatial separating of the colors, so that each color illuminated a separate region of the second grating (image correction grating, ICG). The imaging power of the ICG allowed an aberration corrected imaging of these three colors on the image sensor.

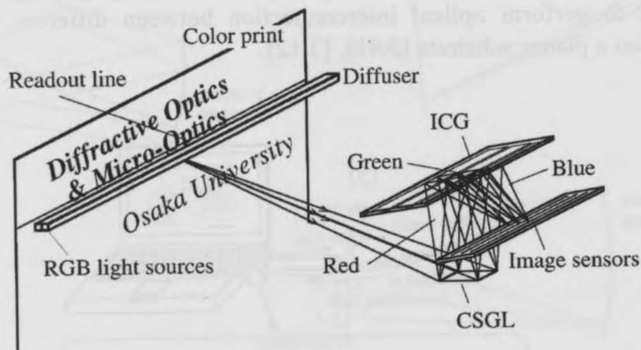

Fig. 3-5. *Double grating three-color imaging system [3.14].*

Although there are examples of the free-space grating-based miniaturized spectrometers, the most of the attention of the researches was devoted to the development of the microdevices which integrate a grating in a planar waveguide and usually referred to as waveguide spectrometers. Potentially, the waveguide spectrometers can provide the higher level of the components integration. However, these are most suitable for applications in the integrated optics for the analysis of light which was generated inside the waveguide (for example in telecom demultiplexers or photonic integrated circuits). This is due to the high losses when light is coupled into the waveguide from a free space.

3.3 Waveguide spectrometers

The principle of the operation of a waveguide is illustrated in Fig. 3-6. Typically, a waveguide consists of three layers with the refractive indices n_1 and n_2 (optical fiber, or cylindrical waveguide, consists of two concentric cylinders with different refractive indices). If the refractive index of the middle layer n_2 is larger than the refractive index of the outer layers n_1, the total internal reflection at the boundary of these layers is possible and light propagates in the middle layer as shown in Fig. 3-6. The maximum input angle θ of the incident light at which the total internal reflection occurs in the waveguide defines the numerical aperture of the waveguide as $NA = n\sin(\theta)$. From simple geometrical considerations it follows that $NA = \sqrt{n_2^2 - n_1^2}$. The adequate description of the electromagnetic field in the waveguide can be obtained by solving Maxwell equations. Depending on the waveguide thickness, layer refractive indices and the wavelength one or more solutions are possible. These solutions represent the different possible states of the electromagnetic field in a waveguide which are called the waveguide modes. In a simplified approach, the different modes correspond to different propagation angles φ (see Fig. 3-6).

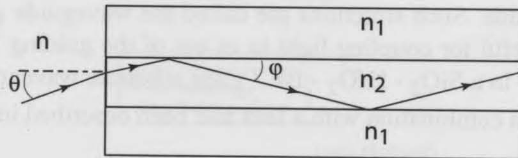

Fig. 3-6. *Total internal reflection in a waveguide.*

For the near-infrared region the waveguides can be fabricated on a SOI (silicon on insulator) wafer with the guiding layer of silicon between two cladding layers of silicon oxide [3.15]. In the visible region a glass wafer can be used with a hafnium oxide layer for waveguiding [3.16].

A planar waveguide can be considered as a two-dimensional optical system. A diffraction grating can be created in the waveguiding or cladding layer by introducing a periodic modulation of the layer optical properties (for example, periodic modulation of the layer refractive index or thickness).

An example of a waveguide spectrometer is described in [3.17]. The spectrometer system illustrated in Fig. 3-7 had been implemented in a polymer waveguide and was able to separate 10 spectral channels with a 20 nm spectral resolution in the range 700 nm - 900 nm. The concave diffraction grating which was fabricated by a deep-etching process provided both dispersion and imaging functionality (compare Fig. 3-7 and Fig. 3-3(c)). A similar system has been also described in [3.18] and a waveguide spectrometer using a transmission grating and external photodetector array has been reported in [3.19].

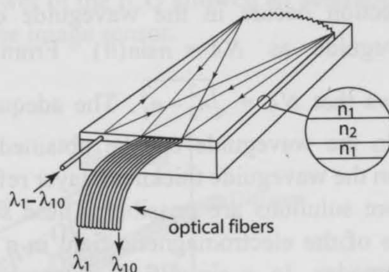

Fig. 3-7. *Waveguide demultiplexer using concave grating [3.17].*

Grating can also be fabricated in an upper cladding layer to diffract the light out of the waveguide. Such structures are called the waveguide grating couplers since these are useful for coupling light in or out of the guiding layer. A grating coupler fabricated in a SiO_2 - HfO_2 - BK7 glass substrate waveguide and used as a spectrometer in a combination with a lens had been described in [3.20].

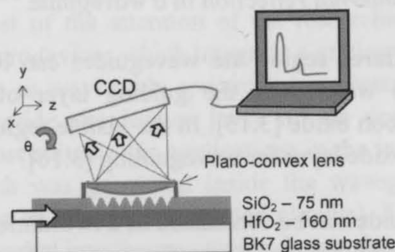

Fig. 3-8. *Spectrometer based on a waveguide grating coupler used in a combination with a lens [3.20].*

The linear periodic grating was etched in a silicon oxide cladding layer and the lens performed imaging functions as shown in Fig. 3-8. The largest dimension of the system was about 1.5 - 2 cm and the resolution varied from 0.3 nm to 4.6 nm within the range from 488 nm to 632 nm. This concept was developed further in [3.21], where an imaging grating coupler was proposed to perform imaging functions thus eliminating the need for using a lens as shown in Fig. 3-9. In order to reduce diffraction effects authors proposed to mount a microprism on top of the grating. The wavelength inside the prism is smaller than in the air, which results in a smaller diffraction broadening of the focused light. Thus it would be possible to obtain a higher resolution. The numerical simulations predicted 2 nm spectral resolution in a 300 nm range.

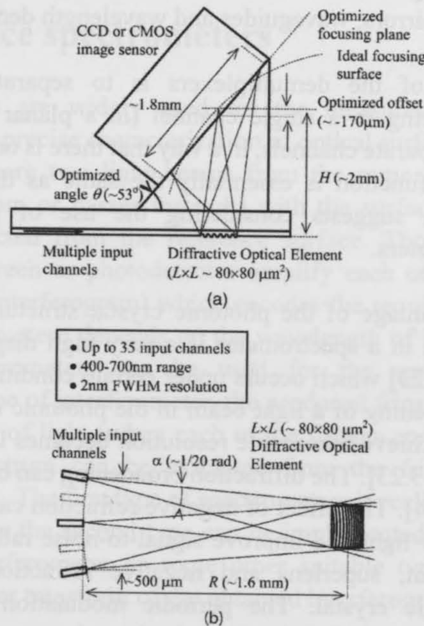

Fig. 3-9. *Side (a) and top (b) view of the waveguide grating coupler spectrometer proposed in [3.21].*

3.4 Spectrometers using photonic crystal structures

Photonic Crystals (PhC) are artificial structures with periodically modulated dielectric (and magnetic) permittivity. This modulation can be induced along one, two or three directions in space and the modulation period is smaller (or comparable) than the wavelength of light. The propagation of a light wave in a media with periodic dielectric and magnetic permittivity is similar to the propagation of an electron in the periodic potential field of a crystal. The principles that govern the behaviour of electrons in crystals are also applicable to the propagation of photons in PhC [3.22]. That is why it is possible to design materials with the desired dispersion properties. Such a possibility is very attractive and provides a potential for using photonic crystals in many applications including semiconductor lasers and amplifiers, wavelength filters and high reflection mirrors, waveguides and wavelength demultiplexers.

The function of the demultiplexers is to separate light at different wavelength propagating in a single channel (in a planar waveguide or in an optical fiber) in to separate channels, in a way that there is only one wavelength in each channel. This function is essentially the same as the task of an optical spectrometer, which suggests considering the use of photonic crystals in waveguide spectrometers.

The main advantage of the photonic crystal structures when considering these for application in a spectrometer is a very high dispersion known as the superprism effect [3.23] which occurs under certain conditions. However, due to the diffraction broadening of a light beam in the photonic crystal, an area of the device required to achieve reasonable resolution becomes large (order of several square centimetres) [3.23]. The diffraction broadening can be compensated with a superlens effect [3.24]. The effect of negative refraction can be used to decrease the level of the stray light and improve signal-to-noise ratio [3.25]. Figure 3-10 illustrates superprism, superlens and negative refraction effects in a two-dimensional photonic crystal. The periodic modulation in this structure is achieved by etching an array of circular holes in a planar waveguide.

A structure of the photonic crystal demultiplexer can be designed to have all the three effects illustrated in Fig. 3-10. Practical realizations demonstrated a device capable to separate 4 channels with the resolution of 8 nm in the wavelength region of 1500 nm [3.25]. However, the cross-talk between the channels was about 6.5 dB and the device worked only with the polarized light.

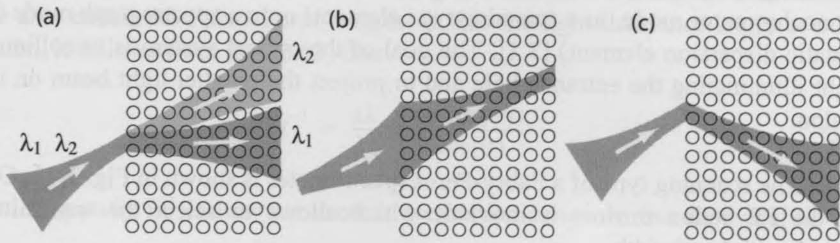

Fig. 3-10. *Illustration of superprism (a), superlens (b) and negative refraction (c) effects in a two-dimensional photonic crystal [3.25].*

3.5 Interference spectrometers

Interferometers are widely used for the measurements of very small distances and for the precise characterization of optical surfaces [3.26]. The basic principle is to compare two light beams from the same source one of which interacts (reflects from or passes through) with the surface of interest and the second one is reflected from the reference surface. Those two beams when combined on the screen or photodetector amplify each other producing fringe pattern (also called interferogram) which encodes the required information. It is obvious that such a pattern depends on the wavelength of interfering light. This implies that interferometers can be used for the spectral measurements. Depending on the type of interferometer, the produced fringe pattern can directly present the spectrum of light (when each of the fringes corresponds to a certain wavelength) or spectrum can be extracted from the fringe pattern using a numerical algorithm. The first type of spectrometers is realized with Fabry-Perot interferometers, while the second type can be implemented using Michelson (or lamellar-grating interferometer or some other suitable type of interferometer) combined with Fourier transform of the obtained interferogram.

3.5.1 Fabry-Perot spectrometers.

The theory of a Fabry-Perot interferometer (FP etalon) was reviewed in chapter 2, section 2.2.2.3. Equation (2.63) shows that both variation of the incident angle and variation of the distance between plates can be used for the

wavelength discrimination. Generally, the Fabry-Perot etalon is used either in a monochromator mode (as a scanning type element) or in a spectrograph mode (as a static dispersion element) [3.1]. The goal of the optical system is to collimate light illuminating the entrance hole and to project the parallel light beam on the etalon.

The scanning type of a Fabry-Perot spectrometer is shown in Fig. 3-11. One of the FP etalon mirrors is movable which allows to select the transmitted wavelength bandwidth.

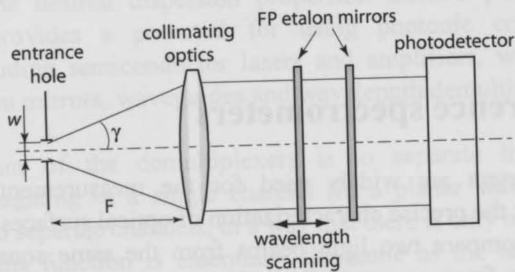

Fig. 3-11. *Scanning Fabry-Perot spectrometer.*

The principle of a Fabry-Perot spectrograph is illustrated in Fig. 3-12. This type of spectrographs is intended to measure extended light sources. Light emitted from different points of such a source makes different angles with the etalon axis after collimation as shown in Fig. 3-12.

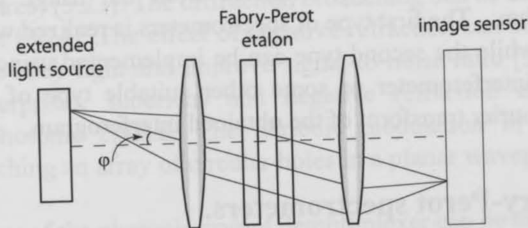

Fig. 3-12. *Fabry-Perot spectrograph.*

Since the etalon transmission function depends on the light incident angle (Eq. (2.63)), the resulting pattern observed in the image plane of the spectrograph

is a set of concentric circles corresponding to different wavelengths. Such circles are also called the Fabry-Perot fringes. If θ is the light incidence angle at a FP etalon, it follows from Eq. (2.63) that:

$$R^{-1} = \frac{\Delta\lambda}{\lambda} = \frac{\Delta(\cos(\theta))}{\cos(\theta)} \quad \textbf{(3.5)}$$

Typically FP etalons are used at normal incidence. In this case $\cos(\theta) \approx 1$, $\Delta\cos(\theta) = 1 - \cos(\theta_s) \approx \theta_s^2/2$ and resolving power becomes $R = 2/\theta_s^2$, where θ_s is a semi-angle defined by half-width of the entrance aperture. The dependence of the Fabry-Perot etalon transmission function on the incident angle defines the axial symmetry of a Fabry-Perot spectrometer. That is why instead of a slit as in the case with the grating or prism based devices it uses a circular entrance aperture. If w is the diameter of this aperture (see Fig. 3-11), the etendue-resolving power product of a Fabry-Perot spectrometer is defined as follows:

$$GR = \pi \times \frac{\pi w^2}{4} \times (NA)^2 \times R = \frac{\pi}{4} \times S \times (\Delta\theta)^2 \times \frac{2}{\theta_s^2} = 2\pi S \quad \textbf{(3.6)}$$

Comparing equations Eq. (3.3) and Eq. (3.6), one can obtain (provided the areas of the grating and FP etalon are equal):

$$\frac{(GR)_{FP}}{(GR)_{grating}} = \frac{8}{\Delta\gamma \frac{m\lambda}{d}} \quad \textbf{(3.7)}$$

The values of $(m\lambda)/d$ are typically in the range 0.2 - 2 (2 is an extreme case) and it is very difficult to make $\Delta\gamma$ larger than 0.1 [3.27]. Thus the etendue of a Fabry-Perot spectrometer is always at least 40 times larger than the etendue of a grating one.

Fabry-Perot spectrograph can be realized with a two-dimensional photodetector array such as a CCD camera to capture interference circular fringes [3.28], while scanning Fabry-Perot spectrometers traditionally used piezo-electric actuators to adjust the distance between FP etalon mirrors [3.29]. However, with the development of MEMS technologies it had become possible to implement a tunable FP resonator in silicon using electrostatic actuation principle. Fabry-Perot MEMS microinterferometers for the infrared [3.30] and visible [3.31] spectral

regions had been described. Such a system described in [3.31] is illustrated in Fig. 3-13. It consists of two processed silicon wafers. The first wafer includes a deflectable silicon nitride membrane with a silicon frame to ensure the membrane flatness and a silver mirror deposited on the membrane. The second wafer includes a static membrane with a silver mirror. The two wafers had been bonded and the distance between the membranes were adjusted electrostatically by applying voltage to aluminium electrodes deposited on silicone around the membranes.

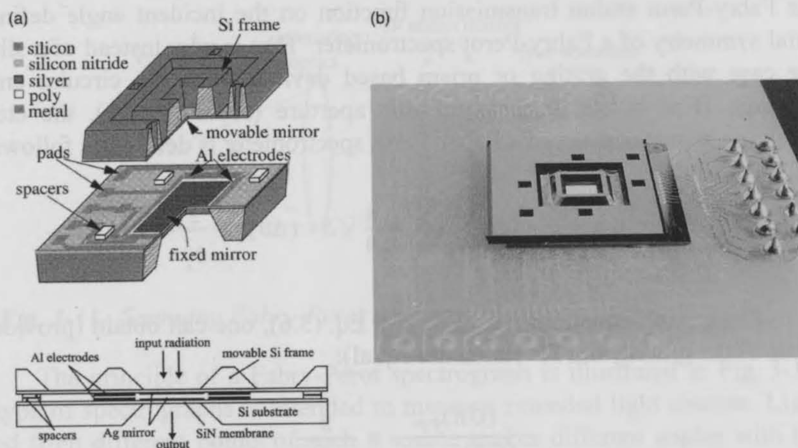

Fig. 3-13. *Cross-sectional view (a) and photograph (b) of a MEMS scanning Fabry-Perot microinterferometer [3.31].*

The main problem in a MEMS FP tunable filter with a moving membrane is to maintain a parallelism between the static and movable membranes, which results in a reduced spectral resolving power. This problem is absent in a static FP filter, which suggests a spectrometer design as an array of static FP filters.

Such an approach had been implemented in the device described in [3.32], which is shown in Fig. 3-14. An array of FP filter structures consisting of metal mirrors and SiO_2 spacer had been deposited on top of the CMOS chip containing photodiodes and read-out circuits.

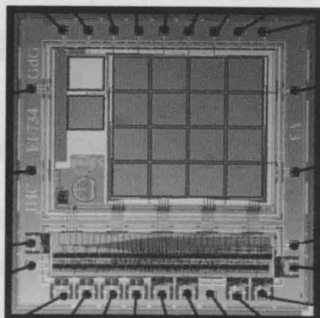

Fig. 3-14. *16-channel CMOS Fabry-Perot filter array integrated with photodiodes and read-out circuits [3.32].*

Although Fabry-Perot spectrometers can provide a high spectral resolution, the resolving power of MEMS based devices does not exceed 50 [3.31] due to the various problems such as the difficulties in achieving parallelism between FP etalon mirrors or technological problems in obtaining high quality mirrors [3.32].

3.5.2 Fourier Transform spectrometers.

One of the realizations of the Fourier Transform Spectrometer (FTS), which is based on the Michelson interferometer, is shown in Fig. 3-15.

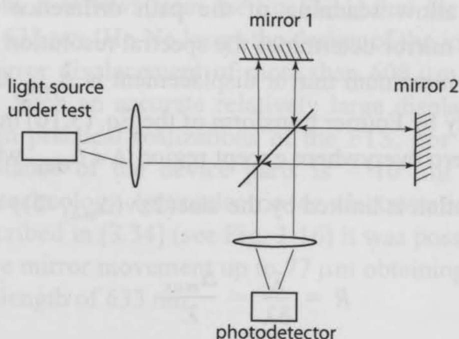

Fig. 3-15. *Michelson interferometer.*

The light from a source is divided by a beamsplitter as shown in Fig. 3-15. Two separated beams travel different paths and after the recombination on the beamsplitter these are focused on a photodetector. The transmission of this system for the monochromatic light is [3.33]:

$$I(\Delta) = (I_0/2) \times (1 + \cos(2\pi\nu\Delta)) \tag{3.8}$$

where I_0 is the intensity of the input light, Δ is the path difference and $\nu = 1/\lambda$ is the wavenumber. The variable part of the function $I(\Delta)$ in Eq. (3.8) is called the interferogram:

$$J(\Delta) = I_0 \times \cos(2\pi\nu\Delta) \tag{3.9}$$

If the input light is not monochromatic and described by the spectral distribution $S(\nu)$, the interferogram becomes

$$J(\Delta) = I_0 \int_0^{\infty} S(\nu)\cos(2\pi\nu\Delta)d\nu \tag{3.10}$$

From Eq. (3.10) it is clear that the interferogram is a Fourier pair of $S(\nu)$. Thus, if $J(\Delta)$ can be measured, it is possible to recover $S(\nu)$ by performing Fourier transform numerically. In practice the measurement of $J(\Delta)$ means that one of the mirrors in the interferometer (mirror 1 or mirror 2 in Fig. 3-15) must be made movable to allow scanning of the path difference Δ. The maximum displacement of the mirror determines the spectral resolution achievable with the FTS. Indeed, if the maximum mirror displacement is Δ_{max} then the spectrum is obtained numerically by Fourier transform of the Eq. (3.10) multiplied by the step function which is zero everywhere except region $\Delta < \Delta_{max}$ where it is equal to *1*. Thus spectral resolution is limited by the $\mathrm{sinc}(2\pi\nu(\Delta_{max}/2))$ and

$$R = \frac{\lambda}{\delta\lambda} = \frac{\Delta_{max}}{\lambda} \tag{3.11}$$

In practice, the interferogram $J(\Delta)$ is always a sampled function. The sampling interval δ defines the operating bandwidth of the FT spectrometer. If the

spectrum lies in the region from ν_1 to ν_2 then the interval between measurements should be $1/(2(\nu_2 - \nu_1))$ as follows from the properties of the Fourier transform.

If h is the diameter of the interferometer entrance aperture and F is the focal distance of the collimating optics, the path difference is defined with the uncertainty $\delta\Delta = \Delta \times \frac{h^2}{8F^2}$. Then from the Eq. (3.8) the resolving power of the interferometer is:

$$R = \frac{8F^2}{h^2} \tag{3.12}$$

Taking Eq. (3.12) into account, the etendue-resolving power product of the Fourier-Transform spectrometer is proportional to the area of the entrance pupil S:

$$GR = 2\pi S \tag{3.13}$$

Equation (3.13) is identical to Eq. (3.6). These express the inherent property of the interference spectrometers known as Jacquinot advantage [3.27] which states that the etendue-resolving power product of the interference spectrometers is higher than that of grating or prism spectrometers.

Practical realizations of Fourier Transform microspectrometers are rather limited. For example, it follows from the Eq. (3.11) that for the visible range at the wavelengths of 632 nm (He-Ne laser) the design of the interferometer should allow maximum mirror displacement of more than 600 μm to provide spectral resolution R=1000. Such an accurate relatively large displacement is the main technical problem in practical realizations of the FTS. For MEMS devices the typical moving distance of the device parts is ~ 10 μm determined by the available actuator technology (piezoelectric or electrostatic). With the clever actuator design described in [3.34] (see Fig. 3-16) it was possible to increase that distance and achieve mirror movement up to 77 μm obtaining spectral resolution of 5.2 nm at a wavelength of 633 nm.

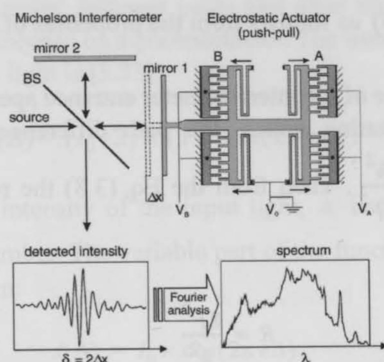

Fig. 3-16. *Schematic of the MEMS Michelson interferometer used in a Fourier-Transform spectrometer. Electrostatic actuator is used to move the interferometer mirror [3.34].*

Another implementation of the Fourier transform spectrometer uses a Lamellar Grating Interferometer (LGI) [3.35] to produce a wavelength dependent interferogram [3.36], [3.37]. In a LGI a grating is used to divide the incident wavefront by reflection from the upper and lower sides of the grooves. The grating consists (see Fig. 3-17 (a)) of the fixed fringes (1), movable fringes (2) connected to the rigid backbone (3) and springs (4) which allow electrostatically induced displacement of the backbone changing the depth of the grating profile d (see Fig. 3-17 (b)).

The intensity of the diffracted light for small angles of diffraction obeys the following proportionality [3.35]:

$$I \sim \cos\left(\frac{2\pi d}{\lambda}\right) \tag{3.14}$$

Equation (3.14) contains the cosine dependence on d which means that the Fourier transform of measured interferogram $I(d)$ will give spectrum of light incident on the grating.

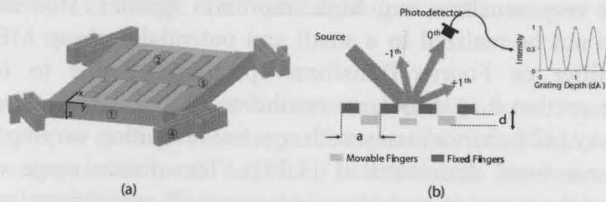

Fig. 3-17. MEMS Lamellar Grating Interferometer used in a Fourier transform spectrometer. Schematic of the variable groove depth diffraction grating (a) and operation principle of the device (b). From [3.37]

The resolution of the LGI spectrometer is limited by the maximum deflection of the movable grating grooves according to Eq. (3.11). Theoretical evaluations demonstrate that structures allowing grooves deflection of 300 μm are possible [3.36] which means resolution R=1000 at the wavelength of 600 nm. However practical MEMS realizations of the LGI based spectrometers report on the 5.5 nm resolution at the wavelength of 800 nm [3.36] and resolution of 12 nm at the wavelength of 638 nm [3.37].

3.6 Why using a diffraction grating?

The important decision to be made at the initial phase of the research is the selection of the concept with the best prospects for further development and actual realisation of microspectrometer. According to the project goals outlined in the introduction, the requirements for the spectrometer are as follows:

1. High spectral resolution (better than 1 nm) and operating bandwidth suitable for a wide range of applications (several hundreds of nanometers).
2. High sensitivity, which implies a high etendue - resolving power product.
3. Small size (the order is 1 cm or smaller).
4. Potentially low cost per device in a high-volume production.

The first and second requirements would be difficult to satisfy using a prism based dispersing element, since the etendue-resolving power of a prism is intrinsically smaller than that of other dispersing elements as discussed in section 3.1 and section 3.2.

Large and expensive Fabry-Perot or Fourier-Transform spectrometers are considered as very sensitive and high resolution devices. However, the high resolution can not be realized in a small and potentially cheap MEMS tunable Fabry-Perot filter or Fourier-Transform spectrometer due to technological problems (see section 3.5). Moderate resolution can be achieved with a Fabry-Perot filter array (128 channel array with spectral resolution varying from 1.7 nm to 3.8 nm have been demonstrated [3.38]). The disadvantage of the array approach is that the signal in each channel is inversely proportional to the number of channels which limits the spectrometer operating range and annihilates the Jacquinot advantage of a FP etalon.

Grating based free-space or waveguide spectrometers can provide a reasonably good resolution meeting the first requirement. Requirements three and four can also be satisfied. However, an acceptable etendue is a problem in the case of the waveguide spectrometers. Reasonable spectral resolution can be achieved in a waveguide spectrometer only if the waveguide operates in a single-mode regime. This, in turn, results in a very thin guiding layer (for example, 160 nm for the device described in [3.20]) and problems in coupling light into the waveguide from a free space.

In the case of photonic crystal demultiplexers the etendue problem becomes even more severe due to the difficulties in coupling light from a homogeneous waveguide region into the modulated region (photonic crystal region). The requirement for a linear polarization of light implies additional 50% light intensity reduction. Moreover, efficient photonic crystal structures can be realized only with a high modulation contrast of the optical properties of the medium. This is difficult to achieve in the visible region where the lowest refractive index is 1 (air) and the highest is about 1.8. High-resolution lithography required for the patterning photonic crystal structures is a very expensive process. The aim for low cost in a high volume production can also be an issue, because of the fabrication of the relatively large-area photonic crystal devices (which is the case with the demultiplexers). Finally, a spectrometer based on a PhC would have a very limited operating spectral range, since superprism, superlens and negative refraction effects are valid in a small wavelength region (several tens of nanometers).

The use of the diffraction grating in free-space microspectrometers is underestimated in the literature. There is no fundamental reasons why a grating-based spectrometer can not meet all four requirements listed in the beginning of

this section. The reasonable etendue-resolving power product can be achieved by an appropriate optical design. The optical design can also answer the fabrication cost issues.

Taking into account the advantages and drawbacks of various concepts described above, a grating based spectrometer had been selected as a basis framework concept in the work described in this thesis. The main challenge can be formulated as follows. High spectral resolving power can be achieved in a complicated optical system including aspherical elements, while only a simple system which uses preferably only planar surfaces can be fabricated at low cost in a MEMS-like process. Thus the goal of the work is to resolve this contradiction.

References

[3.1] John James. *Spectrograph design fundamentals*, Cambridge University Press, Cambridge, 2007

[3.2] D. Malacara, B. J, Thompson. *Handbook of Optical Engineering*, Marcel Dekker, New Yorkm, 2001

[3.3] H. W. Moos, R. C. Vitz, J. R. Barry, and J. L. Buckley, "Small LiF Prism Spectrometer for Space Applications," *Appl. Opt.* 9: 601-603, 1970

[3.4] J. R. Nielsen, F. W. Crawford, and D. C. Smith, "An Infra-Red Prism Spectrometer of High Resolving Power," *J. Opt. Soc. Am.* 37: 296-300, 1947

[3.5] T. K. McCubbin, Jr., R. P. Grosso, and J. D. Mangus, "A High-Resolution Grating-Prism Spectrometer for the Infrared," *Appl. Opt.* 1: 431-436, 1962)

[3.6] L. C. Hwang, M. Leutenegger, M. Gösch, T. Lasser, P. Rigler, W. Meier, and T. Wohland, "Prism-based multicolor fluorescence correlation spectrometer," *Opt. Lett.* 31: 1310-1312, 2006

[3.7] M. Czerny and A. F. Turner, "Uber den Astigmatismus bei Spiegelspektrometern," *Z. Phys.* 61: 792–797, 1930.

[3.8] O. V. Littrow, "Uber eine neue Einrichtung des Spectralapparats", *Wien Ber.* 47:26-32, 1863

[3.9] H. A. Rowland. On concave gratings for optical purposes. *Phil. Magazine*, 16(99):197-210, 1883

[3.10] E. G. Loewen, E. Popov, *Diffraction gratings and applications*, Marcel Dekker, New York, 1997

[3.11] R. K. Kostuk, J. W. Goodman, and L. Hesselink, "Design considerations for holographic optical interconnects," *Appl. Opt.* 26: 3947-3953, 1987

[3.12] M. Testorf and J. Jahns, "Imaging properties of planar-integrated micro-optics," *J. Opt. Soc. Am. A* 16: 1175-1183, 1999

[3.13] S. Ura, F. Okayama, K. Shiroshita, K. Nishio, T. Sasaki, H. Nishihara, T. Yotsuya, M. Okano, and K. Satoh, "Planar Reflection Grating Lens for Compact Spectroscopic Imaging System," *Appl. Opt.* 42: 175-180, 2003

[3.14] S. Ura, T. Sasaki, and H. Nishihara, "Combination of Grating Lenses for Color Splitting and Imaging," *Appl. Opt.* 40: 5819-5824, 2001

[3.15] G. T. Reed, A. P. Knights, *Silicon photonics: An introduction*, Wiley-VCH, Berlin, 2004

[3.16] K. Chaganti, I. Salakhutdinov, I. Avrutsky, G. Auner, and J. Mansfield, "Sub-micron grating fabrication on hafnium oxide thin-film waveguides with focused ion-beam milling," *Opt. Express* 14: 1505-1511, 2006.

[3.17] J. Mohr, B. Anderer, W. Ehrfeld, "Fabrication of a planar grating spectrograph by deep-etch lithography with synchrotron radiation", *Sens. and Act. A*, 25-27: 571-575, 1991

[3.18] H. W. Yen, H. R. Friedrich, R. J. Morrison, and G. L. Tangonan, "Planar Rowland spectrometer for fiber-optic wavelength demultiplexing", *Opt. Lett.* 6: 639-641, 1981

[3.19] D. Sandera,. J. Muller, "Selffocussing phase transmission grating for an integrated optical microspectrometer", *Sens. and Act. A*, 88: 1-9, 2001

[3.20] K. Chaganti, I. Salakhutdinov, I. Avrutsky and G. W. Auner, "A simple miniature optical spectrometer with a planar waveguide grating coupler in combination with a plano-convex lens," *Opt. Express*, 14: 4064-4072, 2006

[3.21] Avrutsky, K. Chaganti, I. Salakhutdinov and G. Auner, "Concept of a miniature optical spectrometer using integrated optical and micro-optical components," *Appl. Opt.* 45: 7811-7817, 2006

[3.22] S. G. Johnson and J. D. Joannopoulos, "Designing synthetic optical media: photonic crystals," *Acta Materialia* 51: 5823-5835, 2003.

[3.23] T. Baba and T. Matsumoto, "Resolution of photonic crystal superprism", *Appl. Phys. Lett.* 81: 2325-2327, 2002

[3.24] T. Matsumoto, S. Fujita, and T. Baba, "Wavelength demultiplexer consisting of Photonic crystal superprism and superlens," *Opt. Express* 13: 10768-10776, 2005

[3.25] B. Momeni, J. Huang, M. Soltani, M. Askari, S. Mohammadi, M. Rakhshandehroo, and A. Adibi, "Compact wavelength demultiplexing using focusing negative index photonic crystal superprisms," *Opt. Express* 14: 2413-2422, 2006

[3.26] D. Malacara, *Optical shop testing*, John Wiley and sons, New York, 1992.

[3.27] P. Jacquinot, The Luminosity of Spectrometers with Prisms, Gratings, or Fabry-Perot Etalons, *J. Opt. Soc. Am.* 44, 761-765 (1954)

[3.28] D. Walton, J. J. Vanderwal, and P. Zhao, "The Use of CCDs in Fabry-Perot Spectrometers," *Appl. Spectrosc.* 46: 373-375, 1992

[3.29] G. Hernandez, "A High Luminosity Spectrometer for Night Airglow Studies," *Appl. Opt.* 9: 1225-1227, 1970

[3.30] J. H. Jerman, D. J. Clift, S. R. Mallinson, “A miniature Fabry-Perot interferometer with a corrugated silicon diaphragm support”, *Sens. and Act. A*, 29: 151-158, 1991

[3.31] J. H. Correia, M. Bartek, R. F. Wolffenbuttel, “Bulk-micromachined tunable Fabry–Perot microinterferometer for the visible spectral range”, *Sens. and Act. A*, 76: 191-196, 1999

[3.32] J. H. Correia, G. de Graaf, M. Bartek and R. F. Wolffenbuttel, “A CMOS optical microspectrometer with light-to-frequency converter, bus interface and stray-light compensation”, *IEEE Trans. Instrum. Meas.* 50: 1530–1537, 2001

[3.33] R. Bell, *Introductory Fourier Transform Spectroscopy*, Academic Press, New York, 1972

[3.34] Omar Manzardo, Hans Peter Herzig, Cornel R. Marxer, and Nico F. de Rooij. Miniaturized time-scanning fourier transform spectrometer based on silicon technology. *Opt. Lett.* 24(23):1705-1707, 1999.

[3.35] John Strong and G. A. Vanasse. Lamellar grating far-infrared interferomer. *J. Opt. Soc. Am.* 50(2):113-118, 1960.

[3.36] Omar Manzardo, Roland Michaely, Felix Schadelin, Wilfried Noell, Thomas Overstolz, Nico de Rooij, and Hans Peter Herzig. Miniature lamellar grating interferometer based on silicon technology. *Opt. Lett.* 29(13):1437-1439, 2004.

[3.37] Caglar Ataman, Haman Urey, and Alexander Wolter. A fourier transform spectrometer using resonant vertical comb actuators. *J. Micromech. Micro-eng.* 16: 2517-2523, 2006.

[3.38] S. -W. Wang, C. Xia, X. Chen, W. Lu, M. Li, H. Wang, W. Zheng, and T. Zhang, "Concept of a high-resolution miniature spectrometer using an integrated filter array," *Opt. Lett.* 32: 632-634, 2007

4. Planar microspectrometers based on imaging gratings

As it was discussed in chapter 3, a high quality optical system typically includes spherical and (or) aspherical elements, while only planar structures can be fabricated at low cost in a MEMS-like process. Moreover, the low-cost requirements prompt for a simple, easy to assemble design. The compromise is inevitable. The possible solution is to use planar imaging diffraction gratings which combine dispersion and imaging functionality and can be fabricated with MEMS technologies.

Two approaches to the design of a spectrometer using only planar elements are described in this chapter. The first one is a microspectrometer based on a single grating. An analytical model has been developed and applied to explore the limits in the design of such a highly miniaturized device. This design tool has been validated providing the smallest possible dimensions while maintaining acceptable spectral resolution. Within the second approach, a possibility to improve the performance of the microspectrometer using a second grating was considered and a double-grating microspectrometer had been designed. A planar concept had been implemented in both single and double grating spectrometer designs. This concept assumes that all spectrometer elements are arranged on two parallel lithographically processed chips. As a result, most of the components are already aligned after processing and only two parts have to be assembled.

4.1 Planar imaging grating

A planar imaging grating is a structure consisting of grooves on a flat substrate. The grooves are not necessary equidistant, straight and parallel. As it is demonstrated below, the curvature and non-periodicity of the grooves are responsible for the imaging properties of the grating.

The imaging properties of the grating can be described on the basis of a geometrical approach [4.1]. Figure 4-1 presents the geometry of the planar diffraction grating which images point *A* into point *B*. Plane *Oyz* of the coordinate system *Oxyz* lies in the grating plane and the origin of the coordinate system coincides with the grating central point. Consider point *O* and a point *P(y,z)* somewhere in the grating plain. Then the optical path difference *F* between light rays passing from *A* to *B* via point *P* and via point *O* is:

$$F(\lambda, y, z) = APB - AOB + m\lambda N(y, z) \tag{4.1}$$

In Eq. (4.1) *N(y, z)* is the number of the grooves between points *O* and *P(y, z)*, *m* is a diffraction order and λ is a wavelength.

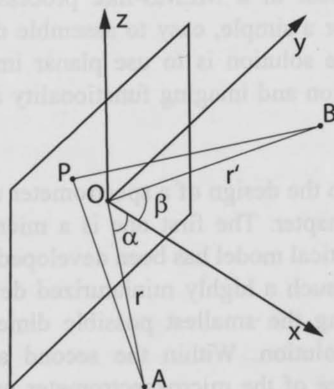

Fig. 4-1. Imaging geometry of a planar grating. Point A is imaged into point B.

The function in Eq. (4.1) can be decomposed into power series and take the form [4.2]:

$$F(\lambda, y, z) = \sum_{i=0}^{\infty} \sum_{j=0}^{\infty} F_{ij} x^i z^j = \sum_{i=0}^{\infty} \sum_{j=0}^{\infty} (M_{ij} + m\lambda N_{ij}) x^i z^j \quad \textbf{(4.2)}$$

A path difference F in Eq. (4.2) equal to zero corresponds to the aberration-free convergent wavefront. Thus, the coefficients F_{ij} define deviations of the wavefront proportional to $y^i z^j$ and can be considered as the aberration coefficients. The coefficients M_{ij} depend on the system configuration and the coefficients N_{ij} are determined by the grating groove pattern [4.2]. It is clear from the Eq. (4.2) that all the aberration coefficients can be made zero for a desired wavelength λ_0 by the proper selection of the coefficients N_{ij}, thus yielding an aberration-free image of a point A. Given the geometrical parameters of the system, the grating coefficients can be calculated analytically:

$$N_{ij} = -\frac{M_{ij}}{m\lambda_0} = \frac{1}{i!j!m\lambda_0}\left[\frac{\partial^{(i+j)}}{\partial y^i \partial z^j}(APB - AOB)\right]_{(0,\,0)} \quad \textbf{(4.3)}$$

Exact formulae which include calculated partial derivatives for the first 15 coefficients M_{ij} are listed for example in [4.2]. The grating groove pattern defined by the coefficients N_{ij} is a set of curved grooves not equally distributed in the grating plane. Such a structure resembles a part of the diffraction lens [4.3]. This analogy is illustrated in Fig. 4-2.

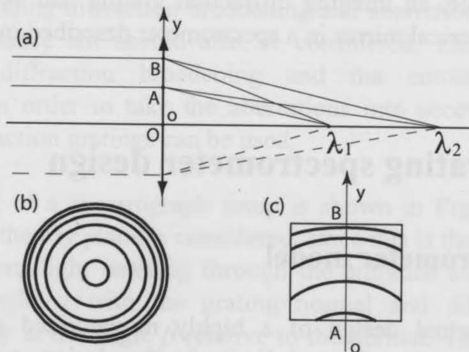

***Fig. 4-2.** Analogy between diffraction lens and imaging grating.*

Diffraction lens (Fig. 4-2(b)) focuses light in different points on the optical axis depending on the wavelength (Fig. 4-2(a)). The edge part of the diffraction lens schematically illustrated in Fig. 4-2(c) can be used for the spatial separation of the wavelength components of the incident light as shown in Fig. 4-2(a).

Imaging grating can not be characterized by a constant period, and the local period of such a grating along the *oy* axis is:

$$d = \left(\frac{\partial N}{\partial y}\right)^{-1} \tag{4.4}$$

The period d calculated in the central grating point is referred to as the grating period d_0.

The parameter λ_0 in Eq. (4.3) is the design wavelength. It follows from the Eq. (4.2) that the aberrations are no longer zero at wavelengths other then λ_0. For the fixed y and z the aberration coefficients are proportional to $\lambda_0 - \lambda$. That is why λ_0 is approximately the central wavelength of the spectrometer operating bandwidth.

The important conclusion that follows from the interpretation of the coefficients F_{ij} in Eq. (4.2) as aberration coefficients is that the imaging power of a diffraction grating can be used to compensate aberrations in a more complex optical system than a single-grating microspectrometer considered in the next section. For example, an imaging diffraction grating had been used to reduce aberrations of a spherical mirror in a spectrometer described in chapter 6.

4.2 Single grating spectrometer design

4.2.1 Spectrometer model

Before the actual design of a highly miniaturized spectrometer, it is important to explore the physical limits in the design, to find the optimal parameters and to determine possible compromises. This can be done with the help of an analytical model accounting for the effects which limit the

spectrometer performance.

4.2.1.1 Theoretical basis of the model

An analysis of the imaging properties of a single-wavelength optical system employing diffraction optical elements has been presented, for example, in [4.4] and [4.5]. However, the goals and parameters considered in the design of a single-wavelength system are different from the optimization targets and design parameters related to a miniaturized spectrometer. That is why the analysis and conclusions in [4.4] and [4.5] are not applicable directly to the design of a microspectrometer. The analysis described in [4.4] and [4.5] was modified and combined with the diffraction grating theory [4.1], [4.2] and then applied to the problem of the optimal design of a microspectrometer. As a result an analytical model of a spectrometer has been developed. It takes into account such factors as optical aberrations and diffraction effects, which do significantly influence the spectral resolution of a spectrometer when scaling down the characteristic dimension to the millimeter range. The model allows the estimation of the best achievable spectral resolution of a spectrometer at its main design parameters, minimizing the dimensions of the device.

The resolution of a spectrometer can be calculated as a product of the diffraction grating dispersion and the spot size produced by the imaging system when the entrance slit is illuminated with a monochromatic light (see discussion in section 2.3.5). Following the analysis of a single-wavelength imaging system in [4.4] and [4.5], the spot size can be estimated as a sum of different contributions including diffraction broadening and aberrations. The width of the image of the entrance slit should also be considered. The calculation of the dispersion, the diffraction broadening and the entrance slit image is straightforward. In order to take the aberrations into account the geometrical theory of the diffraction gratings can be used.

A schematic of a spectrograph setup is shown in Fig. 4-3. In the design optimization only the *oxy* plane is considered, since this is the dispersion plane of the grating. Incident light entering through the entrance slit is directed to the grating at the angle α with the grating normal and diffracts towards the photodetector array at the angle β relative to the normal. The parameters of the design are: the incident angle α, input aperture angle γ, distance r from the input slit to the grating surface, grating period d_0, position of the image sensor plane

(determined by the distance r' and angle ψ) and the design wavelength λ_0. The size of the illuminated part of the grating, $L = y_2 - y_1$, is defined by r, α and γ and can be calculated from the simple geometrical considerations, as shown in Fig. 4-3. At any set of design parameters the resolution of such a spectrometer can be determined considering the contributions of the relevant factors: optical aberrations, diffraction broadening of the image, influence of the slit width.

The contribution of aberrations can be calculated using a path difference function $F(\lambda,y,z)$ defined in Eq. (4.1). According to the discussion in section 2.2.1.2, the entrance slit image broadening due to aberrations is:

$$s_{aber} = \left.\frac{\partial F}{\partial y}\right|_{y=y_1} + \left.\frac{\partial F}{\partial y}\right|_{y=y_2} \tag{4.5}$$

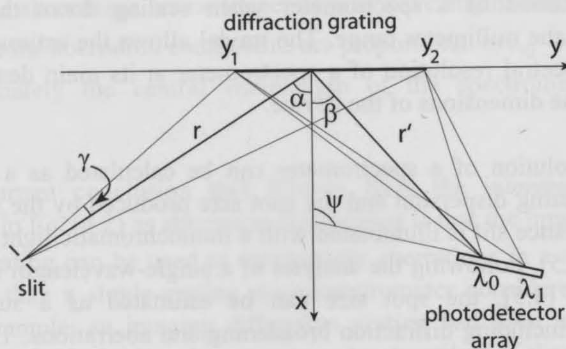

Fig. 4-3. *General configuration of a spectrometer based on a single imaging grating.*

For a finite number of the row members in Eq. (4.5) the value of s_{aberr} can be calculated analytically using Eqs. (4.2), (4.3) and (4.5). Note that the coefficients N_{ij} in Eq. (4.2) are calculated only once for the design wavelength, while the coefficients M_{ij} should be recalculated for another value of the wavelength taking into account that values of β and r' change with the wavelength.

The spatially finite size of the illuminated part of the grating leads to the diffraction broadening of the image of a point source. Such a broadening can be

estimated as follows:

$$s_{dif} = \frac{2\lambda}{(y_2 - y_1)\cos(\beta)} \tag{4.6}$$

The width of the entrance slit also influences the spectral resolution since the smaller the entrance slit the smaller its image on a photodetector. However there is an optimal slit width s_0 defined by the input aperture and reducing the entrance slit further would not improve the resolution. The angular width of the entrance slit image is:

$$s_{slit} = \frac{\cos(\alpha)}{\cos(\beta)} \times \frac{s_0}{r}$$
$$s_0 = \frac{\lambda}{\gamma} \tag{4.7}$$

The resolution of the spectrometer $\delta\lambda$ can be found as the product of the angular dispersion f and the sum of different contributions given by the Eq. (4.5), Eq. (4.6) and Eq. (4.7):

$$\delta\lambda = \delta\lambda(\lambda, \lambda_0, \alpha, r, \beta, r', \gamma, \psi) = f \times (s_{slit} + s_{dif} + s_{aber}) \tag{4.8}$$

The angular dispersion of the grating is defined by:

$$f = d_0 \times \cos(\beta) \tag{4.9}$$

Equations (4.2) - (4.9) are the basis of the model describing the dependence of the spectrometer resolution on different parameters. These equations (except for Eq. (4.6)) result from a geometrical optics approach and provide an estimate of the resolution based on the calculation of the entrance slit image width, multiplied by the dispersion. However, as it is discussed in section 2.2.1.3, geometrical optics cannot provide precise values of the resolution, since a diffraction analysis should be used that takes into account the phase and interference of the light. An accurate resolution estimate can be obtained via calculation of the point spread function (PSF) of the imaging system, convoluted with the ideal image of the entrance slit. The width of this curve measured at half maximum level (FWHM) and multiplied by the dispersion gives an accurate value for the resolution. For a spectrometer with optical aberrations that are small compared to the diffraction-limited performance of the system, the estimation of

resolution based on geometrical optics would give an overestimated value as compared to the diffraction analysis. Equation (4.8) was included in the model to compensate for such a discrepancy. In the case of a system with relatively large optical aberrations, which is typically the case in a microspectrometer, the geometrical approach would provide an underestimated result. In this case the Eqs. (4.2) - (4.9) provide an estimate of the resolution defined as a full width of a monochromatic spectral line at zero level, which implies that the resolution of an actual spectrometer defined as the width of the monochromatic line at half maximum (FWHM) is higher than the one predicted by the model.

4.2.1.2 Analysis of the model

Some of the parameters in Eq. (4.8) should be set to values dictated by technological constraints or design targets. Hence, these are fixed in order to study the dependence of the resolution on the other parameters. Figure 4-4 shows the dependence of the resolution on the incident angle α and the input aperture angle γ within the operating bandwidth of 100 nm. The fixed parameters in Eq. (4.8) are due to design targets and are set at: $r = r' = 10$ mm and $\lambda_0 = 650$ nm and those due to technological constraints at: $d_0 = 2\,\mu$m and $\psi = \pi/2$.

The resolution of a single-grating spectrometer is not uniform within the spectrometer operating range. According to the discussion in section 4.1, the best spectral resolution can be expected at the wavelengths close to the design one (650 nm). The lowest resolution is observed at the edges of the operating range (at 600 nm and at 700 nm). The resolution at 600 nm is slightly (by about 0.4 - 0.6 nm) better than that at 700 nm. For the data points in Fig. 4-4 and Fig. 4-5 the worst values of the resolution (calculated for the wavelength of 700 nm) had been used.

From Fig. 4-4 it is evident that a small aperture angle and a large angle of incidence contribute to an improved resolution of the spectrometer. The improved spectral resolution with the reduced aperture angle complies with intuition, since aberrations of the grating are the main contribution to the resolution function in Eq. (4.8). However, the input aperture angle also defines the optical throughput of the spectrometer. The resulting signal reduction at the photodetector reduces the overall sensitivity of the device.

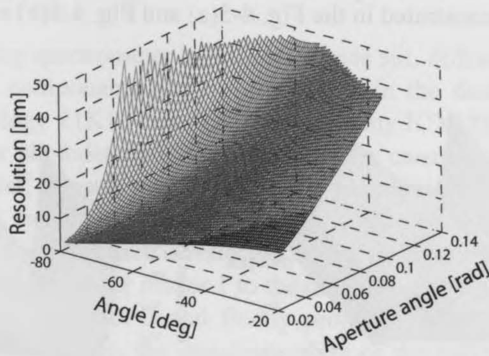

Fig. 4-4. *Dependence of spectral resolution on angle of incidence and input aperture angle.*

Since spectral resolution and throughput are not independent parameters it is necessary to fix the spectrometer input aperture angle to such a value that an acceptable signal-to-noise ratio results at the detector and to take the angle ψ as a variable. Also at this set of fixed parameters the dependence of the resolution within a specified wavelength range on the other design parameters such as the incidence angle α and the distance from the slit to the grating r can be investigated. Assume further that $r' = r$. Since r is the largest dimensional parameter in the design it is convenient to take it as a measure of the spectrometer size and in the following discussion r is referred to as the spectrometer size or dimension. The angle ψ between photodetector plane and the grating normal can be optimized to maximize resolution. It should be noted that the optimal value of the angle ψ does not depend on the spectrometer size. This statement is supported when considering the characteristics of a diffraction lens. The focal distance of such a lens is inversely proportional to wavelength. That is why the optimal value of ψ is defined by the angle of incidence and grating period. Since the angle at which light falls on the surface of a photodetector should not exceed some maximum value to avoid Fresnel reflection of a substantial part of radiation, this angle is limited in the model to 45 degrees. Using Fig. 4-3 yields: $\psi_{max} = 180 - 45 - \beta$.

Figure 4-5 shows the spectrometer resolution depending on the angle of incidence and on the spectrometer dimension. These dependencies had been calculated for the operating range of 100 nm and two different values of the

grating period (1 μm and 2 μm). Results for the aperture angle of 0.1 rad. and 0.05 rad. are demonstrated in the Fig. 4-5(a) and Fig. 4-5(b) respectively.

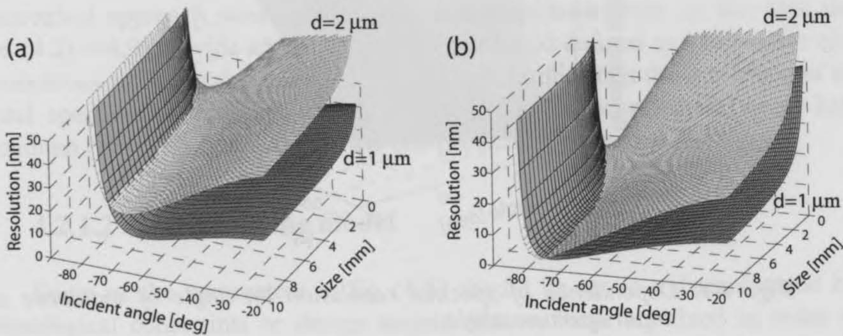

Fig. 4-5. *Dependence of the resolution within a 100 nm bandwidth on the angle of incidence and size (the distance from the entrance slit to the grating) of a spectrometer. The results are for the grating period 1 μm and 2 μm with input aperture angle 0.1 rad. (a) and input aperture angle 0.05 rad. (b).*

For each data point in the Fig. 4-5 the value of ψ was optimized. The optimal value gradually varies depending on the incidence angle from ~ 90° corresponding to the incidence angle of 20° to ~130° for incidence angle of 80°. As can be derived from Fig. 4-5, the resolution is weakly depending on the size of the spectrometer in case the size is larger then 5 - 4 mm. The best results are achieved at an angle of incidence in the 70° to 75° range, irrespective of spectrometer size. The strong dependence of the resolution on angle of incidence is due to aberrations of the grating, which is the main contribution in the resolution dependence. The width of the entrance slit image and the diffraction broadening start to affect resolution for a spectrometer dimension smaller than 2 - 3 mm. This dependence is inversely proportional to r, which is in agreement with Eq. (4.7). For the optimal width of the entrance slit, the influence of the slit image and the influence of the diffraction broadening on the resolution are of the same order of magnitude. Figure 4-5 predicts a resolution of a plane grating spectrometer with dimension as small as 6 mm of about 5 - 10 nm within a 100 nm operating range provided that the input aperture angle of the spectrometer is sufficiently small (~0.05 rad.). This result is the starting point in the design of a single grating microspectrometer.

4.2.2 Principal configuration of the spectrometer

A single-grating spectrometer includes entrance slit, diffraction grating and photosensor. These components had been arranged in the design as shown in Fig. 4-6. The Videology 21K137 camera with the Sony ICX278AL CCD sensor [4.6] was used as a photodetector. The spectrometer consists of two pieces of glass aligned parallel to each other and to the photosensor. All spectrometer optical components, including the input slit and the diffraction grating operate in reflection. The light from a source is reflected from a stripe mirror, acting as a slit and then redirected by the upper mirror 1 to the diffraction grating. The diffracted light is reflected by the mirror 2 and finally projected onto the photodetector through the glass plate. Hence, the imaging system of the spectrometer projects the dispersed image of the reflective input slit onto the plane of the image sensor. In this sense the operation of the reflective slit is similar to the conventional slit in a classical spectrometer. The described layout has the following advantages:

- The entrance slit and the grating are automatically aligned due to the photolithographic processing.
- The folded configuration provided by reflections from mirror 1 and mirror 2 reduces the dimensions of the spectrometer by two times as opposed to a non-folded design.
- Planar design significantly facilitates alignment.

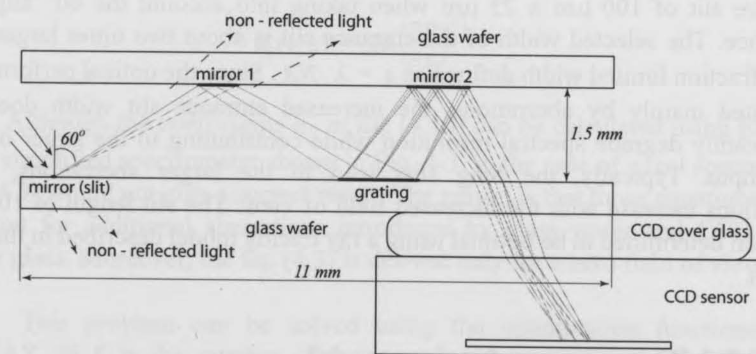

Fig. 4-6. Single grating spectrometer design.

As was already discussed in section 4.2.1.2, the value of the angle of incidence in the range of 70 - 75 degrees would give a superior spectral resolution

(Fig. 4-5), however the amount of light reflected from the glass surfaces increases with incident angle, due to Fresnel reflection. Such parasitic reflections contribute to the stray light, which is indeed observed in the fabricated device and is discussed in more detail in the next section. Therefore, the design was based on an angle of incidence at 60 degrees, as a compromise between stray light level and resolution.

The period of the grating d_0 (the local period in the grating center) should be minimized to achieve best resolution, as results from Fig. 4-5. For a lithographically fabricated grating the smallest period is constrained by the resolution of the available lithographic technology and is two times larger than the minimum feature size of the lithographic process. Taking into account that the local period varies along the grating and that the resolution of the available lithography was 0.7 μm, the parameter d_0 was chosen to be 2 μm.

The dimensions of mirror 1 define the input aperture of the spectrometer, since the non-reflected light escapes the system through the glass plate. The input aperture angle was selected at 0.05 rad. and the distance between the glass plates was 1.5 mm, which yields the very compact device. The angle $\psi = 90^o$ (see Fig. 4-3) is determined by the direct mounting of the image sensor in a planar structure.

The width of the slit mirror is 100 μm x 50 μm, which corresponds to the effective slit of 100 μm x 25 μm when taking into account the 60° angle of incidence. The selected width of the entrance slit is about two times larger than the diffraction limited width defined as $s = \lambda / NA$. Since the optical performance is limited mainly by aberrations, the increased entrance slit width does not significantly degrade spectral resolution while contributing to the larger optical throughput. Typically, the long slits lead to the larger aberrations, since aberrations increase with the increased field of view. The slit length of 100 μm had been determined to be optimal using a ray tracing model described in the next section.

4.2.3 Rigorous ray tracing model

The spectrometer design has been verified using rigorous ray tracing software ZEMAX [4.7]. The parameters of the spectrometer discussed in the

previous section had been used to define an optical model in ZEMAX including the positions of slit, mirrors, gratings, glass wafer and photosensor. The slit was modelled as a set of points in the object space defining the fields of the optical system with the coordinates *(0, 0)*, *(w/2, 0)*, *(- w/2, 0)*, *(w/2, l/2)*, *(w/2, - l/2)*, *(- w/2, l/2)*, *(- w/2, - l/2)*, where $w = 25\,\mu\text{m}$ and $l = 100\,\mu\text{m}$ are the width and the length of the slit respectively.

The packaging of the CCD sensor had been also taking into account in the model. This includes a cover glass 0.75 mm thick and a 1.94 mm distance from the top of the cover glass to the surface of the silicon CCD chip image area.

A diffraction grating can be represented in ZEMAX by a set of grating coefficients a_{ij}, which forms a function describing a phase added to the diffracted ray as:

$$P(y, z) = m\sum_{i,j} a_{ij}y^i z^j \quad \textbf{(4.10)}$$

In Eq. (4.10) *m* is the diffraction order and *y* and *z* are the coordinates in the grating plane. The direction of the diffracted ray can be found using the local grating periods for the *oy* and *oz* axis respectively:

$$d_y(y, z) = 2\pi\left(\frac{\partial P}{\partial y}\right)^{-1}$$
$$d_z(y, z) = 2\pi\left(\frac{\partial P}{\partial z}\right)^{-1} \quad \textbf{(4.11)}$$

Although the coefficients a_{ij} in Eq. (4.10) can be calculated using Eq. (4.3) for a simplified spectrometer shown in Fig. 4-3, in the case of a real spectrometer Eq. (4.3) would not give a correct result. The reason is that those equations do not account for additional aberrations introduced by glass wafer and CCD sensor cover glass. Moreover, the Eq. (4.3) is derived only for a zero field of view.

This problem can be solved using the optimization functionality of ZEMAX. If *K* is the number of the sum members in Eq. (4.10), the grating coefficients can be found as a solution of an optimization problem with *K* variables. The grating is symmetrical relative the *oy* axis which implies that all the members with *j* odd should be set to zero. This significantly reduces the number of optimization variables. As an optimization criteria a spot size

calculated vie geometrical ray tracing can be used [4.7]. Numerical experiments demonstrated that 10 coefficients are enough to adequately describe the grating and increasing the number of the coefficients further does not improve the system performance. Finally, the grating coefficients had been found which completed the design process.

Performance of the imaging system

Figure 4-7(a) shows a spot diagram of the designed single grating spectrometer. The relative illumination plot computed via ray tracing in ZEMAX is shown in Fig. 4-7(b) as a gray scale pattern. In the computation of the relative illumination surface the slit was represented as an extended rectangular light source, and Fig. 4-7(b) is a dispersed image of this source. The whole 100 nm bandwidth is projected on a 500 μm long area.

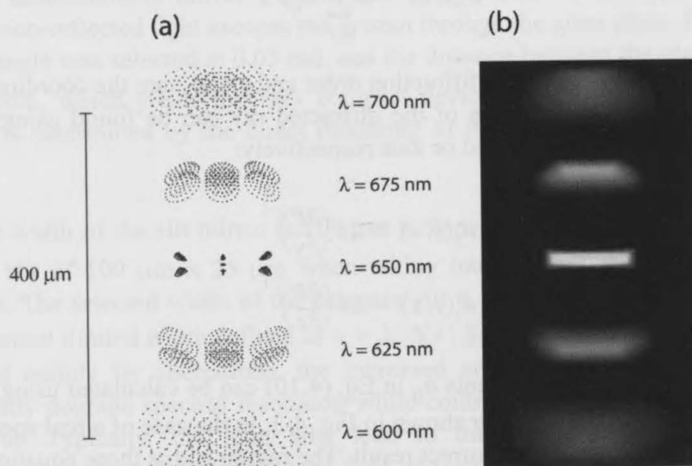

Fig. 4-7. *Spot diagram (a) of the designed single grating spectrometer and relative illumination plot (b).*

It is clear from Fig. 4-7, that the best imaging is obtained at the design wavelength of 650 nm, which is in the agreement with the theoretical discussion in the previous sections. The aberrations becomes larger and the image quality is degraded as the wavelength moves away from the design one. Various kinds of aberrations are present in the system, including defocus, spherical aberration,

coma and astigmatism. Table 1 presents Zernike aberration coefficients calculated for two fields (center and the edge of the slit) at different wavelength using ZEMAX.

TABLE 1. ***The main aberration coefficients of the single grating spectrometer***

λ [nm]	Field [μm,μm]	Defocus Z_4	Spherical Z_{11}	Coma Z_7	Coma Z_8	Astigmatism Z_5	Astigmatism Z_6
650	0, 0	-0.0045	$6x10^{-5}$	$5x10^{-4}$	0	0	-0.013
	50, 0	-0.006	-10^{-4}	-0.005	$-7.6x10^{-4}$	-0.097	-0.011
625	0, 0	-0.24	$-9x10^{-4}$	-0.017	0	0	0.012
	50, 0	-0.24	-0.0018	-0.021	$-8x10^{-4}$	-0.088	0.014
675	0, 0	0.238	0.001	0.017	0	0	-0.026
	50, 0	-0.025	$-2x10^{-5}$	0.011	$-7x10^{-4}$	-0.1	-0.024
600	0, 0	-0.47	-0.002	-0.034	0	0	0.05
	50, 0	-0.47	-0.0026	-0.039	-0.001	-0.078	0.052
700	0, 0	0.49	0.002	0.034	0	0	-0.028
	50, 0	0.48	$9x10^{-4}$	0.027	$-8x10^{-4}$	-0.11	-0.027

It follows from the Table 1 that the dominant aberration is defocus, coma and astigmatism. Relatively large defocus is the results of the planar design, and in principle can be compensated by the tilt of the image plane. The choice of the planar configuration is discussed in the previous sections.

Estimation of spectral resolution

Although Fig. 4-7 provides an insight into the imaging properties of the spectrometer, the resolution can be estimated precisely only if the diffraction effects are taken into account. The convolution of the PSF with the ideal (geometrical paraxial) image of the entrance slit can provide the real FWHM width of the slit image which can be used to calculate spectral resolution. The real entrance slit image can be computed in ZEMAX using diffraction image analysis feature, which performs inverse Fourier Transform of the OTF multiplied by the direct Fourier Transform of the ideal image.

If the slit image FWHM width S is known, the spectral resolution is computed as the product of S and linear dispersion D of the spectrometer in the image plane:

$$\Delta\lambda = S \times D \tag{4.12}$$

The wavelength dependence of the spectrometer resolution had been calculated using ZEMAX and analytical model described in section 4.2.1.1. The obtained results are presented in Fig. 4-8. The linear dispersion in the image plane is approximately constant and equal $D = 0.25$ nm/μm. The resolution values calculated via the computation of S using the relative illumination (geometrical ray tracing, without accounting for diffraction) and using the image diffraction analysis are represented in Fig. 4-8 by circles and crosses respectively. The values of spectral resolution calculated using relative illumination functionality in ZEMAX when S is measured at a zero intensity level rather than at half maximum are shown by triangles. Finally, solid and dashed lines in Fig. 4-8 represent resolution values obtained using analytical model as a full width and FWHM respectively.

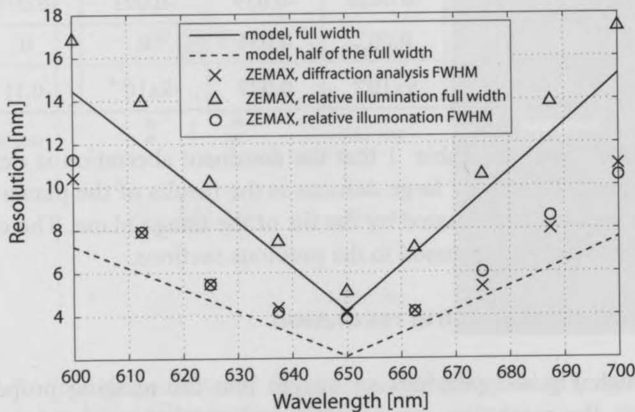

Fig. 4-8. *Resolution of the designed single grating spectrometer versus wavelength.*

The most accurate results are given by the diffraction image analysis. According to the simulations, the resolution is below 6 nm in the range of 60 nm and is below 11 nm in the range of 100 nm. In the range 640 nm - 660 nm the

aberrations are not large and the resolution (below 4.5 nm) is limited mainly by the slit width. The results obtained with the analytical model are in a qualitative agreement with the precise ray tracing model.

Tolerances

Any change of the spacing between the glass plates results in a mirrors (mirrors 1 and 2 in Fig. 4-6) displacement and thus in a change of the angle of incidence and the length of optical path that light travels from the slit to the grating. Such an error is the reason for the aberrations of the grating not to be minimized at the design wavelength, but rather at a wavelength spectrally shifted from the designed value. Thus, a misalignment within reasonable bounds results in a small shift of the operating bandwidth. Having limited such a shift to 25 nm, it was obtained that the alignment tolerances are approximately 100 μm for the spacing of the glass plates. According to ZEMAX image analysis, the resolution is decreased by less than 10% within the shifted operating bandwidth.

The tilt of one of the glass plates around the *oz* axis (see Fig. 4-3) also results in a spectral shift of the operating bandwidth. To keep this shift in the range of +/- 25 nm, the tilt should be less than +/- 0.4 degrees. The tilt around the oy axis disturbs the system symmetry and should not exceed +/- 0.5 degrees.

The lateral glass plates misalignment results in the decreasing of the spectrometer *NA* and is not very critical.

Stray light analysis

The fresnel reflections from the glass plates are the source of the stray light. This effect had been analysed in ZEMAX using a non-sequential mode [4.7].

Unlike a sequential mode in which the rays are traced sequentially, from the field points to surface 1, then 2, then 3, etc... in a strict sequence, in a non-sequential mode the rays are traced in the actual physical order they hit various surfaces and/or objects. The rays are randomly emitted from a source according to a defined statistical distribution. Each ray is traced accounting for the reflections at the optical surfaces. At every surface interface a ray is splitted into the transmitted and reflected rays, each of these rays has an energy assigned to it according to reflection and transmission coefficients. The detector is modelled as an array of pixels. The brightness of each pixel is proportional to the total energy

of rays that hit this pixel.

To perform the stray light analysis, the sequential spectrometer model which was used to design the device, had been converted to a non-sequential model. The slit was modelled as a mirror rectangle, and the circular ray-emitting surface represented an actual light source (for example, a tip of an optical fiber). The results of the simulation are presented in Fig. 4-9 (compare with Fig. 4-7(b)).

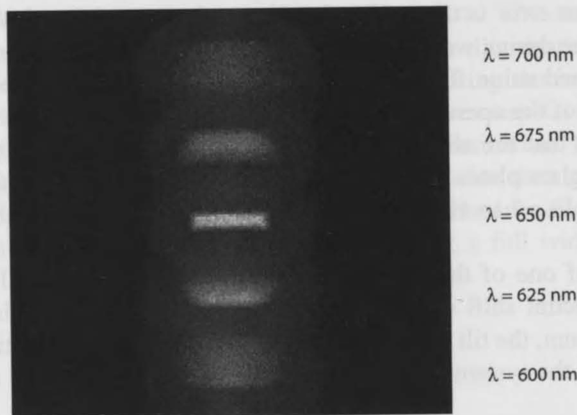

Fig. 4-9. Results of a non-sequential ray tracing. Single grating spectrometer model.

The Fresnel reflection from a glass surface at 60° angle of incidence is 9%. Thus, the pattern shown in Fig. 4-9 is actually a superposition of the dispersed images of the entrance slit and the elliptical images of the projection of a light source on a glass plate. The relative intensity of these elliptical images is about 10% of the slit images, which defines the level of the stray light. However, when the spectral lines are close to each other, the elliptical source images overlap and the resulting level of the stray light can be higher than 10%.

4.2.4 Grating efficiency

The lithographic fabrication allows only rectangular grating profile to be implemented. Although a rectangular profile (lamellar) grating provides a smaller diffraction efficiency than a blazed one, the parameters of the profile can be

optimized for maximum efficiency. The incidence angle, grating period and operating wavelengths are fixed by spectrometer design. The only parameter for optimization is the depth of the grating grooves. For the calculation of the grating efficiency a software PCGrate had been used [4.8]. The computed dependency of the grating efficiency on the depth of the grooves for the central wavelength of the spectrometer operating bandwidth (650 nm) is shown in Fig. 4-10.

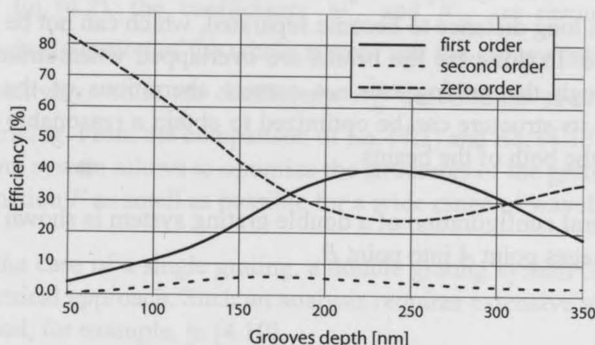

Fig. 4-10. Grating efficiency vs groove depth at the wavelength of 650 nm.

It can be seen in Fig. 4-10 that the maximum efficiency in the first diffraction order is about 40%. The optimal groove depth is 230 nm. This depth value allows for +/- 30 nm tolerances keeping the efficiency above 36%.

4.3 Double grating spectrometer design

4.3.1 Double grating imaging system

A single grating imaging system is limited in the sense that it does not give a sufficient freedom to a grating designer. The system parameters are fixed as soon as the design wavelength and geometrical layout are defined.

Suppose now that a second grating is added to the system. Suppose further that the system operates at two wavelengths, λ_1 and λ_2. The imaging and dispersion functionality of the first grating can be used to spatially separate light

beams at these wavelengths. Then these two light beams would hit the second grating at the different places. This implies that the nonlinear groove pattern of the second grating can be designed to introduce different aberrations in each of the light beams. Thus it would be possible to compensate the total wavefront aberrations in both of the beams. Such an approach had been implemented in [4.9] to design a three-wavelength color imaging system.

When the wavelength λ_1 and λ_2 become close to each other, the light beams have to travel a long distance to become separated, which can not be realized in a compact device. In this case the beams are overlapped when strike the second grating. Although the grating can not correct aberrations of the two beams independently, its structure can be optimized to obtain a reasonable reduction of aberrations of the both of the beams.

The general configuration of a double grating system is shown in Fig. 4-11. The system images point *A* into point *B*.

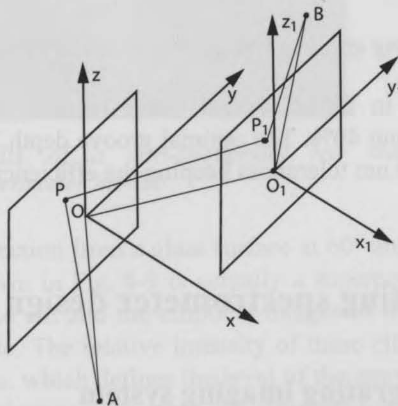

Fig. 4-11. *Imaging geometry of a double grating system. Point A is imaged into point B.*

Basically, there are two important advantages of using a double grating approach to design a spectrometer. The first one is the doubled dispersion which implies that spectral resolution can be improved by a factor of two as compared to a single grating system. The second advantage is the additional degrees of freedom in defining imaging properties of the system.

Similarly to a path difference function of a single grating system, the path difference function of a double grating one can be represented according to Eq. (4.13).

$$F(\lambda, y, z) = \sum_{i=0}^{\infty} \sum_{j=0}^{\infty} (M_{ij} + m\lambda N_{ij} + \tilde{m}\lambda \tilde{N}_{ij}) x^i z^j \quad \textbf{(4.13)}$$

As in Eq. (4.2), the coefficients M_{ij} and N_{ij} are responsible for the geometrical configuration of the whole system and the groove pattern of the first grating respectively, while the coefficients $\tilde{N}_{ij}$ describe the groove structure of the second grating. From the comparison of Eq. (4.2) and Eq. (4.13) follows that a double grating system allows to optimize the structures of the gratings in order to make the function F as small as possible for a wide range of wavelength.

As in the case of a single grating, a double grating system can be analysed using geometrical approach. Such an analysis requires extensive algebra and had been described, for example, in [4.10].

The most practical way to design a double grating system is to start from defining the principal layout based on the first-order equations (grating equation) and subsequently to find the grating coefficients via numerical optimization.

4.3.2 Principal configuration of the spectrometer

The principal design of a double grating spectrometer is shown in Fig. 4-12. All the spectrometer components are located on the two parallel glass plates mounted above the image sensor. The light from a source under test is reflected from a stripe mirror, acting as a slit, to the first grating. The first grating collimates and predisperces the light, which is after being reflected from the lower mirror is directed to the second grating. The second grating focuses the light on the plane of the image sensor adding its dispersive power to that of the first grating. As in the case with a single grating device, the Sony ICX278AL CCD sensor had been used as a photodetector.

The configuration of the spectrometer was driven by several factors. First, in order to simplify alignment, the gratings had been placed on the same glass plate. This forced to a folded geometry with an additional intermediate mirror

required to redirect light from the grating 1 to the grating 2. Second, the period of the gratings should be minimized to obtain a higher dispersion. However, this results in a higher diffraction angle, so that the light diffracted from the grating 2 hits again the intermediate mirror and does not reach the photodetector. To avoid such a situation, the input light incidence angle (see Fig. 4-12) should be increased. As in the case with the single grating spectrometer, Fresnel reflections limited the incidence angle which had been selected to be 60° degrees. Finally, the dimensional constraints lead to a 3 mm distance between glass plates. Thus, the grating periods had been set to 1.7 μm and 1.8 μm for the grating 1 and grating 2 respectively, which was above the limit of 1.6 μm imposed by the lithographic technology. The operating bandwidth was also limited by the position of the intermediate mirror, since longer wavelength diffract at higher angles. The resulting spectrometer bandwidth was 300 nm (from 450 nm to 750 nm).

The input aperture had been set at 0.05 and the size of the input mirror was 50 μm x 100 μm.

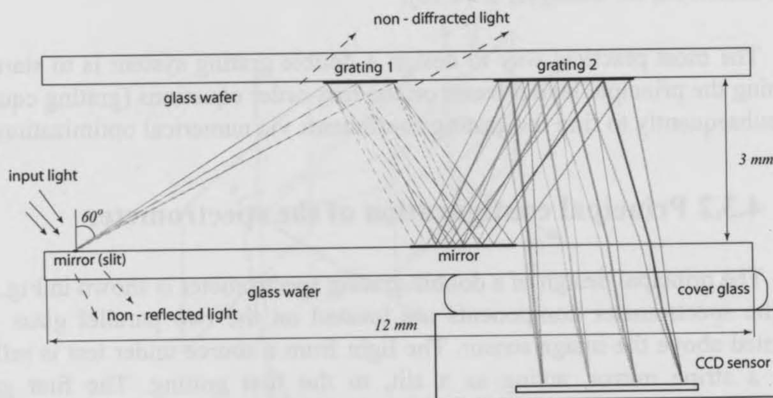

Fig. 4-12. *Design of a double grating spectrometer.*

4.3.3 Ray tracing model

For the final design and optimization of the grating coefficients and for the tolerance and stray light analysis a ray tracing ZEMAX model had been used. The simulation principles are described in section 4.2.3.

Each grating was defined in ZEMAX using 10 coefficients. Thus, the spectrometer design was a 20 variables optimization problem. In the beginning of the optimization process the grating 2 was linear with its coefficients fixed. The image plane was moved to infinity, and the coefficients of the first grating were optimized to obtain collimation of the light. At the next step, the image plane was returned at its place and both of the gratings were optimized to achieve the smallest possible image of the slit at the wavelengths from the spectrometer operating bandwidth.

Performance of the imaging system

The spot diagrams calculated at the wavelength of 450 nm, 550 nm, 650 nm and 750 nm are shown in Fig. 4-13(a). The spot diagram and illumination pattern when these four wavelength are projected on the image plane are shown in Fig. 4-13(b).

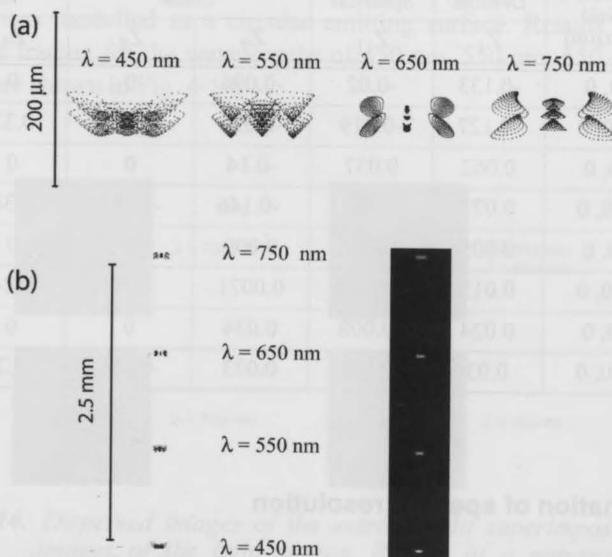

Fig. 4-13. *Spot diagram of the double grating spectrometer at different wavelength in a magnified scale (a) and spot diagram and illumination plot as projected on the photosensor (b).*

As it is visible in Fig. 4-13, the imaging system of two gratings compensates

aberrations at all wavelength in the spectrometer operating bandwidth. Although the relative contribution of various aberrations are different at different wavelength, the performance of the imaging system is reasonably uniform within the operating wavelength range.

Zernike aberration coefficients calculated in ZEMAX for the central and edge fields at the four wavelengths are listed in Table 2. Different aberration types are dominant at different wavelengths. For example, it follows from Table 2, that coma is the largest aberration at 550 nm. This is in agreement with the spot diagram at the wavelength of 550 nm shown in Fig. 4-13(a), which is a typical coma pattern.

TABLE 2. ***The main aberration coefficients of the double grating spectrometer***

λ [nm]	Field [μm,μm]	Defocus	Spherical	Coma		Astigmatism	
		Z_4	Z_{11}	Z_7	Z_8	Z_5	Z_6
450	0, 0	-0.133	-0.02	-0.096	0	0	-0.34
	50, 0	-0.127	-0.019	-0.094	-0.027	0.32	-0.32
550	0, 0	0.062	0.037	-0.14	0	0	0.063
	50, 0	0.077	0.037	-0.146	-0.056	0.38	-0.019
650	0, 0	0.005	0.0026	0.009	0	0	0.028
	50, 0	0.015	0.0029	0.0071	-0.03	0.24	0.032
750	0, 0	0.024	-0.008	0.034	0	0	0.056
	50, 0	0.03	-0.008	0.033	-0.017	0.2	0.062

Estimation of spectral resolution

The linear dispersion in the image plane of the designed spectrometer is $D = 0.116\,\text{nm}/\mu\text{m}$. According to the image diffraction analysis performed in ZEMAX, the FWHM width of the slit image varies from 19 μm to 21 μm depending on the wavelength which implies that spectral resolution is 2.2 nm - 2.5 nm.

Tolerances

The accurate alignment of the glass plates is essential to reach the characteristics of the designed spectrometer which had been predicted using simulations. The most critical tolerances are for the parallelism and for the distance between the glass plates, while the lateral misalignment results in the reduction of the input numerical aperture and is not very important.

The errors in the distance between the glass plates lead to the degradation of spectral resolution. Due to the misalignment of +/- 100 µm the resolution is degraded to 3 nm - 3.2 nm. The same decrease in spectral resolution results from the angular misalignment of +/- 0.5 degrees.

Stray light analysis

The sequential ray tracing model of the double grating spectrometer had been converted to a non-sequential mode in order to analyse the stray light. The light source was modelled as a circular emitting surface. Results of the non-sequential ray tracing for the wavelengths of 450 nm, 550 nm, 650 nm, 655 nm and 750 nm are shown in Fig. 4-14.

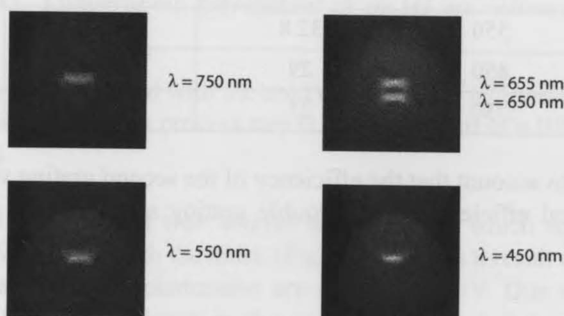

Fig. 4-14. *Dispersed images of the entrance slit superimposed with the images of the light source. Results of a non-sequential ray tracing.*

The bright rectangular images of the entrance slit are superimposed with less bright larger circular images of the light source. The relative brightness of these circular images is about 5% - 7% as compared to the intensity of the slit

image, which gives the level of the stray light in the system.

The dispersed images of the slit at the wavelengths of 655 nm and 650 nm are clearly separated. This is in agreement with the estimation of spectral resolution as 2.5 nm.

4.3.4 Efficiency of the gratings

The first grating works in the same conditions as the grating of the single-grating spectrometer, which efficiency is shown in Fig. 4-10.

The incidence angle for the second grating is different and varies with the different wavelengths. The values of the incident angle and corresponding computed grating efficiency at several wavelengths are presented in Table 3.

TABLE 3. ***Efficiency of the second grating***

λ [nm]	Incident angle [degrees]	Efficiency [%]
450	37	5
550	32.8	18
650	29	26
750	25	35

Taking into account that the efficiency of the second grating varies from 5% to 35%, the total efficiency of the double grating system varies from 1.2% to 10%.

4.4 Fabrication of the spectrometers

The design of the planar spectrometers is targeted to allow for the lithographic fabrication which is very suitable for high volume production at low cost per device. Lithographic fabrication is a mature technology widely used for production of optical microsystems [4.11], [4.12].

Fabrication process.

The optical components of the spectrometer (reflective mirrors and gratings on glass plates) have been implemented as aluminium microstructures on a glass wafer. The fabrication had been done at the Delft Institute of Microsystems and Nanoelectronics (DIMES) and the fabrication process is illustrated in Fig. 4-15.

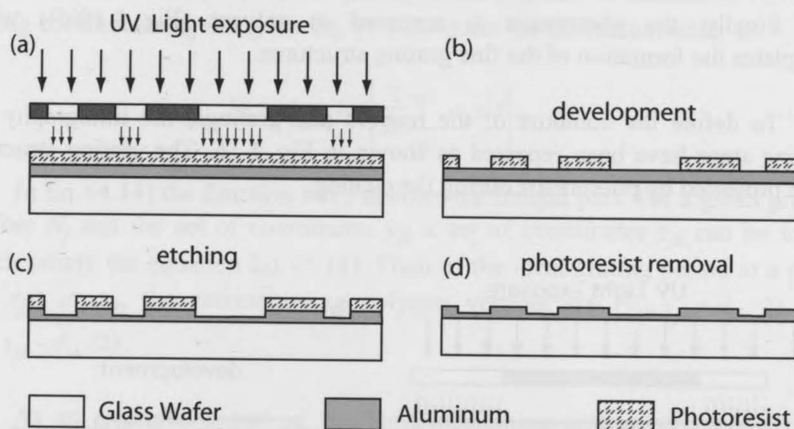

Fig. 4-15. *Lithographic fabrication of an Al microstructure on a glass wafer.*

The fabrication started with the cold deposition of 675 nm thick layer of Al on a AF45 glass wafer. This process step is a standard part of a BiPolar IC process run in DIMES.

Then Al was covered with a layer of photoresist which subsequently was exposed to UV light through the mask (Fig. 4-15(a)). As a result of using a mask, only desired areas of the photoresist are exposed to UV. Due to the structural changes that UV light induces in the exposed areas of the photoresists, it is possible to remove the photoresist from these areas using a liquid called developer, which simply dissolves and washes away the exposed photoresist (Fig. 4-15(b)).

The next step (Fig. 4-15(c)) is plasma etching using a Cl_2HBr plasma. Plasma atoms remove much more atoms of aluminium than molecules of the photoresist from the substrate because of chemical interaction. As a result, a

structure formed lithographically in photoresist is transferred into aluminium. The etching time is controlled to allow the desired depth of the Al trenches which was selected to be 230 nm to maximize grating efficiency as discussed in the previous sections. The rather small grating period could make it difficult to measure the etch depth of the grooves and to control the etching process. That is why a test structure consisting of lines of 10 µm width was included in the masks to facilitate etch depth measurements.

Finally, the photoresist is removed in solvent (Fig. 4-15(d)) which completes the formation of the fine grating structures.

To define the contours of the mirrors and gratings, the lithography and etching steps have been repeated as shown in Fig. 4-16. The grating structures were protected by photoresist during the etching.

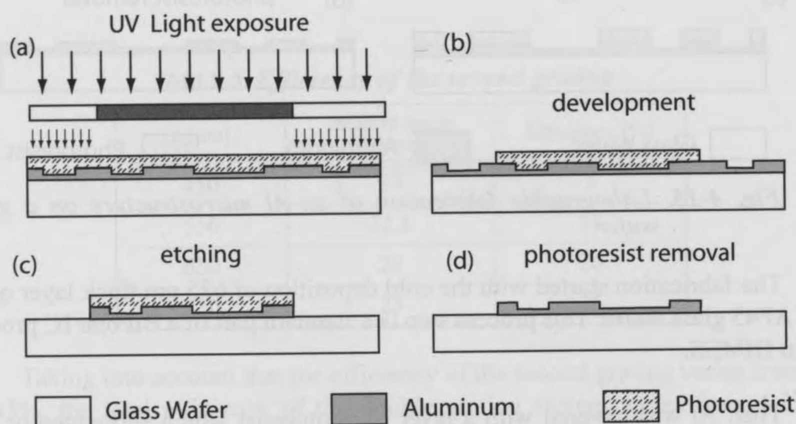

Fig. 4-16. *Defining the grating contour lithographically.*

Design of the lithography masks

In the beginning, masks are drawn in a layout editor of an IC design software (for example Cadence [4.13] or L-Edit [4.14]) using various geometrical primitives such as circles or polygons. For the fabrication two masks were required - according to the lithography steps described above.

The first mask contains the fine grating pattern. The shape of the grating grooves is more complex than graphical primitives and resembles a part of a circular curve. Thus, on the mask, each groove was replaced by a 200-vertices polygon. Such 200-vertices polygons approximated the geometry of the groove with the accuracy better than 5 nm. The coordinates of the polygon vertices were determined using the following procedure. An integer number *N* (positive as well as negative) can be assigned to each groove of the grating. This number *N* is a function of the coordinates in the grating plane and can be calculated from the grating coefficients a_{ij} using the Eq. (4.10), where the diffraction order $m = 1$:

$$N(y, z) = int\left[\frac{1}{2\pi}\sum_{ij} a_{ij}y^i z^j\right] \quad \textbf{(4.14)}$$

In Eq. (4.14) the function *int( )* denotes the integer part. For a given groove number N_j and the set of coordinates y_{jk} a set of coordinates z_{jk} can be found which satisfy the equation Eq. (4.14). Then, if the local grating period at a point (y_{jk}, z_{jk}) is d_{jk}, the corresponding polygon vertices are $(y_{jk}, z_{jk} + d_{jk}/2)$ and $(y_{jk}, z_{jk} - d_{jk}/2)$.

As an example, a part of the mask containing grating structure for the fabrication of a single grating spectrometer is shown in Fig. 4-17.

***Fig. 4-17.** Part of the lithography mask for the fabrication of a single grating spectrometer.*

The second mask contains the rectangle corresponding to the slit mirror and elliptical mirrors which were also approximated by polygons.

Processed wafer.

The AF45 glass wafer had been processed and diced resulting in a number of identical parts ready to be used to assemble a spectrometer. The photograph of the processed and diced wafer is shown in Fig. 4-18.

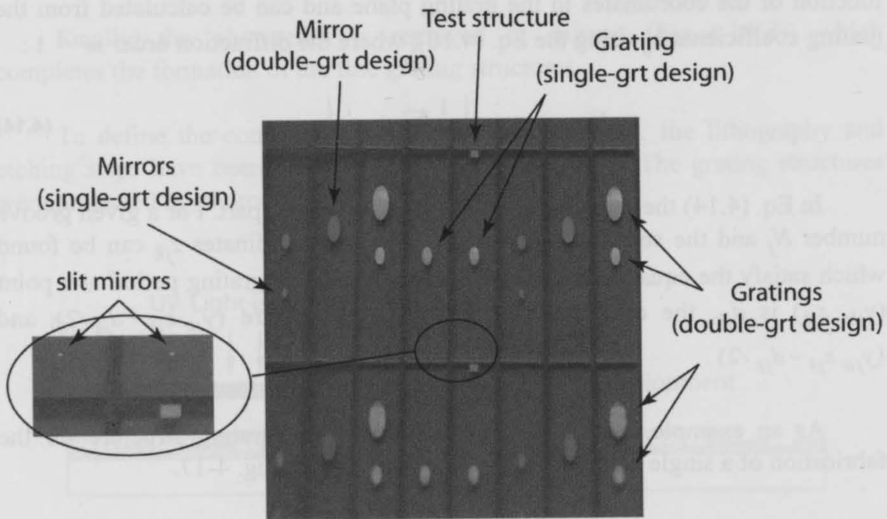

Fig. 4-18. *Processed wafer which contains spectrometer parts.*

The wafer contains parts of both single- and double-grating spectrometers. Elliptical grating and mirrors are clearly visible in the photograph, while the rectangular slit mirrors are too small and are shown in the insert in Fig. 4-18.

The gratings were studied more carefully using a Scanning Electron Microscope (SEM). The SEM photograph of the one of the gratings is shown in Fig. 4-19. The curved shape of the grating grooves can be easily recognized in this figure.

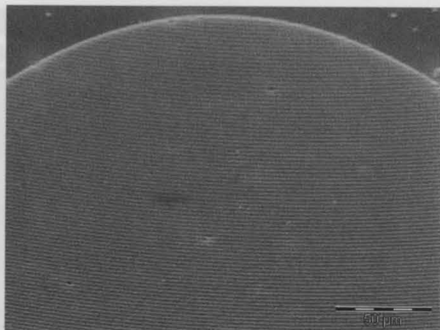

Fig. 4-19. *Scanning Electron Microscope (SEM) photo of the fabricated grating (single-grating design).*

A SEM photograph of the magnified part of the grating edge is shown in Fig. 4-20.

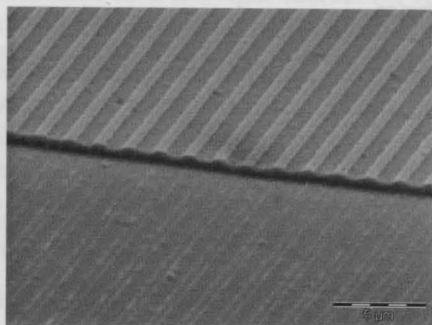

Fig. 4-20. *Scanning Electron Microscope (SEM) photo of the edge part of the grating.*

Figure 4-20 reveals that the shape of the grooves is not rectangular, which is due to the rather narrow width of the grooves. The groove width was close to the limit of the lithography resolution and thus the images of the lines on the photoresist, which determines the pattern to be etched, were blurred. This effect resulted in the rounding of the grooves edges during the etching process. Such rounded edges do not influence the imaging properties of the grating, however the diffraction efficiency can be changed.

Measurements of the grating efficiency were performed at a wavelength of 632 nm using a He-Ne laser and demonstrated an efficiency of 35% in the first diffraction order at a 60 degrees angle of incidence. According to simulations, the predicted efficiency at this wavelength is about 43%. Such a discrepancy is due to the fact that the simulated grating profile is lamellar, while the real shape of the grooves is not rectangular as mentioned above. The corrections had been applied to the grating profile in the simulations, which resulted in a 36% numerically calculated efficiency. This value is in agreement with the experimentally measured result.

4.5 Characterization of the fabricated devices

Both single- and double grating spectrometers had been assembled and characterized. The experimental setups were similar for both of the spectrometers and the only difference was the distance between the glass plates. As an example, Fig. 4-21 shows the experimental setup for the characterization of the double grating microspectrometer.

The lower glass plate was fixed just above the image sensor, while the upper glass plate was attached to an adjustable optical mount. A multi-mode optical fiber was used to feed the spectrometer. One of the cleaved fiber tips was exposed to a light source under test and the second fiber tip illuminated the input slit of the spectrometer. The USB interface of the Videology CCD camera was used to connect it to the computer and enable image capturing.

The spectrum can be reconstructed from the captured image. If a pixel row along the direction of the spectrometer dispersion is selected, there is a direct relationship between the pixel number in this row and the wavelength. Thus, the spectrum can be obtained as a dependency of the row pixel brightness on the pixel number, provided that a corresponding wavelength is assigned to each pixel number.

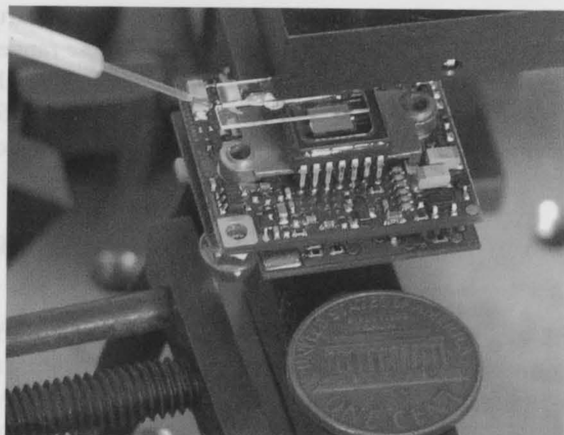

Fig. 4-21. Experimental setup for the characterization of the double grating microspectrometer.

A neon lamp was used as a test light source. Ne spectrum consists of a number of monochromatic lines corresponding to different atomic transitions [4.15]. That is why such a source is very convenient to characterize spectrometers.

Single grating spectrometer characterization

The typical spectral pattern captured with the single grating spectrometer when the entrance slit is illuminated with Ne light is shown in Fig. 4-22.

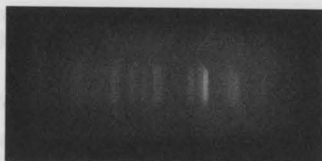

Fig. 4-22. Ne spectral pattern captured with the single grating spectrometer.

The most bright line in the Ne spectrum is the one at 703.2 nm. Using the adjustment of the spectrometer glass plates as discussed in section 4.2.3, the

operating bandwidth was shifted to move this line closer to its center. This line is visible in Fig. 4-22 as the brightest one. The corresponding spectrum is shown in Fig. 4-23. Judging from Fig. 4-23, spectral resolution in the range 650 nm - 700 nm is about 6 nm which is in the agreement with simulation results presented in Fig. 4-8. From the width of the line at 723.7 nm in Fig. 4-23 it follows that the resolution at the edge of the operating bandwidth is degraded to more than 10 nm.

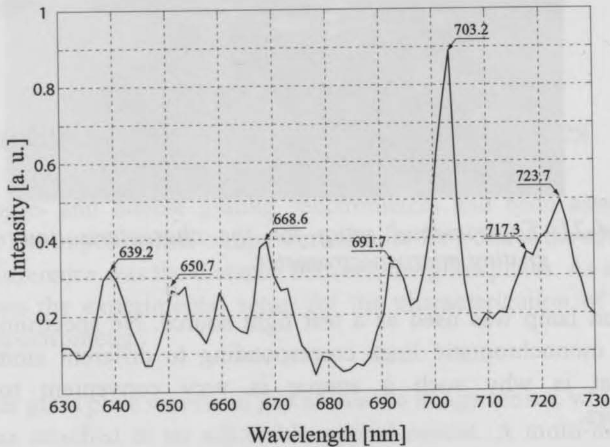

Fig. 4-23. *Ne spectrum measured with the single grating spectrometer.*

The stray light level is difficult to estimate from Fig. 4-23 since spectral lines are close to each other and the contributions of different lines overlap. However, the level of the stray light can be approximately estimated from the Fig. 4-23 using the step on the left from the line at 691.7 nm as $5/33 \approx 15$ %.

Double grating spectrometer characterization

The double grating spectrometer had been also tested with a Neon lamp source. The Ne spectral pattern captured with this spectrometer is shown in Fig. 4-24. When comparing Fig. 4-22 and Fig. 4-24 it is visible that the double grating spectrometer provides much better performance in terms of the resolution and operating bandwidth than the single grating one.

The graphic representation of the measured Ne spectrum in the range 550 nm - 750 nm is shown in Fig. 4-25. The major lines are marked to identify them

with real Ne lines.

***Fig. 4-24.** Ne spectral pattern captured with the double grating spectrometer.*

Judging from the width of a monochromatic line in Fig. 4-25, the resolution of the spectrometer is about 3nm, which is in agreement with the simulation results. The relative positions of the spectral lines can be determined with the accuracy of about 1 nm.

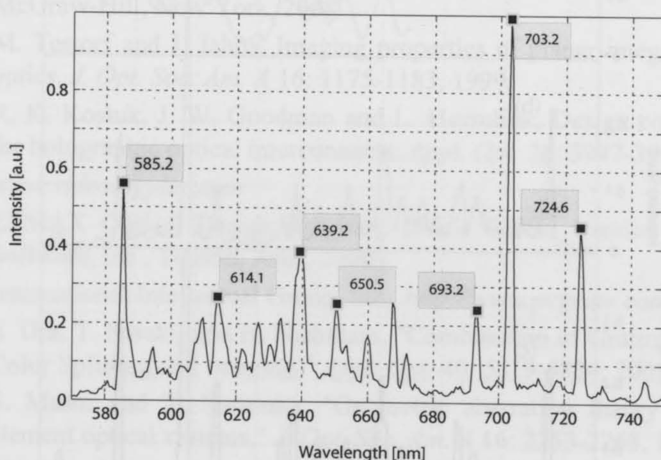

***Fig. 4-25.** Ne spectrum measured with the double grating spectrometer.*

The level of the stray light around clearly separated lines (such as the line at 703.2 nm) is about 5%, which is in agreement with simulations. However, stray light level increases as the lines get closer to each other, as in the region 600 nm - 680 nm in Fig. 4-25.

4.6 Conclusions

The development of a planar spectrometer concept is described in this chapter. The developed spectrometers are extremely compact, simple to assemble and potentially very cheap. However, the small input numerical aperture of the spectrometers limits the optical throughput and consequently the sensitivity of the devices. Thus, the planar spectrometers are most suitable for the applications in colorimetry and for the measurements of relatively bright sources such as lamps or LEDs. The double grating system provides superior performance than the single grating one in terms of spectral resolution and operating bandwidth.

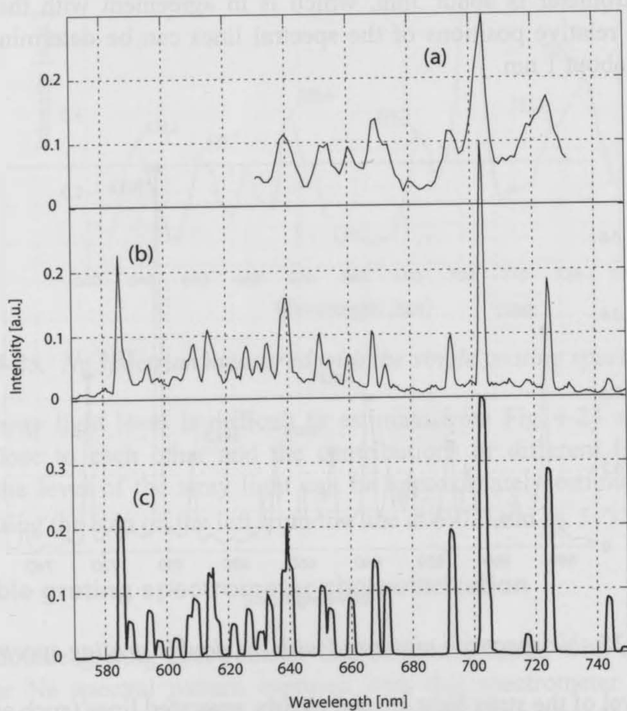

Fig. 4-26. *Ne spectrums measured using single-grating microspectrometer (a), double-grating microspectrometer (b) and commercial spectrometer (c).*

Figure 4-26 shows Ne spectrums measured with the fabricated planar

microspectrometers (single-grating - Fig. 4-26(a) and double-grating - Fig. 4-26(b)) in comparison with the spectrum measured using a commercial 2 nm spectral resolution AvaSpec 2048 spectrometer [4.16] (Fig. 4-26(c)). It is visible in Fig. 4-26, that Ne spectral lines which are not resolved by the 6 nm resolution single-grating spectrometer, are resolved by the 3 nm resolution double-grating spectrometer, and Ne lines, which are not resolved by the double-grating spectrometer, are resolved by the 2 nm AvaSpec spectrometer.

References

[4.1] H. Noda, T. Namioka and M. Seya, Geometric theory of the grating, *J. Opt. Soc. Am.* 64: 1031-1036, 1974

[4.2] C. Palmer and W. R. McKinney, Imaging theory of plane-symmetric varied line-space grating systems, *Opt. Eng.* 33: 820-829, 1994.

[4.3] R. E. Fischer, B. Tadic-Galeb, P. R. Yoder, *Optical System Design*, McGraw-Hill, New York, 2008

[4.4] M. Testorf and J. Jahns, Imaging properties of planar-integrated micro-optics, *J. Opt. Soc. Am. A* 16: 1175-1183, 1999.

[4.5] R. K. Kostuk, J. W. Goodman and L. Hesselink, Design considerations for holographic optical interconnects, *Appl. Opt.* 26: 3947-3953, 1987

[4.6] *www.videologyinc.com*

[4.7] ZEMAX Optical Design Program, User's Guide, Version 9.0 (Focus Software, Inc., Tucson, Ariz., 2000)

[4.8] International Intellectual Group, Inc., *http://www.pcgrate.com*

[4.9] S. Ura, T. Sasaki, and H. Nishihara, "Combination of Grating Lenses for Color Splitting and Imaging," *Appl. Opt.* 40: 5819-5824, 2001

[4.10] S. Masui and T. Namioka, "Geometric aberration theory of double-element optical systems," *J. Opt. Soc. Am. A* 16: 2253-2268, 1999

[4.11] H. Ukita, *Micromechanical photonics*, Springer-Verlag, Berlin, 2006

[4.12] H. P. Herzig, *Micro-Optics*, Taylor&Francis, London, 1997

[4.13] *http://www.cadence.com*

[4.14] *http://www.tanner.com*

[4.15] K. Burns, K. B. Adams, and J. Longwell, "Interference measurements in the spectra of neon and natural mercury," *J. Opt. Soc. Am.* 40: 339-344, 1950

[4.16] AvaSpec 2048 spectrometer datasheet, *http://www.avantes.com*

microspectrometers (single-grating - Fig. 4-26(a) and double-grating - Fig. 4-26(b)) in comparison with the spectrum measured using a commercial 2 nm spectral resolution AvaSpec 2048 spectrometer [4.16] (Fig. 4-26(c)). It is visible in Fig. 4-26 that Ne spectral lines which are not resolved by the 6 nm resolution single-grating spectrometer, are resolved by the 3 nm resolution double-grating spectrometer, and Ne lines, which are not resolved by the double-grating spectrometer, are resolved by the 2 nm AvaSpec spectrometer.

References

[4.1] H. Noda, T. Namioka and M. Seya, Geometric theory of the grating, *J. Opt. Soc. Am.* 64: 1031-1036, 1974

[4.2] C. Palmer and W. R. McKinney, Imaging theory of plane-symmetric varied line-space grating systems, *Opt. Eng.* 33: 820-829, 1994.

[4.3] R. E. Fischer, B. Tadic-Galeb, P. R. Yoder, *Optical System Design*, McGraw-Hill, New York, 2008

[4.4] M. Testorf and J. Jahns, Imaging properties of planar-integrated micro-optics, *J. Opt. Soc. Am. A* 16: 1175-1183, 1999.

[4.5] R. K. Kostuk, J. W. Goodman and L. Hesselink, Design considerations for holographic optical interconnects, *Appl. Opt.* 26: 3947-3953, 1987

[4.6] www.videologicinc.com

[4.7] ZEMAX Optical Design Program, User's Guide, Version 9.0 (Focus Software, Inc., Tucson, Ariz., 2000)

[4.8] International Intellectual Group, Inc., *http://www.pcgrate.com*

[4.9] S. Ura, T. Sasaki and H. Nishihara, "Combination of Grating Lenses for Color Splitting and Imaging," *Appl. Opt.* 40: 5819-5824, 2001

[4.10] S. Masui and T. Namioka, "Geometric aberration theory of double-element optical systems," *J. Opt. Soc. Am. A* 16: 2253-2268, 1999

[4.11] H. Ukita, *Micromechanical photonics*, Springer-Verlag, Berlin, 2006

[4.12] H. P. Herzig, *Micro-Optics*, Taylor and Francis, London, 1997

[4.13] *http://www.cedence.com*

[4.14] *http://www.instec.com*

[4.15] K. Burns, K. B. Adams, and J. Longwell, "Interference measurements in the spectra of neon and natural mercury," *J. Opt. Soc. Am.* 40: 339-344, 1950

[4.16] AvaSpec 2048 spectrometer datasheet, *http://www.avantes.com*

5. Lithographically fabricated concave diffraction gratings

Although planar diffraction gratings are able to provide both dispersion and imaging functionality as it was demonstrated in the previous chapter, the imaging performance of a planar system is significantly degraded by optical aberrations. The attempts to reduce aberrations result in a small optical throughput and, consequently, relatively low sensitivity of planar spectrometers.

As it is shown in this chapter, a non-planar surface of the grating gives more freedom to an optical designer in compensation of aberrations without sacrificing optical throughput. In an aberration-corrected non-planar grating the shape of the grooves and the spacing between them vary in a manner defined by the requirements of the imaging system [5.1].

Typically, non-planar gratings are fabricated by mechanical ruling [5.2] - [5.3] or holographic recording [5.4] - [5.7]. Mechanical ruling is a time-consuming process requiring fine mechanics and precise control of the ruling engine. Holographic recording uses a complicated optical setup to create an appropriate interference pattern on the grating blank.

There are technologies that uses laser [5.8], [5.9] or electron beam [5.10] to record grooves directly in a thin photoresist layer on the surface of a non-planar

grating substrate.The grooves are written one-by-one as in a mechanical ruling process, which implies that the mentioned technologies are also a long process requiring precise control of the writing beam.

In this chapter a different technology for the fabrication of concave gratings is described. The main advantage of this technology is the fabrication of the groove structure on a thin membrane using a standard planar lithography and subsequent membrane deformation into the desired shape. The planar lithography allows for the fast fabrication of any desired groove structure, since this is defined by the projected lithography mask. The fabrication technology described is a MEMS-like process with a single post processing step required to deform the membrane. This implies that the gratings in principle can be integrated with other MEMS structures and / or electronic circuits and fabricated in high volume at low cost per item.

5.1 Concave grating imaging.

A concave grating which images point A in to point B is shown in Fig. 5-1. In Fig. 5-1 the center of the coordinate system coincides with the grating central point *O*, axis *ox* is directed normally to the grating tangent surface and the axes *oy* and *oz* are tangent to the grating surface at the point *O*.

A formalism similar to that used for the analysis of planar gratings and described in the section 4.1 can be also applied to a concave grating [5.11]. Consider point *C* lying somewhere on the grating surface. Then the path difference between the light travelling from point *A* to the point *B* via point *O* and via point *C* is:

$$F(y, z, \lambda) = ACB - AOB + m\lambda N(y, z) \tag{5.1}$$

In Eq. (5.1) $N(y, z)$ is a function equal to the number of the grooves between the points *O* and $C(y, z)$, *m* is a diffraction order and λ is a wavelength. As in the Eq. (4.1), the functions $F(y,z,\lambda)$ and $N(y,z)$ can be decomposed into power series:

$$F(y, z, \lambda) = \sum_{i=0}^{\infty}\sum_{j=0}^{\infty} F_{ij}y^i z^j = \sum_{i=0}^{\infty}\sum_{j=0}^{\infty} (M_{ij} + m\lambda N_{ij})y^i z^j \tag{5.2}$$

The coefficients M_{ij} in Eq. (5.2) depend not only on the grating mounting geometry, as in the case of a planar grating, but also on the shape of the grating substrate.

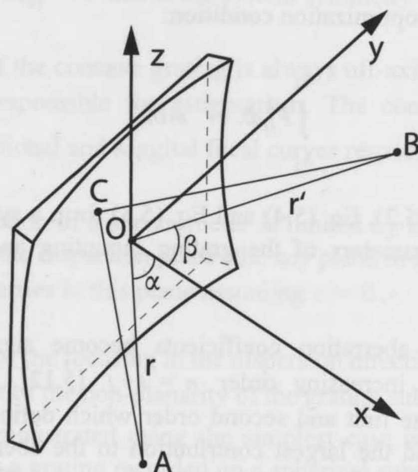

Fig. 5-1. Concave grating imaging point A into point B.

Suppose that the shape of the grating substrate is described by the function *f(y,z)*:

$$x = f(y, z) = \sum_{i=0}^{\infty} \sum_{j=0}^{\infty} a_{ij} y^i z^j \qquad \textbf{(5.3)}$$

Then the coefficients M_{ij} can be defined as follows:

$$M_{ij} = \frac{1}{i!j!}\left[\frac{\partial^{(i+j)}}{\partial y^i \partial z^j}(ACB - AOB)\right]_{(0,\,0)} = \varphi(\alpha, \beta, r, r', a_{ij}) \qquad \textbf{(5.4)}$$

As in the section 4.1, the coefficients F_{ij} in Eq. (5.2) can be interpreted as aberration ones. For the aberrations free image of a point A at a wavelength λ_0 all the coefficients F_{ij} in Eq. (5.2) must be made equal to zero.

In general, it is not possible to zero all aberration coefficients in a certain wavelength range. That is why the concave grating spectrometer design problem can be formulated as an optimization one: to find the optimal coefficients M_{ij} (which actually implies to find optimal grating mounting parameters r, r', α, β and grating substrate shape parameters a_{ij}) and grating groove pattern coefficients N_{ij}, which satisfy the optimization condition:

$$\int_{\lambda_1}^{\lambda_2} F_{ij}^2 d\lambda \to \min \tag{5.5}$$

Equations Eq. (5.2), Eq. (5.4) and Eq. (5.5) form a system which allows to find the optimal parameters of the grating mounting and the grating groove pattern.

Typically, the aberration coefficients become significantly smaller in amplitude with the increasing order $n = i+j$ [5.12]. The most important coefficients are of the first and second order which define the locations of the diffracted images and the largest contribution to the aberration-induced image broadening respectively. The exact formulae for the coefficients M_{ij} of the first and second order which can be derived from the Eq. (5.4) are as follows:

$$M_{10} = -(\sin(\alpha) + \sin(\beta)) \tag{5.6}$$

$$M_{01} = 0 \tag{5.7}$$

$$M_{20} = T(r, \alpha) + T(r', \beta) \tag{5.8}$$

$$M_{02} = S(r, \alpha) + S(r', \beta) \tag{5.9}$$

$$T(r, \alpha) = \cos(\alpha)\left(\frac{\cos(\alpha)}{2r} - a_{20}\right) \tag{5.10}$$

$$S(r, \alpha) = \frac{1}{2r} - a_{20}\cos(\alpha) \tag{5.11}$$

To make $F_{10} = 0$, one has to set $N_{10} = -M_{10}/(m\lambda_0)$, where λ_0 is the design wavelength. For the wavelength not equal to λ_0, the coefficient F_{10} can be

made zero by choosing another value of the angle β solving the equation $\sin(\alpha) + \sin(\beta) = m\lambda N_{10}$, which is actually the basic grating equation, since $N_{10} = 1/d$, where d is the grating period in its center.

The coefficient $M_{01} = 0$ due to the system symmetry relative the *oxy* plane.

The imaging of the concave grating is always off-axis, and the coefficients M_{20} and M_{02} are responsible for astigmatism. The conditions $F_{20} = 0$ and $F_{02} = 0$ define meridional and saggital focal curves respectively.

Since the resolution of a spectrometer is limited by the aberration-induced image broadening in the dispersion plane (the *xoy* plane in Fig. 5-1), consider the grating imaging properties in this plane assuming $z = 0$.

The condition for the focusing in the dispersion direction (meridional focus) is $F_{20} = 0$. The effect of the non-planarity of the grating substrate on the imaging properties can be demonstrated using the simplest case which is a "Rowland" grating [5.13]. This is a grating recorded on a spherical substrate. The grooves of such a grating form straight parallel lines when projected on a plane tangent to the grating surface in the grating central point. For this type of gratings $N_{10} = 1/d$, where d is the grating constant period and $N_{ij} = 0$ for $i > 1, j > 0$. For the spherical substrate $a_{20} = 1/(2R)$, where R is the radius of substrate curvature. Requiring $F_{20} = 0$, one can obtain the condition for the location of the source and the image points from Eq. (5.2) and Eq. (5.8):

$$r = R\cos(\alpha) \text{ and } r' = R\cos(\beta). \quad \textbf{(5.12)}$$

These conditions imply that if a point A is located on a circle tangent to the point O of a Rowland grating with a radius two times smaller than the radius of curvature of the grating substrate (Rowland circle), the diffracted images will also be located on this circle as shown in Fig. 5-2. At the same time, the coefficient M_{02} is not zero, which implies that the image of a point source obtained with a Rowland grating is a thin line. The thickness of this line image is defined by a higher order aberrations the most significant of which is coma.

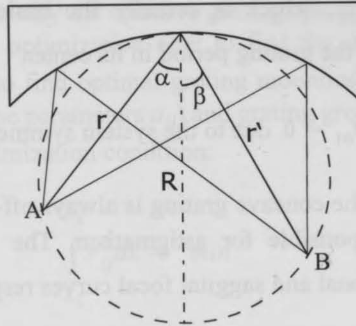

Fig. 5-2. Imaging geometry of a Rowland grating.

Obviously, for spectrometers with planar photodetectors the "Rowland" grating is not optimal. The grating should be designed to achieve a plane focal curve in the desired spectral region. A successful design implies a solution of Eq. (5.5), which can be solved by numerical methods, for example using an optical ray tracing software. The best solution usually is a grating with curved not equally separated grooves recorded on an aspherical substrate.

The spacing between the grooves and the grating substrate curvature in the plane *oxy* are responsible for the shape of the meridional focal curve, while the grating substrate curvature in the *oxz* plane and the curvature of the grooves are responsible for the saggital curve.

The standard technology used for the fabrication of such gratings is holography. After the Eq. (5.5) is solved, the positions of the recording sources should be reconstructed from the coefficients N_{ij}. However, in some cases this is not possible or a complicated optical setup is required to obtain the desired interfering wavefronts. In this sense a lithography, would it be applicable on the non-planar surfaces, could offer a significant advantage. The coefficients N_{ij} could be used to generate the grating pattern directly on the lithography mask.

5.2 Concave grating based spectrometer design

The technology proposed in this chapter is suitable for the fabrication of concave gratings to be used in compact spectrometers. This section describes several possible approaches to design a concave grating based spectrometer.

The parameters of the considered spherical concave gratings are as follows: radius of grating substrate curvature is $R = 25$ mm and the period in the grating center $d_0 = 4\,\mu\text{m}$. Although the smaller grating period is desired to obtain higher spectral resolution, the selected value of 4 μm was determined by the resolution of the lithography machine used in the experiments. The entrance numerical aperture of the systems described in this section is $NA = 0.2$.

The starting point in the considerations of the designs is a Rowland spectrometer shown in Fig. 5-3.

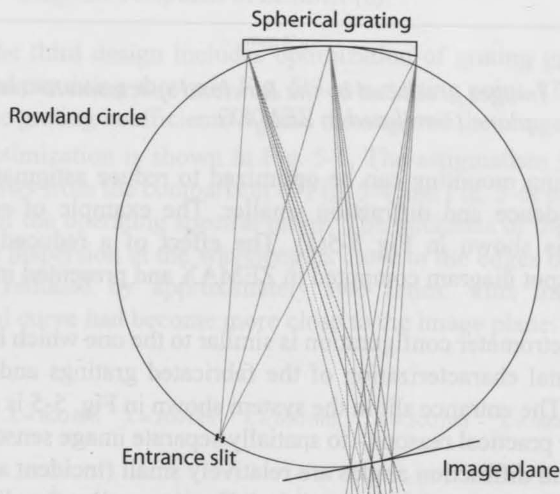

Fig. 5-3. *Rowland spectrometer.*

The wavelength operating region is from 400 nm to 800 nm. The entrance slit is located on the Rowland circle and the image plane is tangent to this circle in the point of location of the diffracted image at the wavelength of 600 nm (the center of the operating wavelength range).

The entrance slit is modeled as a single field point to demonstrate imaging properties of the design.

The resulting spectral pattern formed in the image plane as simulated in ZEMAX [5.14] is shown in Fig. 5-4. The images are thin lines as expected due to astigmatism.

It is also visible that the thickness of the line images is increased as the corresponding wavelength deviates from the center of the operating range. This is due to a circular focal curve of the Rowland spectrometer.

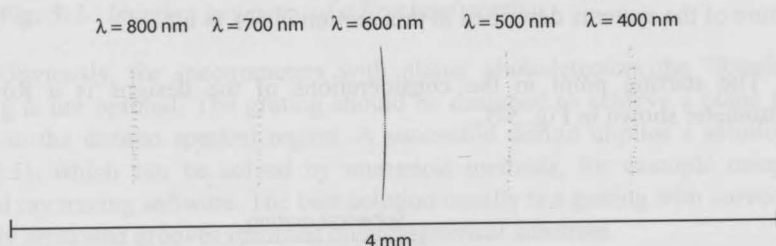

Fig. 5-4. *Images produced by the Rowland spectrometer on a planar image plane (simulated in ZEMAX).*

The grating mounting can be optimized to reduce astigmatism by making angles of incidence and diffraction smaller. The example of such a modified spectrometer is shown in Fig. 5-5(a). The effect of a reduced astigmatism is visible in the spot diagram computed in ZEMAX and presented in Fig. 5-5(b).

This spectrometer configuration is similar to the one which had been used in the experimental characterization of the fabricated gratings and is described in section 5.4.4. The entrance slit in the system shown in Fig. 5-5 is moved closer to the grating for practical reasons - to spatially separate image sensor and slit. Since the incident and diffraction angles are relatively small (incident angle is zero and diffraction angle is about 8 degrees), it is difficult to realize the slit at such a small distance to the image sensor due to the limits imposed by the sensor packaging dimensions and sensor read-out circuit board.

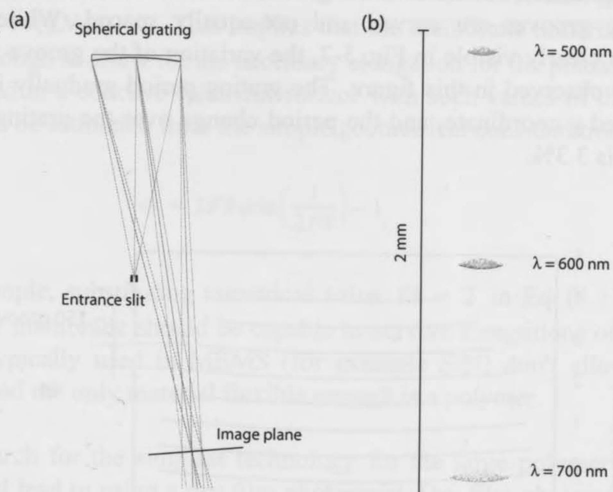

Fig. 5-5. Modified Rowland grating mounting (a) and corresponding spot diagram computed in ZEMAX (b).

Finally, the third design includes optimization of grating groove structure using a Rowland mounting shown in Fig. 5-3 as a starting point. The optimization variables are the grating coefficients N_{ij} and the angle of the image plane tilt. The result of the optimization is shown in Fig. 5-6. The astigmatism is substantially reduced as follows from the comparison of Fig. 5-4 and Fig. 5-6, especially in the central region of the operating spectral range. The thickness of the images in the direction of the dispersion at the wavelengths close to the edges of the operating range is also reduced by approximately two times. This implies that the meridional focal curve had become more close to the image plane.

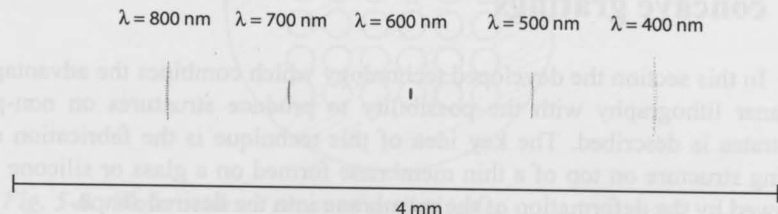

Fig. 5-6. Spot diagram of a spectrometer using a grating with the optimized groove structure.

The optimized structure of the grooves is shown schematically in Fig. 5-7. In fact, the grooves are curved and not-equally spaced. While the grooves curvature is clearly visible in Fig. 5-7, the variation of the groove spacing is too small to be observed in this figure. The grating period gradually increases with the increased *y* coordinate, and the period change over the grating is about 130 nm, which is 3.3%.

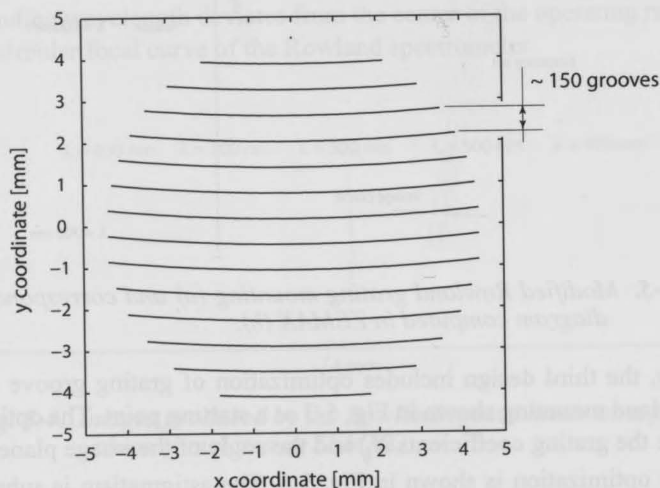

Fig. 5-7. Illustration of the optimized groove structure of the aberration-corrected grating.

5.3 Lithographic technology for the fabrication of concave gratings

In this section the developed technology which combines the advantages of a planar lithography with the possibility to produce structures on non-planar substrates is described. The key idea of this technique is the fabrication of the grating structure on top of a thin membrane formed on a glass or silicone wafer followed by the deformation of the membrane into the desired shape.

Typical values of the input numerical aperture (*NA*) of spectrometers vary

from 0.1 to 0.3, which defines also the $F\#$ number of the diffraction gratings used as $1.6 < (F\# = 1/(2NA)) < 5$. This implies that the membrane material should be stretchable enough to allow for the necessary elongation for the planar membrane to be deformed in a concave spherical surface with such values of the $F\#$. Such elongation can be estimated from the simple geometrical considerations as:

$$\sigma = 2F\#\,\mathrm{asin}\left(\frac{1}{2F\#}\right) - 1 \tag{5.13}$$

For example, substituting numerical value $F\# = 2$ in Eq. (5.13), one can obtain that the membrane should be capable to survive elongations of about 1%. Membranes typically used in MEMS (for example SiN) don't allow for such deformation and the only material flexible enough is a polymer.

The search for the simplest technology for the large polymer membrane fabrication had lead to using a dry film photoresist. Dry film photoresist is a UV light sensitive material which exists as a dry film. This makes it possible to obtain a photoresist layer on top of a wafer by a simple lamination.

The grating fabrication process starts with a glass or silicon wafer containing an array of etched or drilled (for example, ultrasonically) through holes at specified locations as shown in Fig. 5-8. For simplicity only one hole is considered in the following discussion.

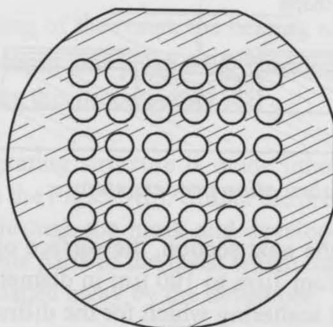

Fig. 5-8. *Wafer with an array of drilled holes.*

The first step is the lamination of the glass wafer with through holes with

the dry film resist as demonstrated in the Fig. 5-9(a). In the experiments a 30 μm thick OHKA TMMF negative film photoresist was used [5.15]. The resist film is rolled over the wafer which is heated up to 60 - 80 °C degrees. After the wafer is cooled it is exposed to UV light (350 nm wavelength) which changes chemical structure of the resist material increasing cross-linking between polymer molecules. After UV exposure the wafer is postbaked - heated up to about 150 °C for about 3 hours.

As a result of the lamination a 30 μm thick polymer membrane is formed on top of a circular hole.

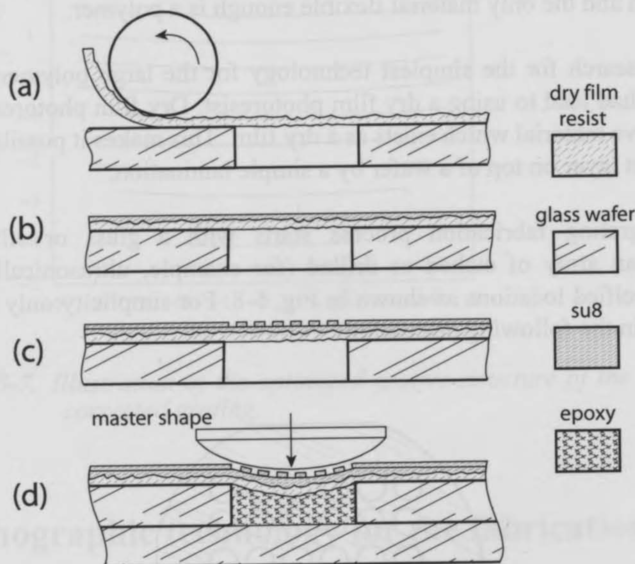

Fig. 5-9. *Grating fabrication process steps.*

As it is shown in the next section, the surface of the resist contains small scratches which can be from 1μm to 100 μm in diameter and 0.1 - 0.5 μm deep. Such defects lead to light scattering which for the diffraction gratings implies the presence of stray light or noise. In order to decrease the scattering effect of scratches a 3 μm thick layer of SU8 photoresist is spin-coated on top of the TMMF film resulting in a more smooth surface (Fig. 5-9(b)). Unlike the lamination process, the spin-coating deposition includes attachment of the wafer

to a special spin-coater plate, dropping a small portion of a liquid resist in the center of the wafer and subsequent rotation of the spin-coater plate at a speed of several thousands rates per minute. As a result, a thin film of the resist is formed on the wafer. The thickness of the resist film depends on its viscosity and on the spin-coater rotation speed. The SU8 2002 resist used in the experiments has relatively low viscosity and suitable for the deposition of the films several microns thick. The dependency of the resist film thickness on the rotation speed is shown in Fig. 5-10.

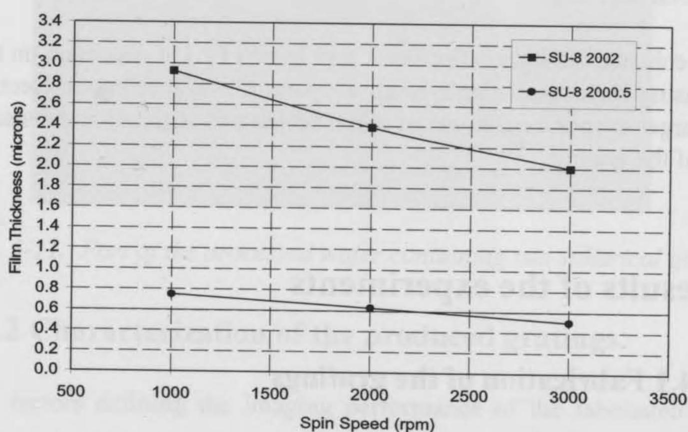

Fig. 5-10. *SU8 spin speed vs the thickness of the obtained layer [5.16].*

After the spin-coating of the resist, the heating of the wafer up to 95°C for about a minute, UV exposure and postbaking (heating up to 95 °C for another several minutes) completes this process step.

Subsequently, the grating structure is made lithographically in the second SU8 layer as presented in the Fig. 5-9(c). Unlike the previous step, the photoresist is exposed to UV light through the mask and developed before the postbaking. During the development the parts of the resist which had not been exposed to UV light are dissolved and washed away by the developer.

Finally, the cavity under the membrane is filled with the epoxy adhesive and the wafer is glued to another one. The membrane is deformed with the plano-convex lens used as a spherical template as illustrated in Fig. 5-9(d) and after

epoxy is cured the lens is removed. The maximum possible curvature of the grating is defined by the wafer thickness for a given hole diameter, since the sag of the grating surface can not be larger that the thickness of the wafer.

The deformation of the membranes can also result in the distortion of the grating pattern. Such an effect can be accounted for when the grating pattern is drawn on the lithography mask by introducing pre-corrections in the curvature and positions of the grooves. The effect of the distortion of the grating pattern on the imaging properties of the grating can be predicted using a ray tracing software as described in [5.17].

To enhance the light reflection a thin layer of Al is deposited on top of the grating using for example an e-beam evaporator. An accelerated electron beam hits Al target evaporating atoms of metal which subsequently condensate on the surface of the grating.

5.4 Results of the experiments

5.4.1 Fabrication of the gratings

The technology proposed in section 5.3 had been used for the experimental fabrication of the diffraction gratings. For this purpose a classical Rowland grating design had been selected. For the characterization of the gratings in a spectrometer setup, a mounting shown in Fig. 5-5 was used.

The polymer membranes had been fabricated on top of the ultrasonically drilled 7 mm diameter holes in a 0.525 mm thick Boroflorat glass wafer according to process steps shown in Fig. 5-9(a) and Fig. 5-9(b), as described in the previous section.

Subsequently, a 2 μm thick layer of SU8 had been spin-coated on top of the fabricated membranes and a lithography mask with the drawn grating patterns consisting of straight lines 2 μm thick and spaced with a 4 μm pitch was used for UV exposure of the resist. As a result, after the development and postbake procedures the planar grating structures with the spatial frequency of 250 line pairs/mm had been obtained.

Finally the membranes had been deformed as shown in Fig. 5-9(d) using a spherical lens with a 25.84 mm radius of curvature. The deposition of 100 nm reflective layer of Al completed the grating fabrication process.

The photograph of the fabricated gratings is presented in Fig. 5-11, which shows a part of the processed wafer containing two gratings 7 mm in diameter each.

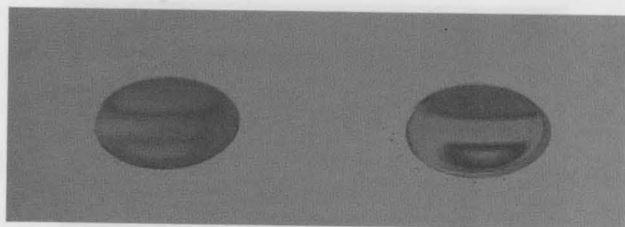

Fig. 5-11. *Part of the processed wafer containing two spherical gratings.*

5.4.2 Characterization of the produced gratings.

The factors defining the imaging performance of the fabricated gratings include:

- Positions of the grating grooves.
- Precision of the replication of the grating shape (how close is the shape of the grating surface to a spherical one).

Quality of the grating surface (roughness) defines the amount of scattered light, which influences the level of stray light in a spectrometer in which the grating is used.

The positions of the grating grooves are defined by the lithography mask. However, when the membrane is deformed in the last process step (Fig. 5-9(d)), the curvature and spacing between the grooves can slightly change. The elongation of the membrane in the experimentally fabricated gratings is about 0.3% as follows from the Eq. (5.13). The inverse analysis from [5.17] applied to the gratings demonstrated that such a degree of elongation has negligible effect on the imaging performance.

The surface of the gratings had been examined using Alfa-step 500 profilometer and Scanning Electron Microscope (SEM).

Since the large roughness of the dry film resist is considered as the main contribution to the roughness of the gratings, the characterization of the gratings starts with the consideration of the dry resist. SEM photograph of the dry photoresist surface is shown in Fig. 5-12.

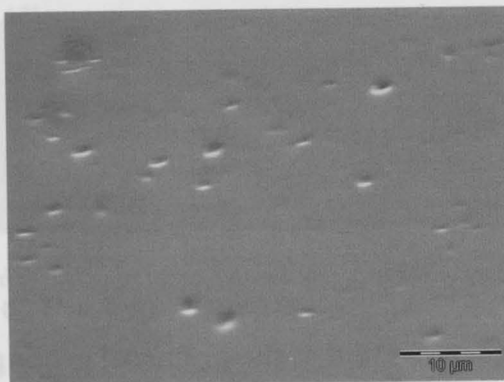

Fig. 5-12. *Scanning Electron Microscope (SEM) photograph of the dry film resist surface.*

While the SEM image gives a general qualitative picture of roughness, a more precise description is provided by surface profile measurements presented in Fig. 5-13. It is visible in this figure that a high spatial frequency roughness with a period of 2 μm - 10 μm as well as low frequency one with a period up to 50 μm - 100 μm contribute to the overall roughness of the resist surface.

The deposition of a thin (3 μm) layer of SU8 photoresist on top of the membranes as shown in Fig. 5-9(b) helps to improve the surface quality. The profile scan of the dry film resist surface after SU8 spin coating process step is presented in Fig. 5-14.

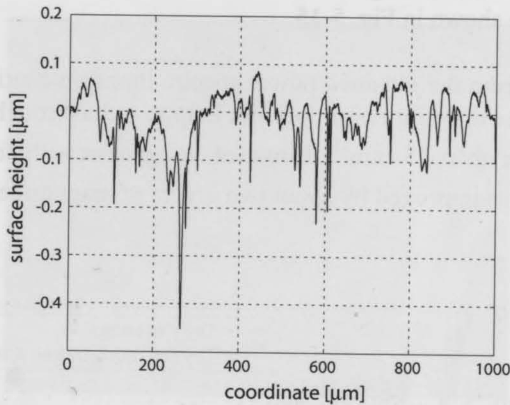

Fig. 5-13. Surface profile of the dry film resist measured with Alfa-step 500 profilometer.

It is clear from Fig. 5-14 that the spin-coated layer of SU8 significantly reduced high frequency roughness component, while the low frequency one remains unaffected.

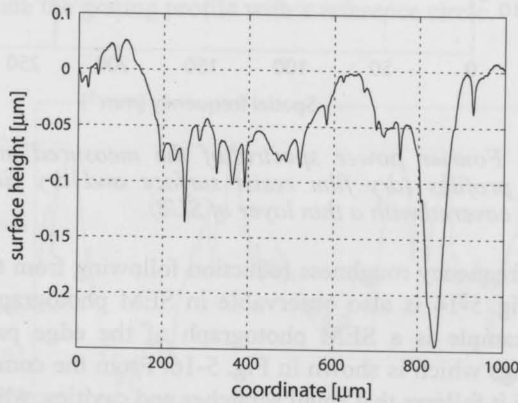

Fig. 5-14. Surface profile of the dry film resist covered with a 3 μm layer of SU8 (measured with Alfa-step 500 profilometer).

The roughness reduction can be estimated quantitatively using a Fourier Transform power spectrum of the measured profiles. The profile scan data

presented in Fig. 5-13 and Fig. 5-14 had been Fourier Transformed and resulting power spectra are shown in Fig. 5-15.

It follows from the obtained power spectra that spin-coating of a thin SU8 layer on top of the dry film resist does not help to reduce roughness with spatial frequencies lower than 15 mm^{-1}. However, roughness with frequencies higher than 100 mm^{-1} was improved by about two orders of magnitude.

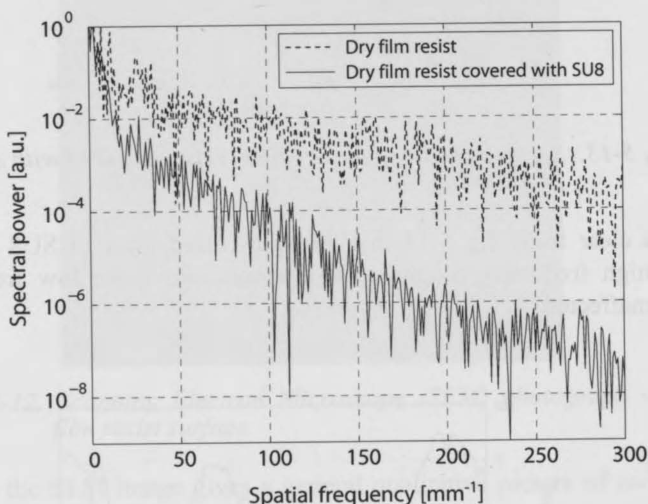

Fig. 5-15. *Fourier power spectra of the measured membrane surface profiles (dry film resist surface and dry film resist surface covered with a thin layer of SU8).*

The high frequency roughness reduction following from the comparison of Fig. 5-13 and Fig. 5-14 is also observable in SEM photographs of the grating surface. The example is a SEM photograph of the edge part of one of the fabricated gratings which is shown in Fig. 5-16. From the comparison of Fig. 5-12 and Fig. 5-16 it follows that small scratches and cavities, which present on the dry film resist surface, had been eliminated after the spin coating of a thin SU8 layer. However, low frequency defects still present.

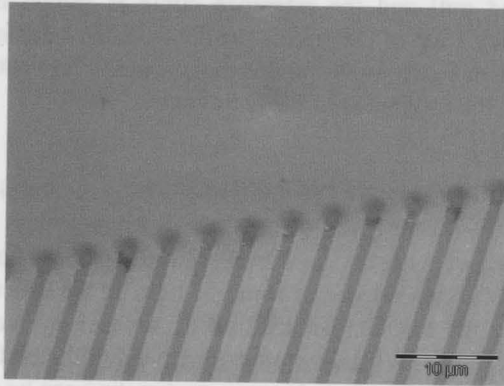

Fig. 5-16. Scanning Electron Microscope (SEM) photograph of the edge part of the fabricated grating.

To characterize the shape replication accuracy, the profile of the grating was measured using Alfa-step 500 profilometer. Original scan data contained a high frequency periodic component which is the result of the periodic grating grooves. This component was removed from the scan profile data using a lowpass numerical filter in Matlab. Then, the curve fitting optimization procedure was used to approximate the grating profile with a reference circle.

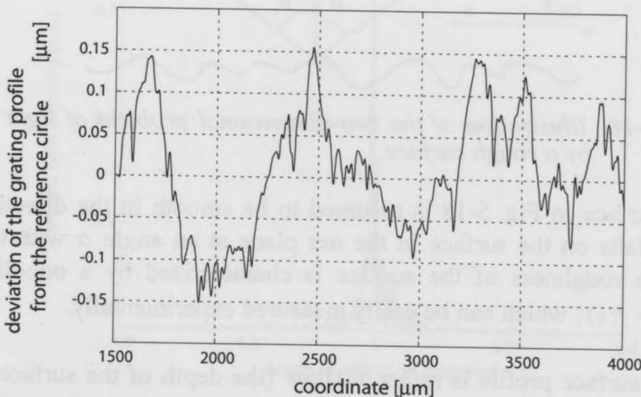

Fig. 5-17. Deviation of the grating profile from the reference circle.

The difference between the profile of the grating (with the high frequency component filtered out) and the reference circle is shown in Fig. 5-17. The amplitude of the deviation of the grating profile from the reference is comparable with the roughness in Fig. 5-14. It implies that the shape replication errors at least are nor larger than the roughness of the membrane.

5.4.3 Roughness induced scattering

The roughness of the reflecting surface defines the direction and intensity of scattered light. Such a dependence of scattered light on the structure of the surface is widely used for the fast characterization of surfaces by measuring scattered light distribution [5.18] - [5.20]. From the other hand, if the surface properties are known, the amount of light scattered in a given direction can be calculated [5.20].

Since one of the most common ways to characterize surface roughness is to measure surface profile along a straight line using a stylus profilometer, it is useful to consider the scattering problem in two dimensions as illustrated in Fig. 5-18.

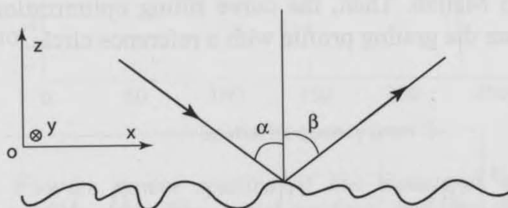

Fig. 5-18. *Illustration of the two-dimensional problem of light scattering by a rough surface.*

The surface in Fig. 5-18 is assumed to be smooth in the direction *oy* and light beam falls on the surface in the *oxz* plane at an angle α with the surface normal. The roughness of the surface is characterized by a one-dimensional function $z = f(x)$, which can be easily measured experimentally.

If the surface profile is rather shallow (the depth of the surface defects is much smaller than their width), which is often the case in practice, and surface is perfectly conductive, the diffraction theory of Kirchhoff can be applied to calculate the scattered electromagnetic field. The normalized field reflected in the

direction β is given by the following integral over the surface profile [5.20], [5.21]:

$$\rho(\beta) = \frac{F(\beta)}{2L}\int_{-L}^{L} \exp(i\boldsymbol{v}\cdot\boldsymbol{r})dx \quad \textbf{(5.14)}$$

In Eq. (5.14) $\boldsymbol{v}$ is the difference between the wave vectors of incident and reflected light, $\boldsymbol{r}$ is the vector describing surface profile and $F(\beta)$ is the phase function depending on the angle of reflection:

$$\begin{gathered}\boldsymbol{v} = \boldsymbol{k}_{inc} - \boldsymbol{k}(\beta)\\ v_x(\beta) = -(2\pi/\lambda)(\sin\alpha + \sin\beta)\\ v_z(\beta) = -(2\pi/\lambda)(\cos\alpha + \cos\beta)\\ \boldsymbol{v}\cdot\boldsymbol{r} = v_x x + v_z f(x)\\ F(\beta) = (1+\cos(\alpha-\beta))/(\cos(\alpha)\times(\cos(\alpha)+\cos(\beta)))\end{gathered} \quad \textbf{(5.15)}$$

Intensity of the scattered light can be obtained from the Eq. (5.14) as $I(\beta) = \rho(\beta)\times\rho^*(\beta)$, where ρ^* is a complex conjugate of ρ . An example of the profile of the dry film resist covered with a layer of SU8 is shown in Fig. 5-14.

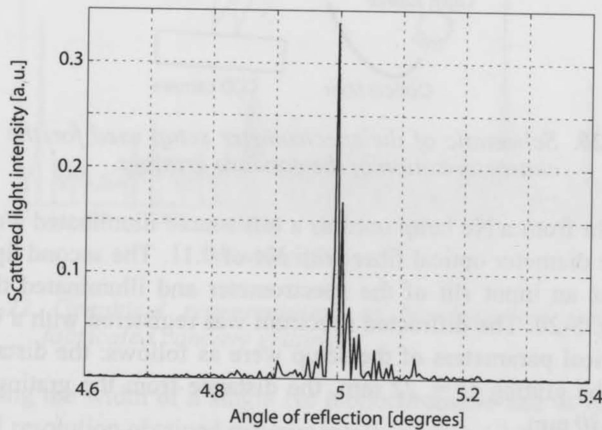

Fig. 5-19. *Calculated intensity of scattered light for the experimentally measured surface profile.*

Equation (5.15) can be applied directly to the experimental profile data measured with stylus profilometer to estimate the amount of scattered light. The result of such calculations is shown in Fig. 5-19. The integral in Eq. (5.14) was taken over 7 mm length (which equals to the diameter of the fabricated gratings), for light at the wavelength of 630 nm incident at a small angle (5 degrees).

Although a sharp reflectance peak in specular direction is present in Fig. 5-19, there is also a significant amount of scattered light in the range +/- 0.2 degrees around the specular direction.

5.4.4 Imaging performance of the gratings

The imaging properties of the fabricated gratings had been characterized in a spectrometer setup schematically represented in Fig. 5-20.

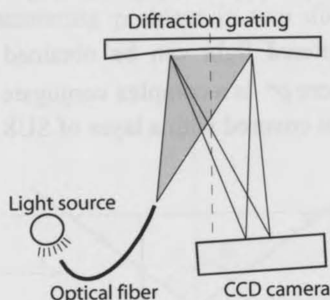

Fig. 5-20. *Schematic of the spectrometer setup used for the experimental characterization of the concave gratings.*

The light from a Ne lamp used as a test source illuminated a cleaved tip of an 5 μm core diameter optical fiber with *NA* of 0.11. The second tip of this fiber was acting as an input slit of the spectrometer and illuminated the grating as shown in Fig. 5-20. The diffracted spectrum was registered with a CCD camera. The geometrical parameters of the setup were as follows: the distance from the fiber tip to the grating $f1 = 22$ mm, the distance from the grating to the CCD camera $f2 = 30$ mm.

The resulting spectral pattern captured with the CCD camera is shown in Fig. 5-21. Two features can be observed in this figure. The first one is the

elliptical images of a circular fiber tip. This is due to grating astigmatism discussed in section 5.2. The elliptical shape of the images is in agreement with the spot diagrams computed with ZEMAX and presented in Fig. 5-5(b). The second feature is a stray light visible as a number of small dots around the more bright dispersed images of the fiber tip.

Fig. 5-21. *Spectral pattern of Ne light produced by the fabricated concave grating and captured with a CCD camera.*

Graphical representation of the measured spectrum is shown in Fig. 5-22.

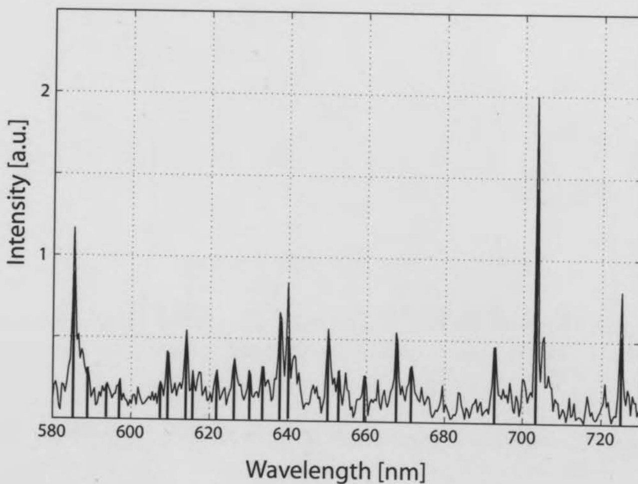

Fig. 5-22. *Graphical representation of Ne spectrum measured using fabricated concave gratings.*

Measuring the width of a single Ne monochromatic line at half maximum gives spectral resolution obtained experimentally as about 0.9 nm. The stray light observed in Fig. 5-21 as dots is visible in Fig. 5-22 as a number of fake or ghost spectral lines surrounding real spectral lines of Ne. The real Ne lines [5.22] are

marked in Fig. 5-22 with a vertical bold lines. Due to the ghost lines it is difficult to identify and measure weak spectral lines located near the strong ones.

The scattering effect in spectral measurements had been also simulated using Eq. (5.14) - Eq. (5.15). Since the grating period of 4 μm is smaller than the 12.5 μm radius of the stylus needle in the profilometer, it is not possible to measure the real grating profile precisely. That is why, to simulate grating scattering, the measured profile of the photoresist surface had been superimposed with an ideal grating profile and substituted into the integral of Eq. (5.14). The light incident angle was set to zero (as in the spectrometer shown in Fig. 5-5) and light spectrum was simulated as a collection of peaks of different amplitudes and different wavelengths corresponding to Ne spectral lines.

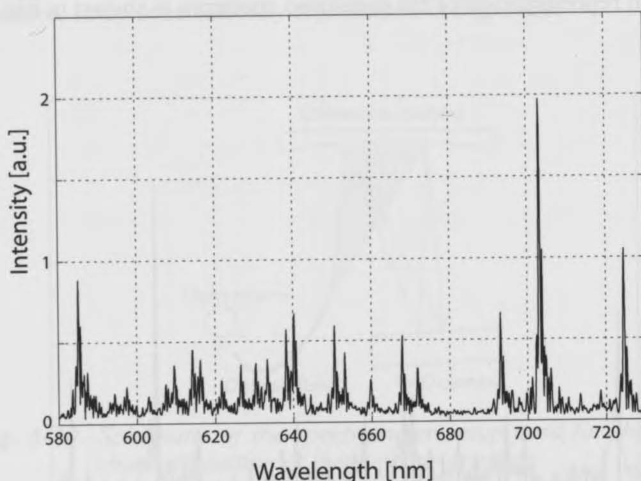

Fig. 5-23. Calculated contribution of light scattering from a rough grating surface to the spectrum of Neon.

The result of the calculation of scattering from a rough grating surface which contributes to the noise in spectral measurements is shown in Fig. 5-23. The calculated spectrum is in agreement with the experimental measurements presented in Fig. 5-22. There are limitations of the model used in the numerical calculations. The model is two-dimensional, while the real system has three dimensions. It also does not take optical aberrations into account, assuming that the imaging performance of the grating is perfect. However, the model provides a

convenient tool for the estimation of the grating performance in terms of the amount of scattered light if the grating surface quality is known.

5.5 Conclusions

A new technology for the fabrication of concave diffraction gratings had been developed and test gratings had been fabricated and characterized. This technology is based on a standard lithography and thus is compatible with the MEMS processing and conservers all the advantages of a planar lithography used for the fabrication of the flat diffraction optical elements.

The fabricated gratings were used in a very compact spectrograph setup and allowed for a subnanometer spectral resolution in the visible range.

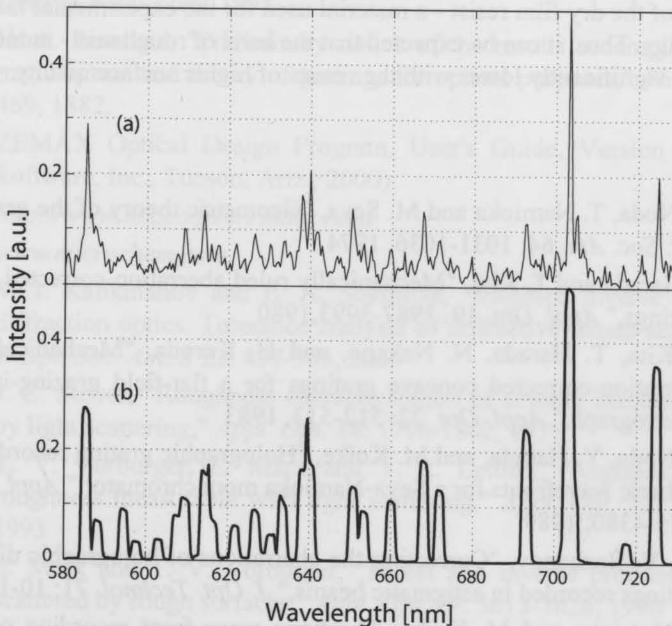

Fig. 5-24. *Ne spectrums measured using fabricated concave grating (a) and commercial spectrometer (b).*

Figure 5-24 shows a Ne spectrum which was measured with the fabricated concave grating (Fig. 5-24(a)) in comparison with the spectrum measured using a commercial 2 nm spectral resolution AvaSpec 2048 spectrometer [5.23] (Fig. 5-24(b)). It is clearly visible in Fig. 5-24 that the spectral resolution provided by the fabricated grating is higher than the resolution of AvaSpec spectrometer, since the FWHM of Ne spectral lines in Fig. 5-24(a) is smaller than that one in Fig. 5-24(b). However, low intensity spectral lines which are resolved by AvaSpec spectrometer, are not resolved by the spectrometer which uses the fabricated grating.

Thus, although fabricated gratings demonstrated an acceptable imaging performance, surface roughness of the gratings results in a stray light and ghost spectral lines which makes the measurements of spectra containing weak spectral lines located close to the strong ones difficult.

The main contribution to the roughness of the gratings is a low quality of the surface of the dry film resist - a material used for the experimental fabrication of the gratings. Thus, it can be expected that the level of roughness - induced stray light can be significantly lower with the resists of higher surface quality.

References

[5.1] H. Noda, T. Namioka and M. Seya, "Geometric theory of the grating," *J. Opt. Soc. Am.* 64: 1031-1036, 1974

[5.2] T. Harada and T. Kita, "Mechanically ruled aberration-corrected concave gratings," *Appl. Opt.* 19: 3987-3993,1980

[5.3] T. Kita, T. Harada, N. Nakano, and H. Kuroda, "Mechanically ruled aberration-corrected concave gratings for a flat-field grazing-incidence spectrograph," *Appl. Opt.* 22: 512-513, 1983

[5.4] H. Noda, Y. Harada, and M. Koike, "Holographic grating recorded using aspheric wavefronts for a Seya-Namioka monochromator," *Appl. Opt.* 28: 4375-4380, 1989

[5.5] Yu. V. Bazhanov, "Correcting the aberrations of holographic diffraction gratings recorded in astigmatic beams," *J. Opt. Technol.* 71: 10-14, 2004

[5.6] T. Namioka and M. Koike, "Aspheric wave-front recording optics for holographic gratings," *Appl. Opt.* 34: 2180-2186, 1995

[5.7] M. Duban, G. R. Lemaitre, and R. F. Malina, "Recording Method for Obtaining High-Resolution Holographic Gratings Through Use of Multimode Deformable Plane Mirrors," *Appl. Opt.* 37: 3438-3439, 1998

[5.8] Yongjun Xie, Zhenwu Lu, Fengyou Li, Jingli Zhao, and Zhicheng Weng, "Lithographic fabrication of large diffractive optical elements on a concave lens surface," *Opt. Express* 10: 1043-1047, 2002

[5.9] D. Radtke and U. D. Zeitner, "Laser-lithography on non-planar surfaces," *Opt. Express* 15: 1167-1174, 2007

[5.10] P. D. Maker, R. E. Muller, and D. W. Wilson, “Diffractive optical elements on non-flat substrates using electron beam lithography,”' US Patent. No. 6,480,333, assigned to California Institute of Technology, Pasadena, CA (1998).

[5.11] C. Palmer and W. R. McKinney, "Imaging theory of plane-symmetric varied line-space grating systems", *Opt. Eng.*, 33: 820-829, 1994.

[5.12] E. G. Loewen, E. Popov, *Diffraction gratings and applications*, Marcel Dekker, New York, 1997

[5.13] H. A. Rowland, "Preliminary notice of the results accomplished in the manufacture and theory of gratings for optical purposes," *Phil. Mag.* 13: 469, 1882.

[5.14] ZEMAX Optical Design Program, User's Guide, Version 9.0 (Focus Software, Inc., Tucson, Ariz., 2000)

[5.15] *http://www.tok.co.jp/en/index.html*

[5.16] *www.microchem.com*

[5.17] V. I. Kalikmanov and E. A. Sokolova, "Ill-posed inverse problem in diffraction optics. Tolerance analysis of diffractive lenses and gratings," *J. Opt. Soc. Am. A* 23: 497-503, 2006

[5.18] J. C. Stover, "Roughness characterization of smooth machined surfaces by light scattering," *Appl. Opt.* 14: 1796-1802, 1975

[5.19] T. V. Vorburger, E. Marx and T. R. Lettieri, "Regimes of surface roughness measurable with light scattering," *Appl. Opt.* 32: 3401-3408, 1993

[5.20] E. Marx and T. V. Vorburger, "Direct and inverse problems for light scattered by rough surfaces," *Appl. Opt.* 29: 3613-3626, 1990

[5.21] P. Beckmann and A. Spizzichino, *The Scattering of Electromagnetic Waves from Rough Surfaces*, Artech, Norwood, Mass., 1987

[5.22] K. Burns, K. B. Adams, and J. Longwell, "Interference measurements in the spectra of neon and natural mercury," *J. Opt. Soc. Am.* 40: 339-344, 1950

[5.23] AvaSpec 2048 spectrometer datasheet, *http://www.avantes.com*

6. Spectrometer with an external spherical mirror

The significant disadvantage of the planar spectrometers discussed in chapter 4 is a low optical throughput resulted from the small entrance aperture angle, or NA. Increasing this angle also increases optical aberrations, which degrades spectral resolution. The problem can be solved if non-planar elements are introduced into design. However, as more non-planar elements are added, the design becomes more complex and more difficult to fabricate. The spherical shape is the easiest one to fabricate, unlike the various types of aspheres. That is why the addition of a single spherical element is the easiest way to go from the production point of view.

Basically, there are two main approaches to design a spectrometer using a single spherical component. One of the alternatives, the use of a concave grating, is discussed in chapter 5. This chapter describes the second alternative which includes the use of a single simple spherical optical element (mirror) combined with a planar grating. All the spectrometer components except mirror are integrated on the same flat MEMS chip. The aberrations inherent to the spherical element are compensated by a specially designed non-linear structure of the grating grooves.

6.1 Concept of the microspectrometer with an external spherical mirror

The general configuration of a spectrometer (presented in Fig. 2-25 of chapter 2) assumes the use of at least two imaging components. The first component is for the collimation of light coming through the entrance slit and the second one is for the focusing of the diffracted light onto the photosensor [6.1]. Typically these imaging components are non-planar mirrors or lenses.

With the only one spherical component combined with a planar grating the imaging functionality can be provided in a way shown in Fig. 6-1. This design is a Monk-Gillison mounting [6.2]. However, a grating illuminated by a converging (or diverging) spherical wavefront, introduces aberrations into the diffracted field [6.3].

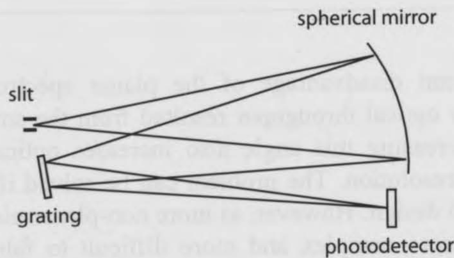

Fig. 6-1. *Monk-Gillison mounting[6.2].*

Another solution is to use the same non-planar component twice, for collimation and focusing. This implies that the grating should direct the diffracted light back, so that the light can be focused by the same element that is used for collimation. This approach had been described in 1889 by Ebert [6.4], but then this idea was buried until it was re-invented by Fastie in 1950's [6.5].

Fastie-Ebert mounting is illustrated in Fig. 6-2. The grating is tilted towards the input side mainly for symmetry reason. The provided symmetry allows partial compensation of coma. The main aberrations left are spherical one and astigmatism. Since in a spectrometer only meridional focusing is required, astigmatism is tolerated, and a proper grating position allows for a flat meridional field.

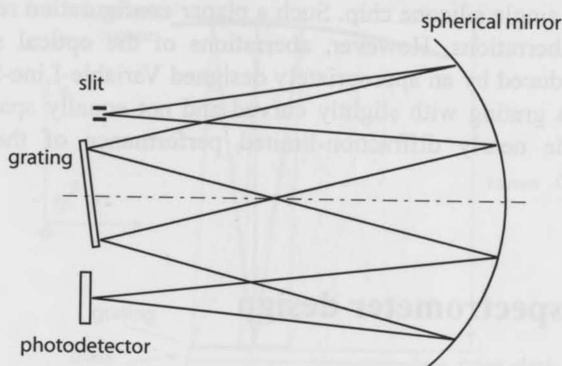

Fig. 6-2. *Fastie - Ebert spectrometer design.*

The Fastie-Ebert configuration is employed nowadays in commercially available devices such as a miniature Hamamatsu spectrograph with a spectral resolution of 9 nm and the dimensions of the optical part of 28x28x28 mm^3 [6.6].

The idea of using a single spherical mirror when applied to a microspectrometer design, implies that, unlike a classical Fastie-Ebert mounting, due to the planarity of the MEMS chip, the entrance slit, the grating and the image sensor are in the same plane. This concept is illustrated in Fig. 6-3.

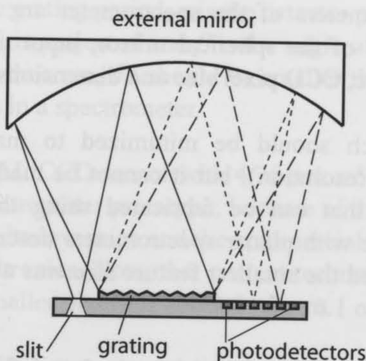

Fig. 6-3. *Concept of a microspectrometer with an external mirror.*

The entrance slit, diffraction grating and array of photodetectors are integrated on a single silicone chip. Such a planar configuration results in poorly compensated aberrations. However, aberrations of the optical system can be significantly reduced by an appropriately designed Variable-Line-Spacing (VLS) grating. Such a grating with slightly curved and not equally spaced grooves is able to provide nearly diffraction-limited performance of the spectrometer imaging system.

6.2 Microspectrometer design

6.2.1 Principal configuration and selection of the design parameters

The described concept has been implemented in the spectrometer design shown schematically in Fig. 6-4. It consists of a glass plate mounted on top of a commercial CCD sensor. The lithographically fabricated metal pattern on the glass plate integrates diffraction grating and transmission slit, which is illuminated using an optical fiber. The spherical mirror collimates light coming through the entrance slit and enables direction of the beam to the grating. The light diffracted in the first order is focused by the same mirror on the surface of the CCD chip.

The design parameters of the spectrometer are: pitch of the diffraction grating, focal distance of the spherical mirror, input numerical aperture (NA), operating spectral range, CCD pixel size and dimensions of the CCD sensor.

The grating pitch should be minimized to maximize dispersion (and consequently spectral resolution), but it cannot be made smaller than twice the smallest feature size that can be fabricated using the available lithographic system. As in the case with planar spectrometers described in chapter 4, in the fabrication process used the smallest feature size was about 0.7 - 0.8 μm, which set the grating period to 1.6 μm.

Focal distance of the spherical mirror in fact defines the largest dimension of the spectrometer.

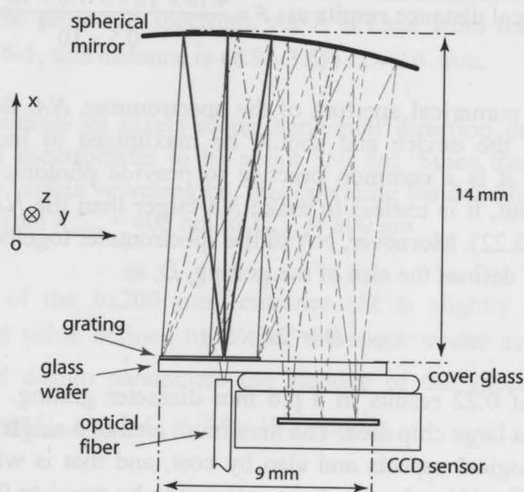

***Fig. 6-4.** Design of a spectrometer with an external spherical mirror.*

Focal distance of the mirror, detector pixel size and desired spectral resolution are connected. One can obtain the following formula using the grating equation:

$$F = \frac{pd\cos(\beta)}{\delta\lambda} \quad \textbf{(6.1)}$$

In Eq. (6.1) d is the grating period, p is the detector pixel width over which a spectral bandwidth of $\delta\lambda$ is projected and β is the angle of diffraction. According to the Nyquist sampling theorem, $\delta\lambda$ should be smaller than 0.5 nm to achieve a subnanometer resolution in a spectrometer.

The Sony ICX278AL CCD sensor with 4.75 μm x 5.55 μm pixels [6.7] has been selected for the spectrometer prototype, because of the relatively small pixel size and high sensitivity, its low price and the commercial availability of standard compatible read-out electronics. Note, that current technology allows fabrication of image sensors with smaller pixels of about 2 - 3 μm.

From Eq. (6.1) taking into account dimensional constraints and a 4.75 μm

pixel width, a focal distance results as: $F \approx \dfrac{4.75 \times 10^{-3} \times 1.6 \times 10^{-3} \times 1}{0.5 \times 10^{-9}} = 15$ mm.

The input numerical aperture of the spectrometer, *NA*, defines throughput (or etendue) of the device and should be maximized to increase sensitivity. However, since it is a common practice to provide photonic devices with an optical fiber input, it is useless to make *NA* larger than the *NA* of a multimode fiber (typically 0.22). Moreover, NA of the spectrometer together with the mirror focal distance *F* defines the size of the grating, *D*, as

$$D = 2F \times NA \tag{6.2}$$

The *NA* of 0.22 results in a 6.6 mm diameter grating. However, a large grating implies a large chip area. The maximum area of a single chip is limited by various technological aspects and also by cost, and that is why compromise is inevitable. Finally, *NA* value has been selected to be equal to 0.14, which results in a 4.2 mm grating.

Due to the very compact size of the spectrometer, the dimensions of the CCD sensor must be taken into account in the design. These parameters include: chip area, size of the chip housing, thickness of the sensor cover glass and distance from the cover glass to the surface of the CCD silicon chip. The main dimensional parameters of the sensor are shown in Fig. 6-5. The refractive index of a 0.75 mm thick cover glass is 1.5. The distance from the top of the cover glass to the surface of the 4.43 mm x 3.69 mm silicone image sensor chip is 1.94 mm. The sensing area of the chip is 3.65 mm x 2.74 mm.

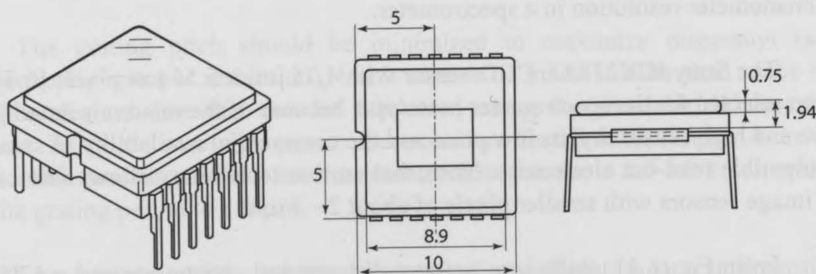

Fig. 6-5. *Sony ICX278AL CCD sensor [6.7].*

The size of the sensor packaging also defines the minimal distance from the entrance slit to the projected spectrum. As it is clear from the comparison of Fig. 6-4 and Fig. 6-5, this distance is $(8.9 - 3.65)/2 \approx 2.6$ mm.

The total number of pixels along horizontal direction defined operating bandwidth of the spectrometer to be about 350 nm. Since the CCD sensor is optimized for the visible wavelengths, this operating bandwidth can be selected within the range from $\lambda_{min} = 400$ nm to $\lambda_{max} = 800$ nm.

The width of the 6x200 μm^2 entrance slit is slightly larger than the diffraction-limited value defined by NA of the spectrometer as $d = \lambda_{max}/NA$. With the selected design parameters the etendue of the spectrometer can be calculated as: $G = \pi l_{slit} w_{slit} NA^2 = 7.4 \times 10^{-5}$ $mm^2 sr$.

6.2.2 Ray tracing design and optimization

As with the spectrometer described in the previous chapters, a ray tracing software ZEMAX [6.8] has been used for optical design.

The starting point in the design process was a modified "W" - type Fastie-Ebert configuration in which a diffraction grating with straight grooves was parallel to the image sensor. This configuration is illustrated in Fig. 6-6.

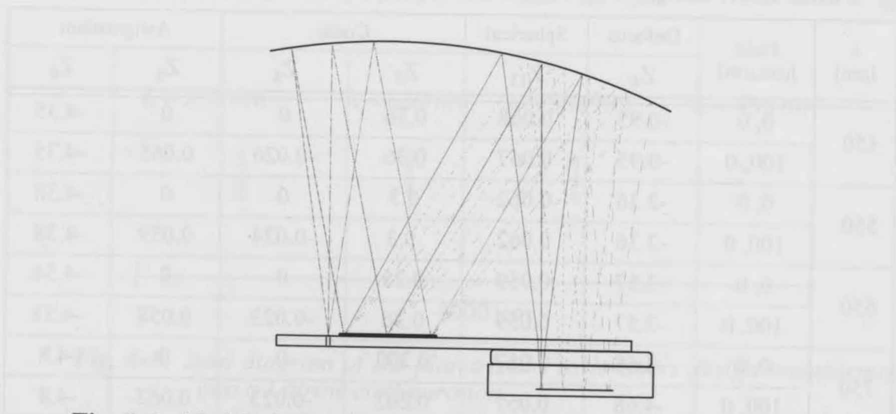

Fig. 6-6. Modified Ebert-Fastie configuration - starting point in the design.

The corresponding spot diagram calculated for the fields of (0 μm, 0 μm), (100 μm, 0 μm) and (-100 μm, 0 μm) is shown in Fig. 6-7.

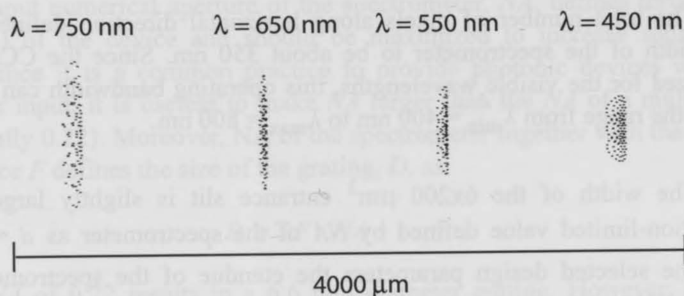

Fig. 6-7. Spot diagram of the modified (planar) Ebert-Fastie configuration.

As it was mentioned in section 6.1, due to the parallel position of the grating the system symmetry is distorted and the optical performance is degraded by various optical aberrations. The main aberration coefficients at the wavelength of 450 nm, 550 nm, 650 nm and 750 nm are presented in Table 1 for the field values of (0 μm, 0 μm) and (100 μm, 0 μm).

TABLE 1. ***The main aberration coefficients of the modified (planarized) Fastie-Ebert design.***

λ [nm]	Field [μm,μm]	Defocus	Spherical	Coma		Astigmatism	
		Z_4	Z_{11}	Z_7	Z_8	Z_5	Z_6
450	0, 0	-0.95	0.068	0.36	0	0	-4.35
	100, 0	-0.95	0.067	0.36	-0.026	0.065	-4.35
550	0, 0	-2.36	0.062	0.3	0	0	-4.38
	100, 0	-2.36	0.062	0.3	-0.024	0.059	-4.38
650	0, 0	-3.57	0.059	0.25	0	0	-4.54
	100, 0	-3.57	0.059	0.26	-0.023	0.058	-4.53
750	0, 0	-4.68	0.057	0.202	0	0	-4.8
	100, 0	-4.68	0.057	0.202	-0.023	0.062	-4.8

Moving the entrance slit as close to the CCD imager as is possible within the sensor package transforms the spectrometer configuration into a Littrow arrangement as shown in Fig. 6-8. In Fig. 6-8 light comes into spectrometer through a slit in the diffraction grating. In practice such a slit could be easily realized lithographically.

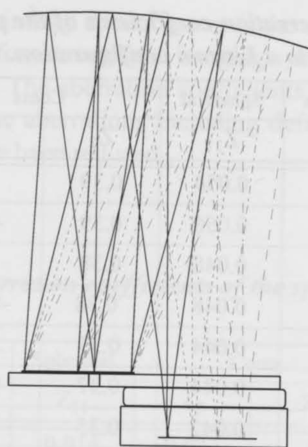

Fig. 6-8. Planarized Fastie-Ebert design transformed into a Littrow configuration.

The corresponding spot diagram calculated for the fields of (0 μm, 0 μm), (100 μm, 0 μm) and (-100 μm, 0 μm) is shown in Fig. 6-9.

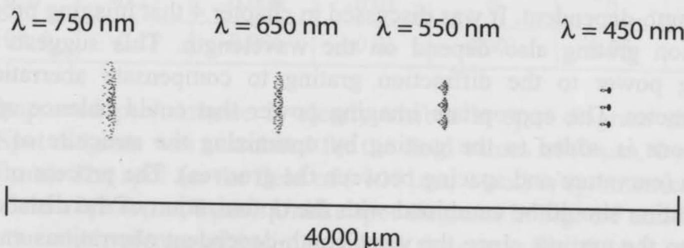

Fig. 6-9. Spot diagram of the planarized Fastie-Ebert design transformed into a Littrow configuration.

Such a transformation reduces some of the aberrations as it is visible from the comparison of spots diagrams in Fig. 6-7 and Fig. 6-9 and also the size of the spectrometer becomes smaller. The main aberration coefficients of the mounting shown in Fig. 6-8 are listed in Table 2.

TABLE 2. ***The main aberration coefficients of the planarized Fastie-Ebert design transformed into a Littrow configuration.***

λ [nm]	Field [μm,μm]	Defocus	Spherical	Coma		Astigmatism	
		Z_4	Z_{11}	Z_7	Z_8	Z_5	Z_6
450	0, 0	0.093	0.056	0.39	0	0	-0.92
	100, 0	0.093	0.056	0.39	-0.02	-0.038	-0.92
550	0, 0	-0.58	0.048	0.38	0	0	-1.19
	100, 0	-0.58	0.048	0.38	-0.017	-0.033	-1.19
650	0, 0	-1.21	0.044	0.37	0	0	-1.47
	100, 0	-1.2	0.044	0.37	-0.016	-0.028	-1.47
750	0, 0	-1.81	0.042	0.35	0	0	-1.76
	100, 0	-1.81	0.042	0.35	-0.015	-0.022	-1.76

As it follows from Table 2, transforming spectrometer into a Littrow configuration had helped to significantly reduce such aberrations as defocus and astigmatism and also made spherical aberration smaller.

According to Table 2, the aberrations of the spectrometer are strongly wavelength-dependent. It was discussed in chapter 4 that imaging properties of a diffraction grating also depend on the wavelength. This suggests to add an imaging power to the diffraction grating to compensate aberrations of the spectrometer. The appropriate imaging power that could balance spectrometer aberrations is added to the grating by optimizing the structure of the grating grooves (curvature and spacing between the grooves). The process of the grating optimization should be combined with the optimization of the distance from the mirror to the grating, since the wavelength-dependent aberrations vary with the position of the mirror.

The principles of modelling a diffraction grating in ZEMAX are described

in details in chapter 4, section 4.2.3. The optimization functionality of ZEMAX was used to find a set of grating coefficients which provides the smallest possible size of the spectrometer entrance slit image at the wavelengths within the spectrometer operating range in the *oy* direction, which is the direction of the dispersion in the image plane (see Fig. 6-4). Simultaneous optimization of the mirror position and grating coefficients completed the design process.

The layout of the optimized spectrometer is the same as that one shown in Fig. 6-8. However, the performance of the imaging system has been considerably improved by optimization. The aberration coefficients of the resulted system are listed in Table 3. All of the aberrations including defocus, spherical aberration, coma and astigmatism have been reduced.

TABLE 3. ***The main aberration coefficients of the spectrometer design with the optimized grating.***

λ [nm]	Field [μm,μm]	Defocus	Spherical	Coma		Astigmatism	
		Z_4	Z_{11}	Z_7	Z_8	Z_5	Z_6
450	0, 0	0.26	0.014	0.027	0	0	0.57
	100, 0	0.26	0.014	0.027	-0.004	0.035	0.57
550	0, 0	0.22	0.004	0.018	0	0	0.28
	100, 0	0.22	0.004	0.019	-0.001	0.004	0.28
650	0, 0	0.037	-0.002	0.005	0	0	-0.02
	100, 0	0.036	-0.002	0.006	0.0003	0.045	-0.02
750	0, 0	-0.23	-0.006	-0.01	0	0	-0.23
	100, 0	-0.23	-0.006	-0.01	0.001	0.05	-0.32

The improved performance is clearly visible in spot diagram shown in Fig. 6-10. Spot diagram was calculated for the field values of (0 μm, 0 μm) and (100 μm, 0 μm). The spot for the field of (-100 μm, 0 μm) is symmetrical to the one for the field of (100 μm, 0 μm). Unlike spot diagrams in Fig. 6-7 and Fig. 6-9, which give the whole picture of the image plane, the one in Fig. 6-10 is presented in a magnified scale to provide a better view of small spots. Each of the spots in Fig. 6-10 is shown in comparison with a scale bar and the corresponding Airy Disk. Thus, it is clear that the system is diffraction limited in the direction of the

dispersion (*oy* direction in Fig. 6-4). The best performance is at the wavelength of 650 nm. Astigmatism observable at other wavelengths is tolerated, since the spot size in the direction normal to the direction of the dispersion does not limit spectral resolution.

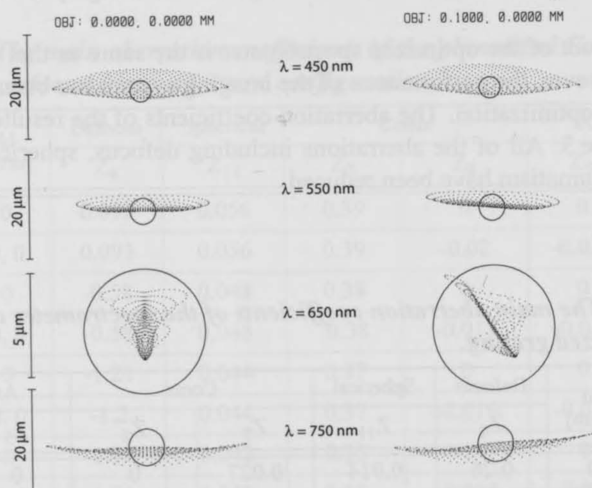

Fig. 6-10. *Spot diagram of the spectrometer with optimized grating.*

The largest dimension of the optimized spectrometer defined by the mirror position is 14 mm (Fig. 6-4) and the size of the glass chip is 4.2 x 9 mm^2.

6.2.3 Estimation of spectral resolution

The linear dispersion in the image plane *D* and the geometrical image width of the entrance slit *S* can be easily calculated from spot diagrams. The realistic width of the entrance slit can be obtained with the diffraction image analysis in ZEMAX, which accounts for the aberrations and diffraction effects [6.8]. The diffraction slit width is determined as a Full Width at Half Maximum (FWHM).

The values calculated using ZEMAX are presented in Table 4. Linear dispersion, slit width and, consequently, spectral resolution slightly depend on the wavelength. According to the results presented in Table 4, the spectrometer resolution is 0.63 nm - 0.67 nm.

TABLE 4. ***Linear dispersion, slit image width and spectral resolution depending on the wavelength.***

Wavelength, nm	450	550	650	750
Dispersion, nm/μm	0.105	0.103	0.1	0.1
Geometrical slit width, μm	6	6.2	6.3	6.43
Diffraction slit width, mm	6	6.2	6.3	6.7
Spectral resolution, nm	0.63	0.64	0.63	0.67

To give the impression about the imaging system performance, Fig. 6-11 shows a simulated image projected on the surface of CCD sensor when the entrance slit of the spectrometer is illuminated with a light which spectrum includes two equal monochromatic lines at wavelength of 750 nm and 750.67 nm. The image in Fig. 6-11 had been calculated using diffraction image analysis in ZEMAX. As it is visible in Fig. 6-11, two wavelength are just resolved, which is in agreement with the value of resolution at the wavelength of 750 nm given in Table 4. The edges of lines in Fig. 6-11 are blurred which is due to astigmatism present in the system.

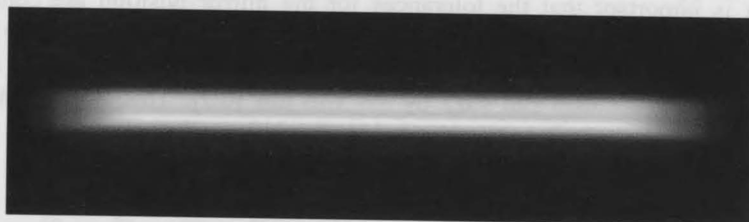

Fig. 6-11. *Image projected on a CCD sensor when the spectrometer entrance slit is illuminated by the wavelengths of 750 nm and 750.67 nm (calculated using diffraction image analysis in ZEMAX).*

The resolution of real spectrometer will be lower the that one predicted in Table 4. The reason is that the CCD sensor pixel pitch is 4.75 μm which is larger than 3 μm required to resolve a 6 μm thick line according to sampling theorem. The smallest line width will be registered by CCD sensor in the case when line image falls in the center of a pixels column.

6.2.4 Tolerances

Most of the spectrometer components including entrance slit, diffraction grating and image sensor are integrated and automatically aligned. The only component to be additionally aligned is the external spherical mirror.

The tolerances for the positioning of the mirror can be defined under condition that spectral resolution is kept below 1 nm. With this condition the tolerances for the distance between mirror and image plane (direction *ox* in Fig. 6-4)have been determined to be +/- 20 μm.

The change of the lateral position (direction *oy* in Fig. 6-4) of the mirror results in the shift of the spectral bandwidth projected on the image sensor. Quantitatively, a 100 μm displacement of the mirror results in a 20 nm spectral shift. However, the resolution is also degraded during such movements of the mirror. Having limited spectral resolution to be less than 1 nm, the tolerances for lateral mirror displacement have been determined to be +/-150 μm.

The tolerances for the lateral positioning of the mirror in the normal direction to the direction of the dispersion (*oz* direction in Fig. 6-4) are +/-250 μm.

It is important that the tolerances for the mirror position are computed assuming that the distance from the CCD sensor cover glass to the surface of the silicone CCD chip is precisely fixed. In practice, according to the CCD sensor data sheet, the distance can vary by +/- 150 μm [6.7]. This implies that the distance from the mirror to the glass chip should be adjusted according to the actual CCD sensor.

6.2.5 Stray light

The potential sources of the stray light in the spectrometer include light scattering by mirror and grating. The surface quality of the mirror is scratch-dig 60-40, which is a high commercial standard. The surface quality of the grating is defined by the quality of the polished glass wafer, since the deposited aluminium film does not add extra roughness. That is why there is no considerable stray light can be expected.

6.2.6 Grating diffraction efficiency.

The profile of the diffraction grating fabricated lithographically is rectangular. As in the case of planar spectrometers described in chapter 4, the depth of the grating grooves should be optimized for maximum efficiency in the desired diffraction order. The wavelength of 600 nm (central wavelength of the spectrometer operating range) was selected for the optimization of the groove depth. The dependency of the grating efficiency on the depth of the grooves computed using PCGrate software [6.9] is shown in Fig. 6-12. The grating operates in the spectrometer in the -1 diffraction order. According to Fig. 6-12, an efficiency of more than 30% can be expected for a grating with 160 +/- 30 nm deep grooves.

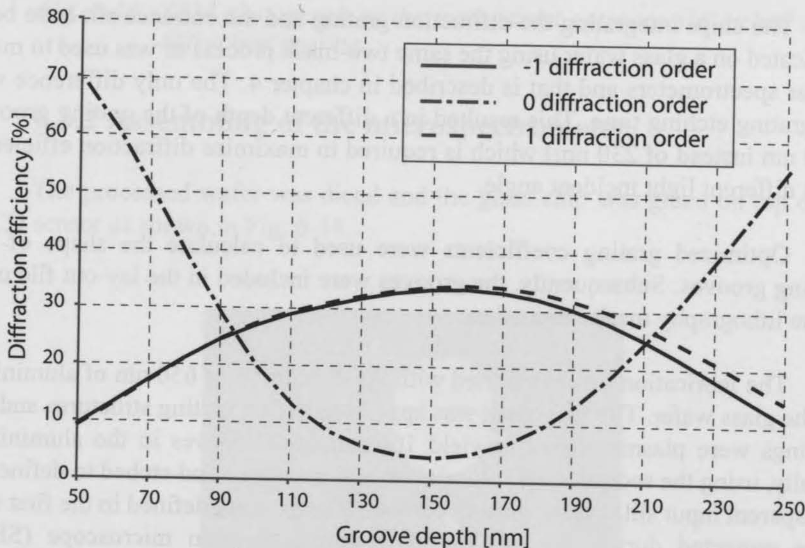

Fig. 6-12. Grating efficiency vs groove depth at the wavelength of 600 nm.

Since the angle of incidence is small (2.7 degrees) as it is visible in Fig. 6-4, the grating orders are almost symmetrical relative the grating normal. That is why the efficiencies of the orders 1 and -1 are very close to each other as shown in Fig. 6-12.

The efficiency of the -1 order is higher for the gratings with a smaller pitch

and higher incident angle. For example, with the angle of incidence of 20 degrees and the grating pitch of 0.8 μm only zero and minus first diffraction orders exist at the wavelength of 600 nm as follows from the grating equation. In such a configuration the depth of the rectangular grooves can be optimized to yield a 60% efficiency in the -1 order (according to numerical simulations).

6.3 Fabrication and characterization of the microspectrometer

6.3.1 Fabrication of the glass chips

The chips integrating the diffraction grating and the entrance slit have been fabricated on a glass wafer using the same two-mask process as was used to make planar spectrometers and that is described in chapter 4. The only difference was the grating etching time. This resulted in a different depth of the grating grooves (160 nm instead of 230 nm) which is required to maximize diffraction efficiency for a different light incident angle.

Optimized grating coefficients were used to calculate the shape of the grating grooves. Subsequently, the grooves were included in the lay-out file used in the lithography mask fabrication.

The fabrication process started with the deposition of 650 nm of aluminium on the glass wafer. The first mask was applied to define grating structures and the gratings were plasma etched to yield 160 nm deep grooves in the aluminium. Finally, using the second mask, aluminium was patterned and etched to define the transparent input slit and the grating contour. The grooves defined in the first step were protected during the etching. A scanning electron microscope (SEM) photograph of the transparent slit etched in the aluminium grating is shown in Fig. 6-13.

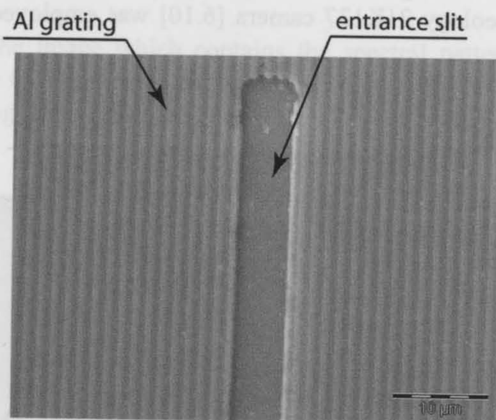

Fig. 6-13. SEM photograph of the transparent entrance slit etched in the diffraction grating.

6.3.2 Assembling of the microspectrometer.

The processed wafer was diced and the glass chip was glued on top of the CCD sensor as shown in Fig. 6-14.

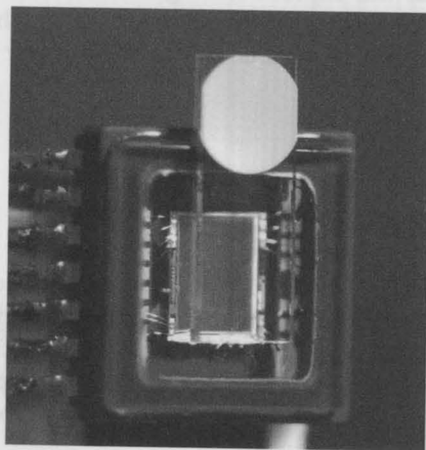

Fig. 6-14. Glass chip with aluminum grating and entrance slit glued on top of the CCD sensor cover glass.

The device was aligned with a spherical mirror (see Fig. 6-15) and the electronics of Videology 21K137 camera [6.10] was employed for signal read-out.

Fig. 6-15. *Spectrometer chip aligned with a spherical mirror. Cleaved fiber tip visible in the left is used to illuminate the entrance slit of the spectrometer.*

A multimode optical fiber with a 100 μm core was used for light delivery. A cleaved tip of the fiber was exposed to a light source under test and the second fiber tip was aligned to illuminate the entrance slit of the spectrometer. The resulting spectral pattern was captured by the CCD sensor and observed on the computer screen.

6.3.3 Experimental characterization of the microspectrometer

The efficiency of the fabricated gratings was measured using a He-Ne laser to be 31% in the first order (at 632 nm wavelength), which is smaller than 34% predicted by numerical simulation in PCGrate. Such a discrepancy is due to the imperfections of the fabricated grating profile (the real profile is not exactly rectangular, but has rounded groove edges, see the discussion in chapter 4)

The performance of the spectrometer was characterized experimentally with

a Ne lamp as a test light source.

A part of the image which contains the spectral pattern of Ne and was captured with the CCD sensor is shown in Fig. 6-16. Different Ne spectral lines can be easily recognized in the image.

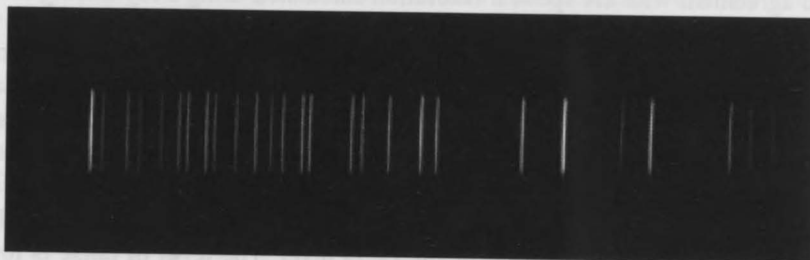

Fig. 6-16. *Part of the image captured by CCD sensor when the entrance slit is illuminated by Ne light.*

Graphical representation of Ne spectrum measured in the range allowed by the spectrometer (from 420 nm to 770 nm) is presented in Fig. 6-17.

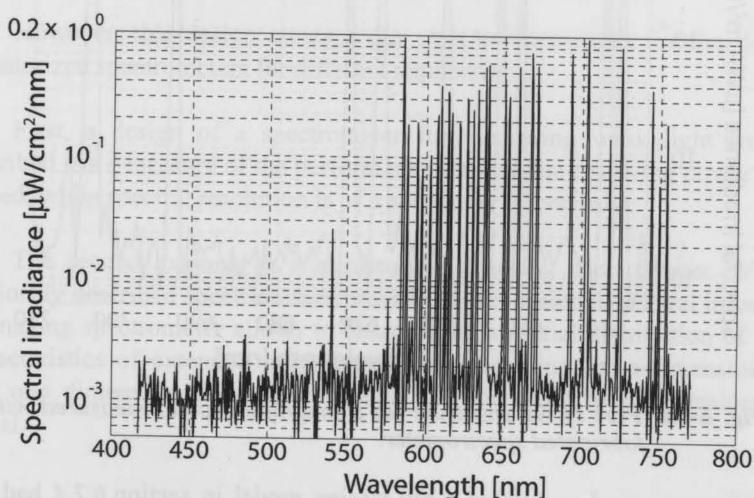

Fig. 6-17. *Neon spectrum measured with the fabricated spectrometer.*

Before actual spectral measurements, CCD camera had been calibrated using laser light and power meter, which allows to interpret measured spectra in spectral irradiance units.

The FWHM resolution of the spectrometer is estimated from the width of a single spectral line in Fig. 6-17 to be approximately 0.7 nm. This value is in a good agreement with the spectral resolution calculated using a ray tracing model (section 6.2.3).

The magnified part of the measured Ne spectrum is presented in Fig. 6-18. Several peaks are marked with the corresponding measured wavelength values in Fig. 6-18 to identify them with the Ne spectral lines. The numbers in brackets are reference values from [6.11]. The positions of spectral lines registered by the spectrometer can be defined with the precision of about 0.3 - 0.4 nm. This precision is limited by the width of the CCD pixel. The level of noise is lower than 0.2%, which allows registration of very weak spectral peaks.

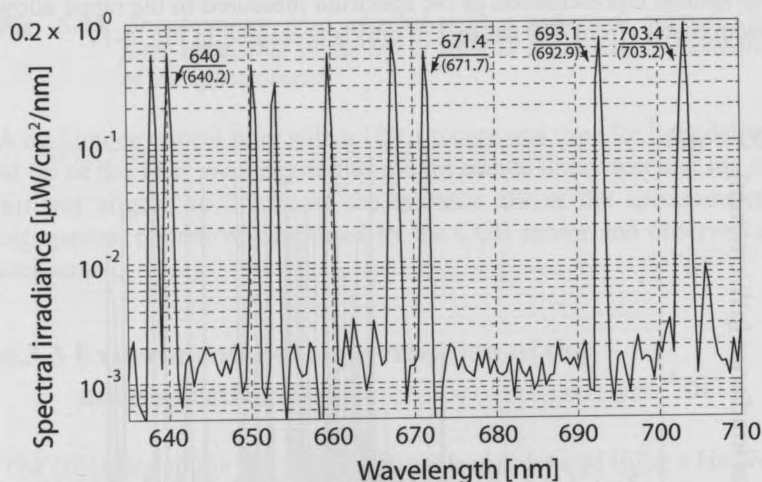

Fig. 6-18. *Part of Ne spectrum (in a magnified scale) measured with the fabricated spectrometer.*

Tolerances predicted using a ray tracing model in section 6.2.4 had been confirmed experimentally. Spectrum of Ne lamp contains a set of monochromatic lines and each spectral line illuminates maximum 2 rows of adjacent CCD pixels

in the spectrometer.

The tolerance for the distance between mirror and CCD sensor (direction *ox* in Fig. 6-4) has been experimentally determined to be about +/- 20 μm. When the mirror position is within the tolerance bounds, 2 rows of pixels are illuminated by a spectral line and the resolution of the spectrometer is better than 1 nm. If the mirror displacement is larger than the specified tolerance, more than 2 pixel rows are illuminated, which implies degradation of the resolution by more than 30% as compared to the best possible value (0.7 nm). The movement of the mirror parallel to the image plane (direction *oy* in Fig. 6-4) results in a shift of the spectral range projected on the CCD sensor, without the significant loss of spectral resolution. The adjustment of the mirror position can be used to select a 350 nm operating bandwidth in the range from 400 nm to 800 nm

6.4 Modifications of the microspectrometer

The spectrometer design described in section 2 of this chapter is targeted at maximizing spectral resolution under dimensional constraints and constraints imposed by the used lithographic technology and available image sensor.

However, this design concept can also be considered for the design of miniaturized spectrometers for different applications.

First, a design of a spectrometer for measuring weak light sources is described. As a measure of the performance the etendue-resolving power product is used, while spectral resolution is of a secondary importance.

The second example is a miniaturized imaging spectrometer. While the previously described spectrometers provide on-dimensional spectral information, an imaging spectrometer allows to characterize a spatial distribution of spectral characteristics of extended light sources by measuring three-dimensional data with one dimension being spectral one and the other two dimensions being spatial.

6.4.1 Design for maximising etendue-resolving power product

The amount of light which can be collected by a spectrometer is characterized by etendue or optical throughput defined as (see section 2.3.6):

$$G = \pi \times S_x \times S_y \times NA^2 \tag{6.3}$$

In Eq. (6.3) S_x and S_y are the width and the length of the entrance slit respectively and *NA* is the entrance numerical aperture of the spectrometer. The etendue value is important, since more light can collect a spectrometer, more sensitive it is. However, etendue is coupled to resolution. As it is shown in chapter 2, in a spectrometer with a perfect imaging system spectral resolution $\Delta\lambda$ is inversely proportional to the width of the entrance slit S_x. That is why an etendue resolving power product is used for evaluation of the spectrometer:

$$GR = \pi \times S_x \times S_y \times NA^2 \times \lambda / \Delta\lambda \tag{6.4}$$

In Eq. (6.4) λ is the operating wavelength of the spectrometer and $\Delta\lambda$ is spectral resolution.

When aberrations of the spectrometer optics are small, the value of GR does not depend on spectral resolution. However, as aberrations became larger, a higher value of GR can be obtained if resolution is tolerated to a lower value. This is clear if the image width of the entrance slit is presented as a sum of widths of gaussian image and image blurring due to aberrations as $D = D_{gaus} + D_{aberr}$. The value of D_{aberr} weakly depends on S_x, while $D_{gauss} = mS_x$, where *m* is the magnification of optical system. Thus, since $\Delta\lambda \sim D$:

$$GR \sim \frac{S_x}{D_{gauss} + D_{aberr}} = \frac{S_x}{mS_x + D_{aberr}} = \frac{1}{m} \times \frac{1}{1 + \frac{D_{aberr}}{mS_x}} \tag{6.5}$$

It follows from the Eq. (6.5), that GR is larger for larger S_x.

In the design of a spectrometer with maximized etendue-resolving power

product, the following principles had been followed:

- *NA* is set to 0.22, which is a typical *NA* of optical fiber and many commercial spectrometers.
- The length of the entrance slit is maximized.
- The increased *NA* always results in larger optical aberrations, so the performance of the spectrometer optics is not expected to be diffraction-limited. Thus, the width of the entrance slit is balanced according to Eq. (6.5) to maximize *GR* taking aberrations into account and also trying to make resolution as high as possible.
- There are no technology limitations, so the grating pitch can be made as small as desired.
- The design assumes that Sony ICX278AL CCD sensor is used to capture spectral pattern.

The design of the spectrometer is illustrated in Fig. 6-19.

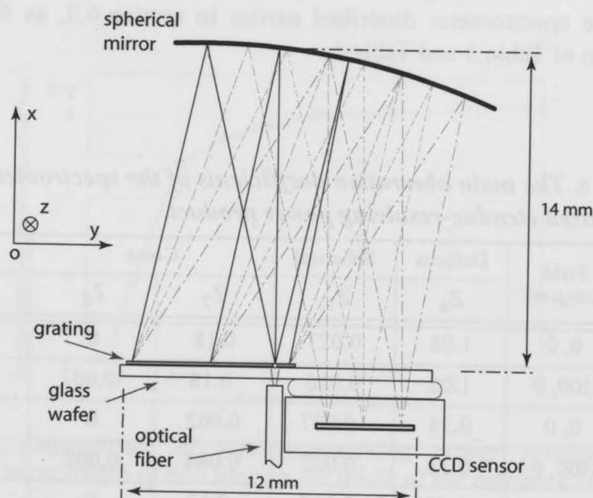

Fig. 6-19. Design of the spectrometer with maximized etendue-resolving power product.

This design configuration is similar to the one shown in Fig. 6-4. However, design parameters are different.

In order to increase dispersion, the grating pitch was set to 1 μm. This results in larger diffraction angles and, as a consequence, in larger spectrometer dimension in *oy* direction (12 mm). Making grating pitch smaller than 1 μm is not practical, since larger diffraction angles also result in larger aberrations which can not be compensated by the grating design. Thus, the benefits of the higher dispersion are annihilated by the increased aberrations. The increased dispersion has also reduced spectral bandwidth projected over the image sensor, making the operating range of the spectrometer to be about 230 nm.

The length of the entrance slit had been set to 600 μm in order to increase throughput. This value is within the range of slit lengths used in commercial spectrometers (from 500 μm to 1000 μm). For larger value of the slit length, optical aberrations for the extreme field points become unacceptably large.

Since *NA* is increased to 0.22, optical aberrations are also increased and imaging system is not diffraction limited. The aberration coefficients of the spectrometer as calculated in ZEMAX are listed in Table 5. Aberrations are symmetrical relative to the central wavelength of the operating range with the minimum at this wavelength. The amplitude of the aberrations is larger than in the case of the spectrometer described earlier in section 6.2, as follows from the comparison of Table 3 and Table 5.

TABLE 5. ***The main aberration coefficients of the spectrometer with maximized etendue-resolving power product.***

λ [nm]	Field [μm,μm]	Defocus	Spherical	Coma		Astigmatism	
		Z_4	Z_{11}	Z_7	Z_8	Z_5	Z_6
550	0, 0	1.08	0.027	0.18	0	0	1.8
	300, 0	1.05	0.028	0.18	-0.007	0.1	1.8
650	0, 0	0.34	-0.007	0.062	0	0	0.24
	300, 0	0.32	-0.007	0.064	0.002	0.23	0.26
750	0, 0	-1.07	-0.027	-0.12	0	0	-1.5
	300, 0	-1.1	-0.027	-0.12	0.003	0.36	-1.5

Diffraction image analysis in ZEMAX had been used to calculate spectral resolution for different values of the entrance slit widths.

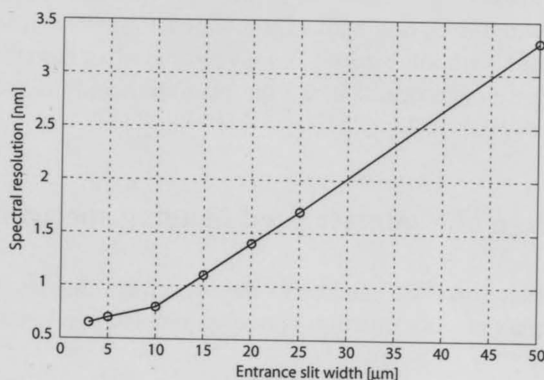

Fig. 6-20. *Dependence of spectral resolution on the width of the entrance slit.*

The computed dependence of spectral resolution on the width of the slit is shown in Fig. 6-20. The highest resolution possible is about 0.6 nm if the slit width is 3 μm.

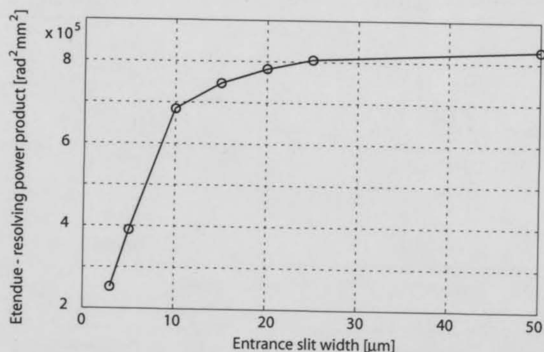

Fig. 6-21. *Dependence of etendue-resolving power product (at the wavelength of 600 nm) on the width of the entrance slit.*

Substituting calculated values of resolution and design parameters into Eq. (6.4), the dependence of the etendue-resolving power product had been obtained. The behaviour of this dependence which is presented in Fig. 6-21 is in a qualitative agreement with the Eq. (6.5). It follows from the Fig. 6-21 that the

optimal value of etendue-resolving power product is about $8x10^5$ $\mu m^2 rad^2$, which can be achieved with the entrance slit 25 μm wide and spectral resolution of about 1.7 nm. If spectral resolution below 1 nm is required, than the entrance slit width can be set at 10 μm which results in 0.8 nm resolution and the etendue-resolving power product of $7x10^5$ $\mu m^2 rad^2$.

6.4.2 Design of a miniaturized imaging spectrometer

Imaging spectrometers measure the spectral characteristics of light collected from an object as a function of two spatial and one spectral dimensions.

Imaging spectrometers can be divided into classes based on the methods by which they achieve spatial and spectral discrimination. Corresponding classification is given in Table 6 according to [6.12].

TABLE 6. ***Classification of imaging spectrometers (according to [6.12]).***

	Spatial scanning			
Spectral discrimination	Whiskbroom	Pushbroom	Windowing	Framing
Filtering	Multiband radiometer		Filter array Linear variable filter Wedge filter	Band-sequential Filter wheel Tunable filter
Dispersive	Grating or prism	Grating or prism		Image slicer Tomographic
Interferometric	FTS (Michelson)	FTS (Sagnac)	FTS (Mach-Zander, Sagnac	FTS (Michelson)

Whiskbroom spectrometers can measure spectral information only for a single point-like Field Of View (FOV) which is scanned over the object. One-dimensional extended FOV can be measured using pushbroom spectrometers. Thus, to acquire a compete spectral dataset with a pushbroom instrument, this one-dimensional FOV is moved along the object. In windowing instruments a two-dimensional FOV is moved gradually over the object, while in framing

instruments a two dimensional FOV is fixed on the object.

Grating based spectrometers can be used to realize a whiskbroom or a pushbroom system. The advantage of a pushbroom system is a faster data acquisition and a simpler scanning mechanism. However, the requirements to the imaging optics of a spectrometer used in a pushbroom instruments are more demanding since the imaging is in two dimensions and astigmatism can not be tolerated.

Pushbroom grating based systems are often used in aerospace applications for mapping chemical substances over the earth surface or in the atmosphere. One-dimensional scanning in such a pushbroom system is provided by the movement of the sensor platform (space- or aircraft). The principles of the operation of an airborne pushbroom imaging spectrometer are illustrated in Fig. 6-22 (according to [6.13]).

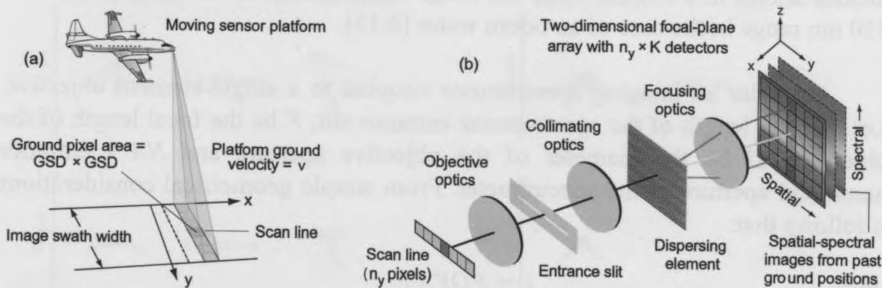

Fig. 6-22. Pushbroom spectrometer operation principles (from [6.13]). Geometry of a spectroscopic pushbroom imaging system (a). Main components of an imaging spectrometer (b).

The area coverage rate is the swath width (cross-track direction) multiplied by the platform ground velocity, and the area of a pixel on the ground is the square of ground sample distance (GSD). The swath width defines FOV of the spectrometer, while the size of a single ground pixel defines instantaneous FOV (IFOV). Ground pixels are imaged onto the spectrometer entrance slit by the objective optics and are dispersed by the spectrometer onto the two-dimensional image sensor. Thus, each pixel column of the sensor contains spectral information of a certain ground pixel.

Typical range of the requirements to pushbroom imaging spectrometers is summarized in Table 7 (according to [6.14]).

TABLE 7. ***Typical requirements to the pushbroom imaging spectrometers ([6.14]).***

FOV	2 deg - 32 deg
IFOV	50 μrad - 0.6 mrad
Spectral range	450 nm - 1000 nm, 1000 nm - 2500 nm
Spectral sampling (resolution)	5 nm - 15 nm

The requirement for a wide wavelength operating region given in Table 7 is a consequence of using a single instrument for multiple applications. A single application often requires measuring spectrum in a smaller wavelength range. For example, the mapping of chlorophyll concentration in water requires measurements in a 660 nm - 715 nm range in the case of lakes and in a 400 nm - 550 nm range in the case of an ocean water [6.15].

Consider an imaging spectrometer coupled to a single-element objective. Let s be the length of the spectrometer entrance slit, F be the focal length of the objective, D be the diameter of the objective aperture and NA - entrance numerical aperture of the spectrometer. From simple geometrical considerations it follows that:

$$\begin{aligned} s &= FOV \times F \\ D &= 2NA \times F \\ FOV &= \frac{2s \times NA}{D} \end{aligned} \quad \textbf{(6.6)}$$

The importance of the Eqs. (6.6) is the link between the parameters of the spectrometer and those of the objective. Although Eqs. (6.6) have been derived for an objective consisting of a single element (a single lens or a mirror), the conclusion that can be drawn from the Eqs. (6.6) is valid also for other objectives: large FOV requires either a long entrance slit or a small objective aperture.

In a miniaturized spectrometer which is described in section 6.2 the entrance slit is, naturally, also small. Thus, such a microspectrometer is most suitable to be used in an imaging system with a small FOV.

The layout of the miniaturized imaging spectrometer is the same as shown in Fig. 6-4. In order to use some reference point in the design, it is supposed that the imaging spectrometer is based on Sony ICX278AL CCD sensor [6.7] which is also employed in the system described in section 6.2. The wavelength operating range is set to 450 nm - 950 nm. The mirror focal distance (15 mm) and sensing area of the CCD chip define the spectrometer entrance slit length and linear dispersion (consequently, grating pitch). As a result, the length of the entrance slit was set to 2.7 mm and grating pitch was set to 2.3 μm. The *NA* of the spectrometer is 0.2.

In the same way as it is described in section 6.2, the parameters of the spectrometer had been optimized using ZEMAX. However, the goal of the optimization was to reduce the spot size both in *oy* and *oz* directions, not in the direction of the dispersion only, as in section 6.2. The resulting spot diagram is shown in Fig. 6-23 for the field values of (0 mm, 0 mm) and (1.35 mm, 0 mm).

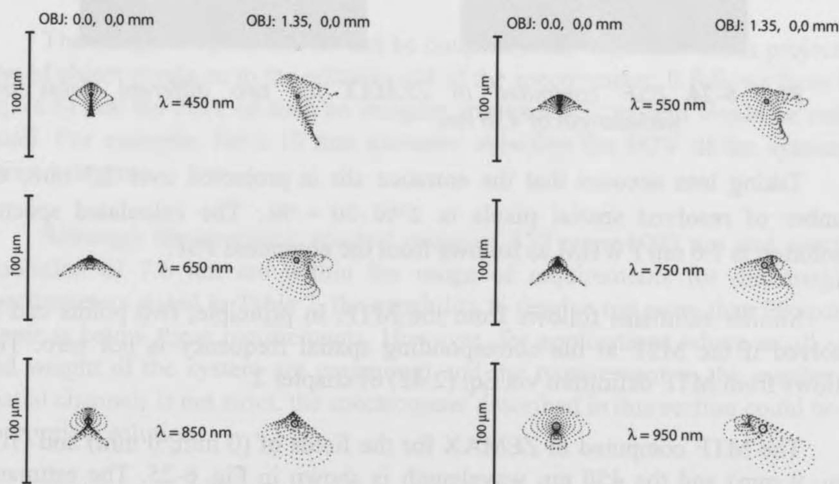

***Fig. 6-23.** Spot diagram of the spectrometer optimized for imaging applications (computed in ZEMAX).*

The size of the spot which defines spectral and spatial resolution of the spectrometer is approximately the same for all wavelength in the operating bandwidth as it is visible in Fig. 6-23. Imaging system of the spectrometer is not diffraction limited and the maximum number of resolved pixels can be estimated

using PSF or MTF. As an example, Fig. 6-24 shows PSF computed in ZEMAX for the field values of (0 mm, 0 mm) and (1.35 mm, 0 mm) and the wavelength of 450 nm. The largest spot is obtained for a larger field. Estimated at half of the maximum value, the PSF size is about 30 x 50 μm^2 in *oz* and *oy* directions respectively. Approximately the same PSF size is obtained at other wavelengths of the spectrometer operating bandwidth.

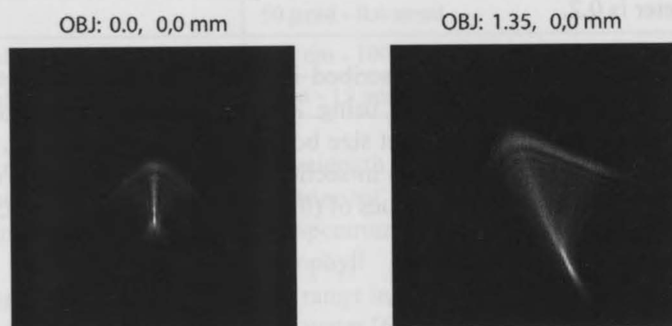

Fig. 6-24. *PSF computed in ZEMAX for two different fields and wavelength of 450 nm.*

Taking into account that the entrance slit is projected over 2.7 mm, the number of resolved spatial pixels is $2700/30 = 90$. The calculated spectral resolution is 7.6 nm FWHM as follows from the computed PSF.

Similar estimates follows from the MTF. In principle, two points can be resolved if the MTF at the corresponding spatial frequency is not zero. This follows from MTF definition via Eq. (2.42) of chapter 2.

The MTF computed in ZEMAX for the fields of (0 mm, 0 mm) and (1.35 mm, 0 mm) and the 450 nm wavelength is shown in Fig. 6-25. The estimated from PSF spot width of 30 μm in saggital direction corresponds to a spatial frequency of 33 cycles per mm. The value of MTF at this frequency for the field of (1.35 mm, 0 mm) is 0.15. The value of MTF for this field varies from 0.15 to 0.27 for different operating wavelengths.

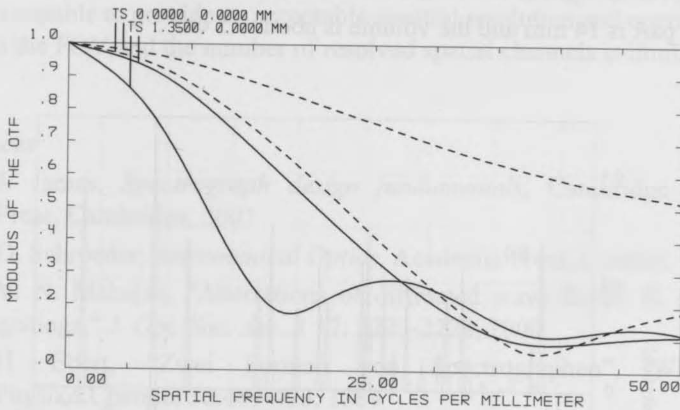

Fig. 6-25. MTF computed in ZEMAX for two different fields and wavelength of 450 nm. "T" denotes tangential (oy) direction and "S" denotes saggital (oz) direction.

The designed spectrometer can be coupled to an objective which projects a line of object pixels on to the entrance slit of the spectrometer. It follows from the Eq. (6.6) that the FOV of such an imaging spectroscopic system would be rather small. For example, for a 10 mm diameter objective the FOV of the system is about 3 degrees.

Although the operating spectral range of 450 nm - 1000 nm and spectral resolution of 7.6 nm are within the range of requirements for the imaging spectrometers stated in Table 7, the capability to resolve not more than 90 spatial pixels is below these requirements. However, for applications where small size and weight of the system are paramount and the requirement to the number of spatial channels is not strict, the spectrometer described in this section could be an appropriate solution.

6.5 Conclusions

This chapter describes a concept of a highly compact spectrometer with all elements (except an external spherical mirror) integrated on a planar MEMS chip.

The device prototype providing a 0.7 nm spectral resolution over 350 nm

range has been designed, fabricated and characterized. The largest dimension of the optical part is 14 mm and the volume is about 0.5 cm^3.

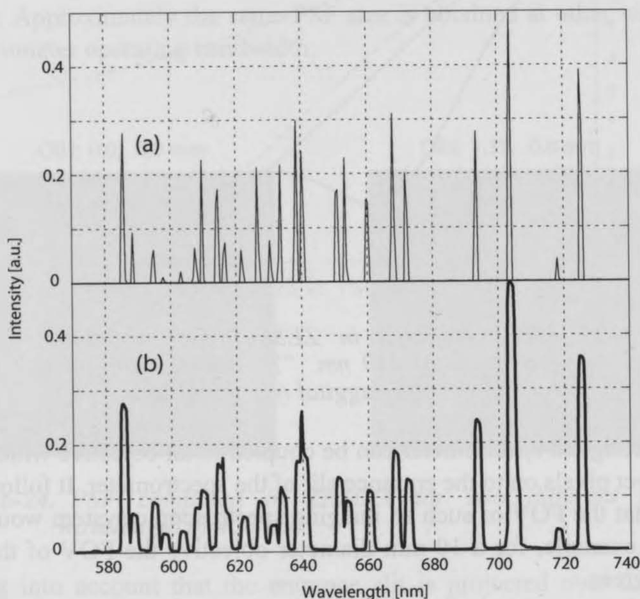

Fig. 6-26. *Ne spectrums measured using fabricated microspectrometer (a) in comparison with the commercial spectrometer (b).*

The comparison of spectrums measured using fabricated microspectrometer and the commercial AvaSpec 2048 spectrometer [6.16] is shown in Fig. 6-26 (in part (a) and part (b) respectively). The performance of the fabricated spectrometer is clearly better both in terms of spectral resolution (the fabricated spectrometer resolves lines which are not resolved by AvaSpec) and stray light (0.2% vs 1% of AvaSpec).

The proposed spectrometer concept can be adopted for various applications. The last section of this chapter presents two designs of a spectrometer optimized for different applications. The first design example is a spectrometer with maximized etendue-resolving power product. Such a device can be applied for measuring spectrum of weak light sources, since its optical system is optimized to collect more light. The second design is an imaging spectrometer which, when

coupled to an objective, forms a pushbroom spectroscopic imaging system. This design is capable to provide an acceptable spectral resolution and operating range, although the FOV and the number of resolved spatial channels is limited.

References

[6.1] J. James. *Spectrograph design fundamentals*, Cambridge University Press, Cambridge, 2007

[6.2] D. Schroeder, *Astronomical Optics*, Academic Press, London, 1987

[6.3] V. N. Mahajan, "Aberrations of diffracted wave fields. II. Diffraction gratings," *J. Opt. Soc. Am. A* 17: 2223-2228, 2000

[6.4] H. Ebert, “Zwei Formen von Spectrographen”, Wied. Ann. Physik&Chemie, 38:489-493, 1889

[6.5] W. G. Fastie, Small plane grating monochromator, *J. Opt. Soc. Am.* 42: 641- 647, 1952

[6.6] Hamamatsu C9409MA spectrometer data sheet

[6.7] Sony ICX278AL sensor data sheet

[6.8] ZEMAX Optical Design Program, User's Guide, Version 9.0 (Focus Software, Inc., Tucson, Ariz., 2000)

[6.9] International Intellectual Group, Inc., *http://www.pcgrate.com*

[6.10] *http://www.videologyinc.com*

[6.11] K. Burns, K. B. Adams, and J. Longwell, "Interference measurements in the spectra of neon and natural mercury," *J. Opt. Soc. Am.* 40: 339-344, 1950

[6.12] R. G. Sellar and G. D. Boreman, “Classification of imaging spectrometers for remote sensing applications”, *Opt. Eng.* 44: 013602, 2005

[6.13] G. A. Shaw and H. K. Burke, "Spectral imaging for remote sensing," *Lincoln Laboratory Journal*, 14: 3-28, 2003

[6.14] F. Blechinger, B. Harnisch, and B. P. Kunkel, “Optical concepts for high-resolution imaging spectrometers“, *Proc. SPIE* 2480: 165, 1995

[6.15] K. Kallio, S. Koponen and J. Pulliainen, “Feasibility of airborne imaging spectrometry for lake monitoring—a case study of spatial chlorophyll a distribution in two meso-eutrophic lakes.” *International Journal of Remote Sensing.* 24(19): 3771-3790, 2003

[6.16] AvaSpec 2048 spectrometer datasheet, *http://www.avantes.com*

coupled to an objective, forms a push-broom spectroscopic imaging system. This design is capable to provide an acceptable spectral resolution and operating range, although the FOV and the number of resolved spatial channels is limited.

References

[6.1] J. James, *Spectrograph design fundamentals*, Cambridge University Press, Cambridge, 2007

[6.2] D. Schroeder, *Astronomical Optics*, Academic Press, London, 1987

[6.3] V. N. Mahajan, "Aberrations of diffracted wave fields. II. Diffraction gratings", *J. Opt. Soc. Am. A* 17: 2223-2228, 2000

[6.4] H. Ebert, "Zwei Formen von Spectrographen", *Wied. Ann. Physik&Chemie*, 38:489-493, 1889

[6.5] W. G. Fastie, Small plane grating monochromator, *J. Opt. Soc. Am.* 42: 641-647, 1952

[6.6] Hamamatsu C9409MA spectrometer data sheet

[6.7] Sony ICX275AL sensor data sheet

[6.8] ZEMAX Optical Design Program, User's Guide, Version 9.0 (Focus Software, Inc, Tucson, Ariz. 2000)

[6.9] International Intellectual Group, Inc., *http://www.pegrand.com*

[6.10] *http://www.videologyinc.com*

[6.11] K. Burns, K. B. Adams, and J. Longwell, "Interference measurements in the spectra of neon and natural mercury," *J. Opt. Soc. Am.* 40: 339-344, 1950

[6.12] R. G. Sellar and G. D. Boreman, "Classification of imaging spectrometers for remote sensing applications", *Opt. Eng.* 44: 013602, 2005

[6.13] G. A. Shaw and H. K. Burke, "Spectral imaging for remote sensing", *Lincoln Laboratory Journal*, 14: 3-28, 2003

[6.14] F. Blechinger, B. Harnisch, and B. P. Kunkel, "Optical concepts for high-resolution imaging spectrometers", *Proc. SPIE* 2480: 165, 1995

[6.15] K. Kallio, S. Koponen and J. Pulliainen, "Feasibility of airborne imaging spectrometry for lake monitoring—a case study of spatial chlorophyll a distribution in two meso-eutrophic lakes," *International Journal of Remote Sensing*, 24(19): 3771-3790, 2003

[6.16] AvaSpec 2048 spectrometer datasheet, *www.avantes.com*

7. Conclusions

This final chapter combines the results presented in the thesis, which are the framework for drawing conclusions making suggestions for future work.

7.1 Three approaches to make a microspectrometer

In Chapter 3 it was shown that the optimal way to build a microspectrometer is to use a diffraction grating as a dispersive element. Indeed, the dispersion of a grating is higher than that of a prism, it is more suitable for use in a wide wavelength operating range than Fabry-Perot etalons and, finally, diffraction gratings can be fabricated in a MEMS-compatible process.

Three approaches to make a grating-based microspectrometer are described in this thesis:

- Planar microspectrometer.
- Spectrometer based on a concave grating which is fabricated in a MEMS-compatible process.
- Spectrometer with an external spherical mirror.

The first approach includes single- and double-grating planar designs. Double-grating spectrometer is superior than the single-grating one in terms of spectral resolution and operating bandwidth, although at a price of higher light losses due to the limited diffraction efficiency of the gratings.

The use of concave gratings (the second approach) allows to improve spectral resolution and to increase etendue since aberrations can be compensated more efficiently with a non-planar grating surface. A spectrometer based on a concave grating consists of only three elements (slit, grating and photosensor) and can be made quite small in size, although larger than planar spectrometers. In principle, entrance slit and photodetectors can be integrated on a single MEMS chip resulting in a two-component spectrometer consisting of chip and concave grating.

Finally, the third approach combines a single spherical mirror and a planar chip integrating slit, photodetectors and aberration-correcting planar grating. The performance of the imaging system of this spectrometer is almost diffraction-limited. This implies that the design of this device has almost reached the physical limits in terms of maximum spectral resolution at dimensional constraints.

TABLE 1. ***Qualitative comparison of the developed microspectrometers.***

Spectrometer	Resolution	Operating range	Optical throughput	Fabrication cost
Single-grating planar	bad	small	small	low
Double-grating planar	medium	large	small	low
Concave grating	medium	medium	large	medium
Planar grating combined with an external mirror	high	large	large	medium

Table 1 presents a qualitative comparison of the developed spectrometers in terms of spectral resolution, size of the spectral operating range, optical throughput and potential fabrication cost (in mass production).

The highest level of integration (complete MEMS-compatible fabrication) is possible with planar spectrometers. That is why the potential fabrication cost of a single planar spectrometer can be very low. At the same time, the resolution (3 nm) and operating range (300 nm) of the double grating spectrometer can be sufficient for many applications. The only significant drawback of planar spectrometers is a relatively small optical throughput. Thus, these devices are most suitable for the applications where light sources to be measured are sufficiently bright and extremely small size and weight of an instrument as well as low cost are important.

The problem of low throughput can be solved to some degree with a concave grating. The main disadvantages in using a concave grating are field curvature and aberrations which, although smaller than in case of a single planar grating, still can not be eliminated completely to make imaging system diffraction-limited. That is why Table 1 indicates that a spectrometer based on a concave grating can have a large optical throughput, but medium spectral resolution and operating bandwidth. The technology for the fabrication of concave gratings described in this thesis allows the realisation of gratings in a MEMS-compatible process. Nevertheless, the fabrication of a concave grating based spectrometer is a bit more complicated (requires a postprocessing step) than that of a planar one, so the potential cost is higher.

The best performance has been achieved in a system using a concave mirror combined with an aberration-correcting planar grating. Such a spectrometer consists of only two components (MEMS chip and a low cost spherical mirror) and the potential cost of the device is low, although higher than that of a planar spectrometer. The characteristics of the spectrometer allows to use it for many applications including high resolution measurements and spatial multichannel measurements (imaging spectrometer). At the same time, the device has extremely small dimensions as compared to available commercial spectrometers. The presence of a single non-MEMS component makes the fabrication process of this microspectrometer the least IC-compatible as compared to the above mentioned concepts.

Finally, Fig. 7-1 compares Ne spectrums measured using microspctrometers described in this thesis (single-grating and double-grating spectrometers, concave grating spectrometer and spectrometer with the external spherical mirror) in comparison with the spectrum measured using the commercially available AvaSpec 2048 spectrometer [7.7].

The improvement in spectral resolution and stray light is clearly visible from Fig. 7-1(a) to Fig. 7-1(d).

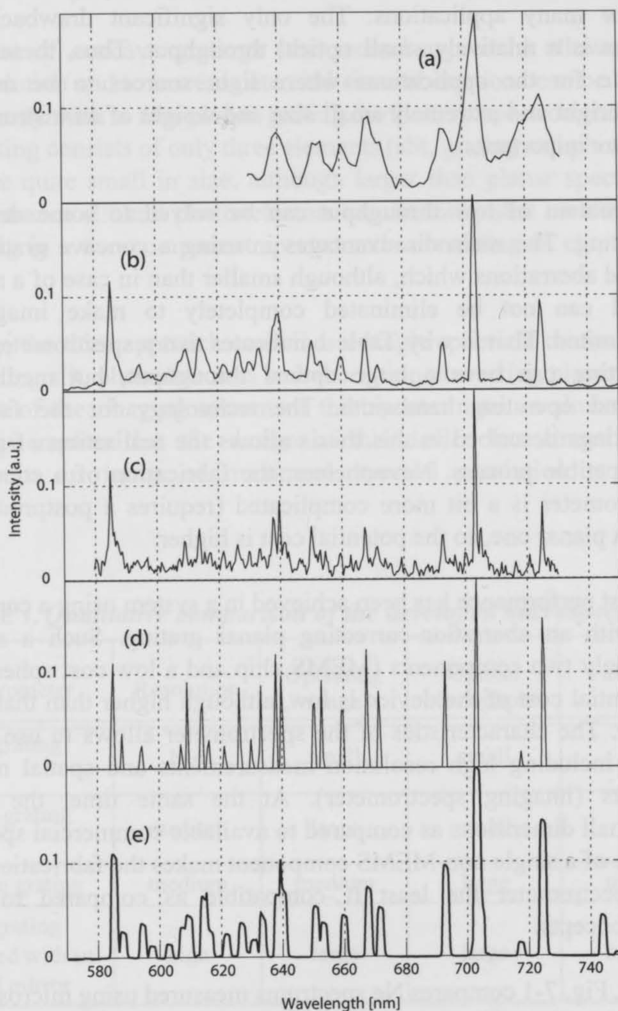

Fig. 7-1. *Ne spectrums measured using single-grating microspectrometer (a), double-grating microspectrometer (b), fabricated concave grating (c), spectrometer with a concave mirror and planar grating (d) and a commercial spectrometer (e).*

7.2 Performance of the developed microspectrometers in comparison with the commercial devices

The main characteristics of some of the compact spectrometers described in this thesis are given in Table 2 in comparison with the same characteristics of commercially available spectrometers according to manufacturers datasheets [7.1] - [7.6].

TABLE 2. ***Comparison of main parameters of the spectrometers described in this thesis and commercially available devices ([7.1]-[7.6]).***

	Slit, μm x μm	NA, rad	Δλ, nm	λ/Δλ (at 600 nm)	Volume, cm^3	GR, $\mu m^2 rad^2$
Spectrometers described in this thesis						
Planar double-grating spectrometer	25x100	0.05	3	200	0.1	$4x10^3$
Concave grating spectrometer	5x5	0.11	1	600	0.8	570
Spectrometer with an external mirror	6x200	0.14	0.7	857	0.5	$6.3x10^4$
Spectrometer with an external mirror (max. GR)	25x600	0.22	1.7	352	1	$8x10^5$
Hamamatsu spectrometers						
C9409MA	70x550	0.22	9	67	22	$3.9x10^5$
C10988MA	75x750	0.22	12	50	6	$4.3x10^5$
C10083CAH	10x1000	0.11	1	600	664	$2.3x10^5$
Ocean Optics spectrometers						
USB2000	5x1000	0.22	0.95	631	205	$4.8x10^5$
	25x1000	0.22	1.3	461	205	$1.75x10^6$
	25x1000	0.22	0.6	1000	205	$3.8x10^6$
JobinYvon spectrometers						
cp20	50x500	0.185	5	120	10	$3.2x10^5$
VS70	25x500	0.25	1	600	432	$8x10^5$

It follows from Table 2 that spectral resolution of the developed microspectrometers is comparable or even better that the resolution of commercial spectrometers, while the reduction of volume is 2 - 3 orders of magnitude. It should be mentioned, that the volume of commercial devices given in Table 2 also includes spectrometer housing (the size of optical part is not available in manufacturers datasheets), while volume of the developed spectrometers includes only optical part. However, the numbers in Table 2 still give an adequate impression since for a large spectrometer the increase in volume due to the housing is small as compared to the total volume.

The etendue-resolving power product of the microspectrometers described in this thesis is comparable or smaller than the same characteristic of commercial spectrometers. This is natural, since the entrance slit of a small system designed to provide as high spectral resolution as possible is also small. Concave grating based spectrometer described in Chapter 5 has the smallest etendue-resolving power product. This is due to the use of an optical fiber tip as an entrance slit. In spite of spectral resolution of 1 nm and NA of 0.11 (better parameters that those of the double-grating planar microspectrometer), the small area of the entrance slit finally degrades the etendue-resolving power product.

The conclusion that can be drawn from the comparison of spectrometers in Table 2, is that the developed microspectrometers can be used for the same applications that are currently served by available commercial spectrometers. At the same time the extremely compact microspectrometers described in this thesis can offer the advantage of low size, low weight and low cost, which can expand the range of applications.

7.3 Suggestions for future work

The final goal of the development of any device is to make it useful for people and to deliver the device to the market. The work described in this thesis should be continued to reach this goal.

The planar devices described in this thesis have demonstrated a relatively high level of stray light due to Fresnel reflections from the glass plates. This problem can be solved applying an appropriate antireflection coating, which can be the scope of future work.

Technology for the fabrication of concave gratings in a MEMS-compatible process has so far not resulted in grating surface of a high optical quality, which was due to the rough surface of the dry film resist used in the fabrication process. Such a surface roughness results in stray light when gratings are used for spectral measurements. Possible solution could be to use a resist of better quality if it is available on the market, or to modify the process used for the polymer membrane fabrication.

Spectrometers with an external mirror are actually free from serious problems. The device sensitivity can be improved by increasing the diffraction efficiency of the grating. To achieve this, a gray-scale lithography, for example, can be considered to fabricate triangular profile (blazed) gratings. However, it should be noted that the external mirror is fundamentally non-IC compatible.

Finally, future work can be directed to the integration of the devices - the design of a custom CMOS array of potodetectors and the development of the fabrication process to allow integration of the photodetectors, entrance slit and diffraction grating on a single silicone chip. Such a process will consist of the fabrication of photodetectors on a silicone wafer in a standard CMOS process and subsequent postprocessing including lithographic fabrication of the grating and silicone etching to open the entrance slit.

References

[7.1] Hamamatsu minispectrometer C9409MA datasheet

[7.2] Hamamatsu spectrometer C10083CAH datasheet

[7.3] Hamamatsu spectrometer C10988MA datasheet

[7.4] Ocean Optics USB2000 spectrometer datasheet

[7.5] JobinYvon minispectrometer cp20 datasheet

[7.6] JobinYvon spectrometer vs70 datasheet

[7.7] AvaSpec 2048 spectrometer datasheet

Summary

Optical spectrometers - devices that measure the spectrum of light - have found widespread application in industry, medicine and science. Examples of applications range from the investigation of the chemical composition of stars and planets to the in vivo analysis of cells and organisms. Compact (with dimensions comparable to those of an integrated electronic component-IC's) and inexpensive spectrometers could bring new applications, which would not be feasible (economically or technically) with the large conventional spectrometers.

This thesis discusses the development of such a microspectrometer. The goal of this development was to maximize spectrometer performance at dimensional constraints. Moreover, the design should be suitable for fabrication in a batch-like process intended for the mass production at low cost per single device. These characteristics make an IC-compatible MEMS-like fabrication process an obvious choice, since it also allows the integration of optical components with electronic circuits.

The contribution of the work described in this thesis is the development and experimental validation of three microspectrometer concepts. For each of these concepts a prototypes device was designed, fabricated and characterized.

The first concept is a spectrometer that includes only planar components - a 'flat' spectrometer. The device consists of two parallel MEMS-processed plates with mirrors and imaging diffraction grating, which are used to provide the imaging functionality in the absence of collimating and focusing non-planar optics. The important advantage of this concept is that the fabrication of the device is fully IC-compatible. Two designs had been fabricated - a

microspectrometer with a single grating and another with a double grating.

The second concept is a spectrometer composed of three-elements (entrance slit, concave grating and image sensor). The concave imaging grating was fabricated in an IC-compatible process with an additional post-processing step. The concept of a concave grating based spectrometer has been well known for already a long time. However, the importance of this work is the adaptation of a standard MEMS processing for the fabrication of miniature concave imaging gratings in a batch process, which is based on the applying photolithography on planar surfaces.

Finally, the third concept is a microspectrometer composed of MEMS components with one single external non-MEMS element, a concave mirror. This concept combines the advantages provided by MEMS technologies for integration of as many of the components as possible on a single chip, including entrance slit, image sensor and diffraction grating, with one single component pf superior optical performance. This grating is specially designed to compensate for the aberrations of the spherical mirror, which results in an almost diffraction-limited performance of the optical micro-system.

These three concepts in a row demonstrate how the performance in terms of spectral resolution and signal-to-noise ratio improves from the first one to the last one at the expense of a reduced IC compatibility of the fabrication. Nevertheless, each of the microspectrometers developed is in principle suitable for practical application after an industrial product development effort, since the performance of these small and potentially cheap devices is comparable with the characteristics of conventional large spectrometers.

Samenvatting

Optische spectrometers - apparaten voor de meting van het spectrum van het licht - hebben op grote schaal toepassing gevonden in de industrie, de geneeskunde en de wetenschap. Voorbeelden van toepassingen variëren van onderzoek naar de chemische samenstelling van sterren en planeten tot de in vivo analyse van cellen en organismen. Compacte (met afmetingen vergelijkbaar met die van een geïntegreerde elektronische componenten-IC's) en goedkope spectrometers kunnen nieuwe toepassingen mogelijk maken, welke niet haalbaar zouden zijn (economisch of technisch) met grote conventionele spectrometers.

Dit proefschrift bespreekt de ontwikkeling van een dergelijke microspectrometer. Het doel van deze ontwikkeling was de spectrometerprestaties te maximaliseren bij dimensionale beperkingen waarbij het ontwerp geschikt moet zijn voor fabricage in een 'batch-proces', welke is bedoeld voor massaproductie tegen lage stukskosten. Bij deze randvoorwaarden is fabricage in een IC-compatibel MEMS-achtig fabricageproces een de hand liggende keuze, aangezien het ook de integratie van optische componenten met elektronische schakelingen mogelijk maakt.

De bijdrage van het werk beschreven in dit proefschrift is de ontwikkeling en experimentele validatie van drie microspectrometerconcepten. Voor elk van deze concepten is een prototypes van een apparaat ontworpen, gefabriceerd en gekarakteriseerd.

Het eerste concept is een spectrometer welke uitsluitend planaire componenten bevat - een 'platte' spectrometer. Het apparaat bestaat uit twee parallelle platen, waarbij via MEMS-technologieën spiegels en een

beeldvormende diffractietralie zijn gerealiseerd, om beeldvorming mogelijk te maken bij afwezigheid van collimerende of focusserende niet-planaire optica. Het belangrijkste voordeel van dit concept is de volledig IC-compatibele fabricage van het apparaat. Twee ontwerpen zijn gerealiseerd - een microspectrometer met een enkele tralie en een met een dubbele tralie.

Het tweede concept is een spectrometer welke is samengesteld uit drie elementen (ingangsgleuf, concaaf tralie en beeldvormende sensor). De beeldvormende tralie in een spiegel met concaaf oppervlak en gefabriceerd in een IC-compatibel proces met een extra nabewerking. Het concept van een spectrometer met een tralie in een spiegel met concaaf oppervlak al geruime tijd bekend. De belangrijke bijdrage van dit werk is de aanpassing van een standaard MEMS proces, zodat het geschikt wordt voor de fabricage van kleine beeldvormende tralies in een niet-planair oppervlak bij gebruik van een batch proces welke is ingericht op toepassing van fotolithografie op planaire oppervlakten.

Het derde concept, tenslotte, is een microspectrometer welke is samengesteld uit MEMS componenten met een enkel externe, niet-MEMS element, een concaaf sferische spiegel. Dit concept combineert de voordelen die de MEMS-technologie biedt, om zoveel mogelijk componenten op een enkele chip te integreren, inclusief de ingangsspleet, de beeldsensor en de diffractietralie, met de superieure optisch kwaliteit van een enkele externe component. De speciaal ontworpen tralie compenseert voor de aberraties van de externe sferische spiegel, waardoor de prestaties van de optische micro-systeem bijna diffractiegelimiteerd zijn.

Deze drie concepten op een rij tonen aan hoe de prestaties van de eerste tot de laatste verbeteren in termen van spectrale resolutie en signaal-ruis-verhouding, ten koste van een verminderde compatibiliteit met IC fabricage. Desondanks is elk van de ontwikkelde microspectrometers in principe geschikt voor praktische toepassing na een industriële productontwikkeling, aangezien de prestaties van deze kleine en potentieel goedkope apparaten vergelijkbaar zijn met de eigenschappen van conventionele grote spectrometers.

Acknowledgements

This work could not have been completed without the help and support of many people. It is a pleasure to thank all those who made this thesis possible and to them I would like to express my deeply felt gratitude. In particular, I would like to thank:

Dr. Reinoud F. Wolffenbuttel, my supervisor, for his continuous support and guidance throughout all the period of this project, for his encouragement and inspiration. His ideas, his experience, practical help and enthusiasm were essential for the results achieved in this project. I owe my deepest gratitude to him for all the skills and knowledge I acquired from him.

Dr. Gleb Vdovin whose support and expertise in optics were crucial in the early phase of the project. I'm also indebted to him for his help in various practical issues during my adaptation period after coming to The Netherlands.

Prof. Gerard C. M. Meijer, my promotor, to whom I'm very grateful for his valuable advices on my work.

Arvin Emadi, Huaiwen Wu and Ger de Graaf, my closest colleagues. It was a great pleasure to work with them in the same research group. I'm thankful to them for being so very cooperative and for helping me to enjoy the days at the TU Delft.

All my colleagues at the Electronic Instrumentation Laboratory and the head of the Laboratory Prof. Paddy French, for creating a warm and creative research environment. I'm thankful to Willem van der Sluys for his valuable help

with financial and administration issues. To Joyce Siemers, Ilse van der Kraaij, Trudie Houweling and Inge Egmond for practical and administrative support. To Jeroen Bastemeijer, Maureen Meekel, Jeff Mollinger and Piet Trimp for their help with technical and IT problems. I would like to thank my fellow PhD students, especially Vijay Rajaraman, Eduardo Margallo, Lujun Zhang and Chung-Kai Yang, for their cooperation and friendliness.

The members of Delft Institute of Microsystems and Nanoelectronics (DIMES) Prof. Lina Sarro, Charles de Boer, Cassan Visser, Jan Groeneweg, Wim van der Vlist, Jan Cornelis Wolff and Tom Scholtes for their considerable help with the microfabrication and for teaching me to work in a cleanroom.

Rob Vink (TNO Delft) and Elena Sokolova (River Diagnostics BV) for their important advices and help on different technical issues.

Oleg Soloviev, Mikhail Loktev, Dorota and Alain Grandcoing, Yadira and Frans Lambregts, are very nice and friendly people. I feel fortunate to have met them during my living in Delft.

All my teachers from the Moscow Institute of Physics and Technology, especially Oleg A. Ryabushkin, Mikhail Vyatkin, Alexander D. Romanov, Sergey M. Korshunov and Vladimir A. Rastrenin for giving me knowledge, inspiration for science and for helping me to grow up as a researcher.

The teachers from the Gymnasium N1 in Penza: Nadezhda N. Pushkareva, Lyudmila I. Lazarevskaya, Olga A. Baryshnikova and Anatoly V. Uchevadov for their encouragement in studying physics.

My parents and my grandmothers for bringing me up, for their love and care, their support and for everything they gave to me. I'm deeply grateful to them.

Finally, I would like to thank my beloved wife Irina for her love and for making my life full of joy and happiness.

List of publications

In scientific journals

H. Wu, S. Grabarnik, A. Emadi, G. de Graaf and R. F. Wolffenbuttel, “Characterization of thermal cross-talk in a MEMS-based thermopile detector array“, *J. Micromech. Microeng.* 19: 074022, 2009

A. Emadi, H. Wu, S. Grabarnik, G. de Graaf and R. F. Wolffenbuttel, “Vertically tapered layers for optical applications fabricated using resist reflow“, *J. Micromech. Microeng.* 19: 074014, 2009

S. Grabarnik, A. Emadi, H. Wu, G. de Graaf, and R. F. Wolffenbuttel, "High-resolution microspectrometer with an aberration-correcting planar grating," *Appl. Opt.* 47: 6442-6447, 2008

S. Grabarnik, A. Emadi, H. Wu, G. de Graaf, G. Vdovin and R. F. Wolffenbuttel, "Fabrication of an imaging diffraction grating for use in a MEMS-based optical microspectrograph", *J. Micromech. Microeng.* 18: 064006, 2008

H. Wu, S. Grabarnik, A. Emadi, G. de Graaf and R. F. Wolffenbuttel, “A thermopile detector array with scaled TE elements for use in an integrated IR microspectrometer“, *J. Micromech. Microeng.* 18: 064017, 2008

S. Grabarnik, A. Emadi, E. Sokolova, G. Vdovin, and R. F. Wolffenbuttel, "Optimal implementation of a microspectrometer based on a single flat diffraction grating," *Appl. Opt.* 47: 2082-2090, 2008

S. Grabarnik, R. Wolffenbuttel, A. Emadi, M. Loktev, E. Sokolova, and G. Vdovin, " Planar double-grating microspectrometer," *Opt. Express* 15: 3581-3588, 2007

A. N. Simonov, S. Grabarnik, and G. Vdovin, "Stretchable diffraction gratings for spectrometry," *Opt. Express* 15: 9784-9792, 2007

M. Yu. Vyatkin, S. P. Grabarnik, O. A. Ryabushkin, "Temperature dependence of the radiation wavelength of a fibre laser", *QUANTUM ELECTRON.*, 35(4): 323-327, 2005

In conference proceedings

S. Grabarnik, A. Emadi, H. Wu, G. de Graaf, R. F. Wolffenbuttel, "Microspectrometer with a concave grating fabricated in a MEMS technology", Proceedings of the Eurosensors XXIII, September 6 - 9, 2009, Lausanne, Switzerland, pp. 401-404

H. Wu, A. Emadi, S. Grabarnik, G. de Graaf, R. F. Wolffenbuttel, "Static and Dynamic Analysis of Thermal Cross-Talk in an Thermopile Detector Array for use in a Microspectrometer", Proceedings of the Eurosensors XXIII, September 6 - 9, 2009, Lausanne, Switzerland, pp. 1139-1142

A. Emadi, H. Wu, S. Grabarnik, G. De Graaf and R. F. Wolffenbuttel, "IC-Compatible Fabrication of Linear Variable Optical Filters for Micro-Spectrometer", Proceedings of the Eurosensors XXIII, September 6 - 9, 2009, Lausanne, Switzerland, pp. 1143-1146

A. Emadi, H. Wu, S. Grabarnik, G de Graaf and R. F. Wolffenbuttel, "Interference filter based IR absorber for MEMS thermopile array", Proceedings of MME, September 20-22, 2009, Toulouse, France, paper 217

H. Wu, S. Grabarnik, G. de Graaf, A. Emadi and R. F. Wolffenbuttel, "Thermal Cross-Talk in IC-Compatible Micromachined Infrared Thermopile Detector Arrays", IRS 2009 Proceedings , SENSOR+TEST Conference 2009, May 26 - 28, 2009, Nurnberg, Germany, pp. 319 - 323

H. Wu, S.Grabarnik, A. Emadi, G. de Graaf and R. F. Wolffenbuttel, "Study

of Thermal Cross-Talk in Micromachined Thermopile based Infrared Detector Arrays", Proceedings of Sense of Contact, April 8, 2009, Zeist, The Netherlands, pp. 1 - 5

A. Emadi, S.Grabarnik, H. Wu, G. de Graaf and R F Wolffenbuttel, "IC-Compatible Fabrication of Linear Variable Optical Filter for Micro-spectrometer",Proceedings of Sense of Contact, April 8, 2009, Zeist, The Netherlands, pp. 1 - 5

H. Wu, S. Grabarnik, G. de Graaf, A. Emadi and R. F. Wolffenbuttel, "Characterization of thermal cross-talk in a thermopile detector", Proceedings of MME, September 28 - 30 , 2008, Aachen, Germany, pp. 415-418.

A. Emadi, H. Wu, S. Grabarnik, G. de Graaf and R. F. Wolffenbuttel, "Fabrication of tapered optical structures using resist reflow", Proceedings of MME, September 28 - 30 , 2008, Aachen, Germany, pp. 113-116.

A. Emadi, H. Wu, S. Grabarnik, G. de Graaf and R. F. Wolffenbuttel, "Simulation and analytical calculation of reflowed resist structures", Proceedings of MME, September 28 - 30 , 2008, Aachen, Germany, pp. 347-350.

H. Wu, S. Grabarnik, A. Emadi, G. de Graaf and R. F. Wolffenbuttel, "Cross-talk characterization of thermal detector array", Proceedings of the Eurosensors XXII, September 7 - 10, 2008, Dresden, Germany, pp. 366-369.

S. Grabarnik, A. Emadi, H. Wu, G. de Graaf and R. F. Wolffenbuttel, "Optical microspectrometer with planar grating and external spherical mirror". Proceedings of the Eurosensors XXII, September 7 - 10, 2008, Dresden, Germany, pp. 350-353.

H. Wu, A. Emadi, W. van der Vlist, S.Grabarnik, G. de Graaf and R. F. Wolffenbuttel, "Design and fabrication of a thermopile detector array with scaled elements for an integrated IR microspectrometer", Proceedings of APCOT, June 22 - 25, 2008, Tainan, Taiwan, pp. 213-216.

S. Grabarnik, A. Emadi, H. Wu, G. de Graaf, G. Vdovin and R. F. Wolffenbuttel, "Planar MEMS-compatible microspectrograph", Proceedings of APCOT, June 22 - 25, 2008, Tainan, Taiwan, pp. 53-56.

S. Grabarnik, A. Emadi, H. Wu, G. De Graaf, and R. F. Wolffenbuttel, "Concave diffraction gratings fabricated with planar lithography", Proc. SPIE, Vol. 6992: 699214, 2008

S. Grabarnik, A. Emadi, H. Wu, G. De Graaf, G. Vdovin, and R. F. Wolffenbuttel, "IC-compatible microspectrometer using a planar imaging diffraction grating", Proc. SPIE Vol. 6992: 699215, 2008

S. Grabarnik, A. Emadi, H.Wu, G de. Graaf, G. Vdovin, R.F. Wolffenbuttel, "Spectral sensor based on an imaging diffraction grating and fabricated with MEMS technologies", Proceedings of MME, September 16 - 18, 2007, Guimaraes, Portugal. pp 175-178.

S. Grabarnik, A. Simonov, G. Vdovin, "Aberrations of a stretchable diffraction grating", in Proc. of the EOS Topical Meeting on Micro-Optics, Diffractive Optics and Optical MEMS, October 17-19, 2006, Paris, France, pp. 144-145.

M. Vyatkin, S. Grabarnik, and O. Ryabushkin, " Temperature Dependent Behaviour of Emission Wavelength of the Rare Earths Doped Fiber Lasers," in Advanced Solid-State Photonics (TOPS), Vol. 98 of OSA Trends in Optics and Photonics (Optical Society of America, 2005), February 6, 2005, Vienna, Austria, p. 536.

M. Vyatkin, R. Yagodkin, S. Grabarnik, A. Avdokhin, S.Popov, V.P. Gapontsev and J. R. Taylor, "A practical realization of the compact, multi-watt 775 nm source by frequency doubling of linearly polarized Yb-Er fiber pump in PPKTP", Paper 2.6, 2nd International Symposium on High Power Fiber Lasers and Their Applications, St. Petersburg, Russia, 2003

M. Vyatkin, S. Grabarnik. A. Rulkov, V. Gapontsev, "1W, 980nm single mode Yb fiber laser", 2nd International Symposium on High Power Fiber Lasers and Their Applications, St. Petersburg, Russia, 2003

About the author

Semen Grabarnik was born in Penza, Russia, on September 9th, 1980. After graduating from Penza Gymnasium N1 in 1997, he entered the Moscow Institute of Physics and Technology, where he received his M.Sc. degree cum laude in applied physics and mathematics in 2003. His specialization was in fiber optics and lasers and his graduation project was dedicated to the research of the temperature effects in high-power fiber lasers. From 2003 till 2005 he was working on the simulation of the pipelines and integration of the numerical models with the pipeline control systems. However, his passion for physics resulted in his joining Electronic Instrumentation Laboratory of TU Delft as a PhD student and a member of the microspectrograph project in 2005. His research was focused on the development of highly miniaturized spectrometer systems suitable for the fabrication using microtechnologies. Since July 2009 he is employed by AOES Group BV, The Netherlands, where he works on the analysis of optical instruments for the projects of the European Space Agency.

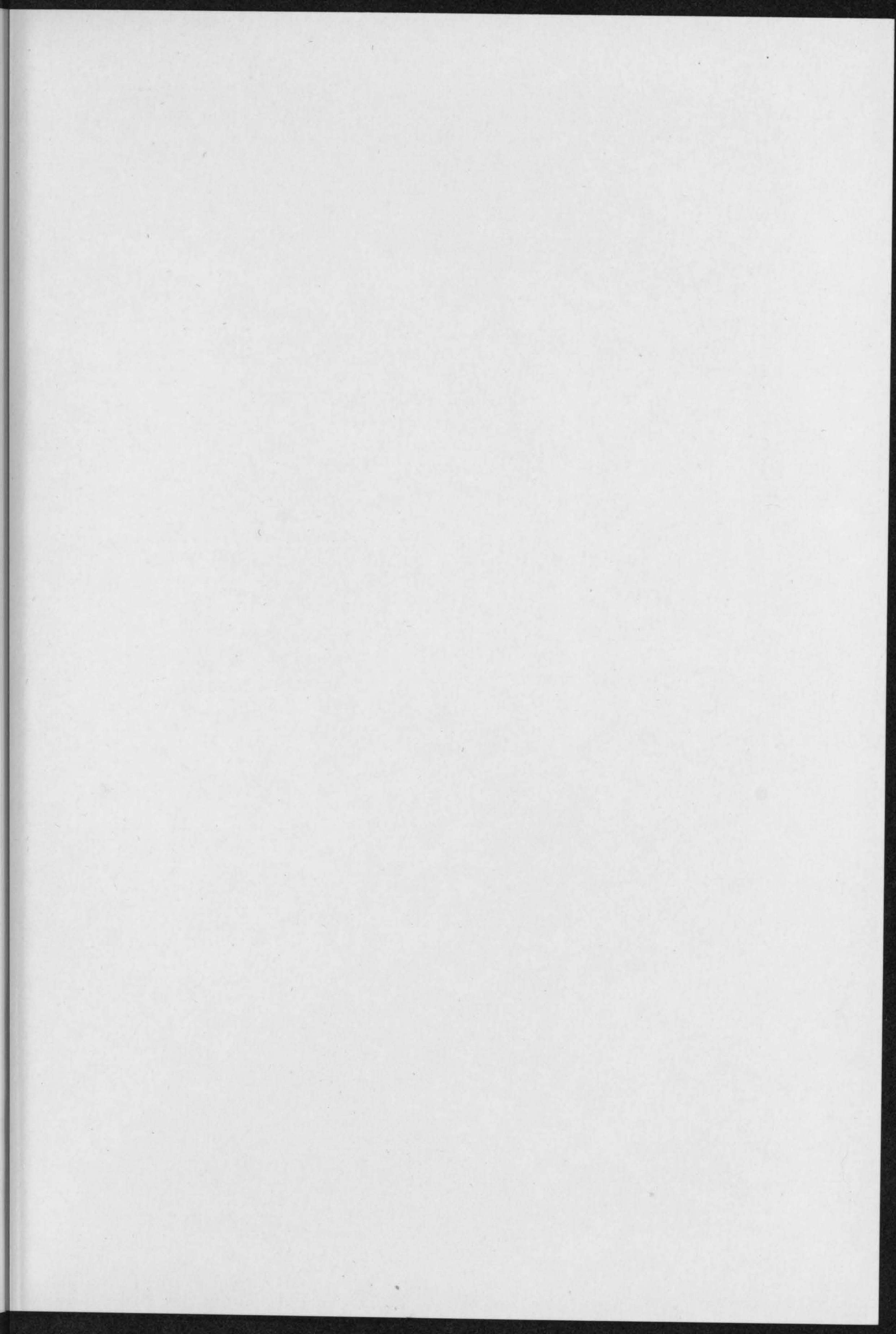

Delft University of Technology

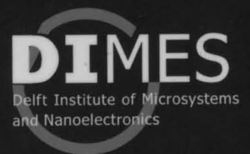

ISBN: 978 - 90 - 9025048 - 9